NASA/TP—2020-220185

Stochastic Simulation of Mudcrack Damage Formation in an Environmental Barrier Coating

Noel N. Nemeth
Glenn Research Center, Cleveland, Ohio

Subodh K. Mital
University of Toledo, Toledo, Ohio

Evan J. Pineda, Brett A. Bednarcyk, Pappu L.N. Murthy, and Dongming Zhu
Glenn Research Center, Cleveland, Ohio

Haydn N.G. Wadley
University of Virginia, Charlottesville, Virginia

Steven M. Arnold
Glenn Research Center, Cleveland, Ohio

February 2020

NASA STI Program . . . in Profile

Since its founding, NASA has been dedicated to the advancement of aeronautics and space science. The NASA Scientific and Technical Information (STI) Program plays a key part in helping NASA maintain this important role.

The NASA STI Program operates under the auspices of the Agency Chief Information Officer. It collects, organizes, provides for archiving, and disseminates NASA's STI. The NASA STI Program provides access to the NASA Technical Report Server—Registered (NTRS Reg) and NASA Technical Report Server—Public (NTRS) thus providing one of the largest collections of aeronautical and space science STI in the world. Results are published in both non-NASA channels and by NASA in the NASA STI Report Series, which includes the following report types:

- TECHNICAL PUBLICATION. Reports of completed research or a major significant phase of research that present the results of NASA programs and include extensive data or theoretical analysis. Includes compilations of significant scientific and technical data and information deemed to be of continuing reference value. NASA counter-part of peer-reviewed formal professional papers, but has less stringent limitations on manuscript length and extent of graphic presentations.

- TECHNICAL MEMORANDUM. Scientific and technical findings that are preliminary or of specialized interest, e.g., "quick-release" reports, working papers, and bibliographies that contain minimal annotation. Does not contain extensive analysis.

- CONTRACTOR REPORT. Scientific and technical findings by NASA-sponsored contractors and grantees.

- CONFERENCE PUBLICATION. Collected papers from scientific and technical conferences, symposia, seminars, or other meetings sponsored or co-sponsored by NASA.

- SPECIAL PUBLICATION. Scientific, technical, or historical information from NASA programs, projects, and missions, often concerned with subjects having substantial public interest.

- TECHNICAL TRANSLATION. English-language translations of foreign scientific and technical material pertinent to NASA's mission.

For more information about the NASA STI program, see the following:

- Access the NASA STI program home page at http://www.sti.nasa.gov

- E-mail your question to help@sti.nasa.gov

- Fax your question to the NASA STI Information Desk at 757-864-6500

- Telephone the NASA STI Information Desk at 757-864-9658

- Write to:
  NASA STI Program
  Mail Stop 148
  NASA Langley Research Center
  Hampton, VA 23681-2199

NASA/TP—2020-220185

Stochastic Simulation of Mudcrack Damage Formation in an Environmental Barrier Coating

Noel N. Nemeth
Glenn Research Center, Cleveland, Ohio

Subodh K. Mital
University of Toledo, Toledo, Ohio

Evan J. Pineda, Brett A. Bednarcyk, Pappu L.N. Murthy, and Dongming Zhu
Glenn Research Center, Cleveland, Ohio

Haydn N.G. Wadley
University of Virginia, Charlottesville, Virginia

Steven M. Arnold
Glenn Research Center, Cleveland, Ohio

National Aeronautics and
Space Administration

Glenn Research Center
Cleveland, Ohio 44135

February 2020

Acknowledgments

We would like to gratefully acknowledge the inspiration, guidance, and collaboration of our colleague and friend, Dr. Dongming Zhu, who regretfully passed away before this report could be completed. He will be greatly missed.
This work was funded by the NASA Transformative Tools and Technologies Program.

This work was sponsored by the
Transformative Aeronautics Concepts Program.

Level of Review: This material has been technically reviewed by expert reviewer(s).

Available from

NASA STI Program
Mail Stop 148
NASA Langley Research Center
Hampton, VA 23681-2199

National Technical Information Service
5285 Port Royal Road
Springfield, VA 22161
703-605-6000

This report is available in electronic form at http://www.sti.nasa.gov/ and http://ntrs.nasa.gov/

Contents

Stochastic Simulation of Mudcrack Damage Formation in an Environmental Barrier Coating

Noel N. Nemeth
National Aeronautics and Space Administration
Glenn Research Center
Cleveland, Ohio 44135

Subodh K. Mital
University of Toledo
Toledo, Ohio 43606

Evan J. Pineda, Brett A. Bednarcyk, Pappu L.N. Murthy, and Dongming Zhu
National Aeronautics and Space Administration
Glenn Research Center
Cleveland, Ohio 44135

Haydn N.G. Wadley
University of Virginia
Charlottesville, Virginia 22904

Steven M. Arnold
National Aeronautics and Space Administration
Glenn Research Center
Cleveland, Ohio 44135

Summary

The FEAMAC/CARES program, which integrates finite element analysis (FEA) with the MAC/GMC (Micromechanics Analysis Code with Generalized Method of Cells) and the CARES/*Life* (Ceramics Analysis and Reliability Evaluation of Structures / Life Prediction) programs, was used to simulate the formation of mudcracks during the cooling of a multilayered environmental barrier coating (EBC) deposited on a silicon carbide substrate. FEAMAC/CARES combines the MAC/GMC multiscale micromechanics analysis capability (primarily developed for composite materials) with the CARES/*Life* probabilistic multiaxial failure criteria (developed for brittle ceramic materials) and Abaqus (Dassault Systèmes) FEA.

In this report, elastic modulus reduction of randomly damaged finite elements was used to represent discrete cracking events. The use of many small-sized low-aspect-ratio elements enabled the formation of crack boundaries, leading to development of mudcrack-patterned damage. Finite element models of a disk-shaped three-dimensional specimen and a two-dimensional model of a through-the-thickness cross section subjected to progressive cooling from 1,300 °C to an ambient temperature of 23 °C were made. Mudcrack damage in the coating resulted from the buildup of residual tensile stresses between the individual material constituents because of thermal expansion mismatches between coating layers and the substrate. A two-parameter Weibull distribution characterized the coating layer stochastic strength response and allowed the effect of the Weibull modulus on the formation of damage and crack segmentation lengths to be studied. The spontaneous initiation of cracking and crack coalescence resulted in progressively smaller mudcrack cells as cooling progressed, consistent with a fractal-behaved fracture pattern. Other failure modes such as delamination, and possibly spallation, could also be reproduced. The physical basis assumed and the heuristic approach employed, which involves a simple stochastic cellular automaton methodology to approximate the crack growth process, are described. The results ultimately show that a self-organizing mudcrack formation can derive from a Weibull distribution that is used to describe the stochastic strength response of the bulk brittle ceramic material layers of an EBC.

Nomenclature

Symbols

α	thermal expansion coefficient

$\overline{C}$	Shetty shear-sensitivity coefficient (see Nemeth, Jadaan, and Gyekenyesi, 2005).
E	Young's modulus
ε_{xx}, ε_{yy}, ε_{zz}	strain in the x-, y-, and z-directions, respectively
m_V	Weibull modulus for volume-based analysis or as a function of volume
P_{fV}	component failure probability
V	volume
x,y,z	location in the body of the structure
ν	Poisson's ratio
μ	micro (10^{-6})
σ_{0V}	Weibull scale parameter for the volume-flaw failure mode normalized to unit volume
σ_x, σ_y, σ_z	normal stress components parallel to the x-, y-, and z-coordinate directions, respectively
τ_{xy}, τ_{yz}, τ_{zx}	shear stress components in the xy, yz, and zx rotational planes

Subscripts

V	volume or a volume-based property (e.g., indicates volume-flaw analysis)

Definitions

2D	two-dimensional
3D	three-dimensional
APS	air plasma spray
BSAS	barium strontium aluminosilicate, $Ba_{1-x}Sr_xAl_2Si_2O$
CARES/*Life*	Ceramics Analysis and Reliability Evaluation of Structures life prediction program
channel crack	a crack intersecting and perpendicular to a surface, where the length of the crack along the surface is substantially larger than the penetration depth of the crack
CMAS	calcium-magnesium-aluminum-silicate, $CaO\text{-}MgO\text{-}Al_2O_3\text{-}SiO_2$
CMC	ceramic matrix composite
CTE	coefficient of thermal expansion
EBC	environmental barrier coating
FE	finite element
FEA	finite element analysis
FEAMAC/ CARES	Finite Element Analysis—Micromechanics Analysis Code/Ceramics Analysis and Reliability Evaluation of Structures program
MAC/GMC	Micromechanics Analysis Code with Generalized Method of Cells
mode I	crack-opening mode
mode II	crack-sliding mode (in-plane shear)
mode III	crack-tearing mode (out-of-plane shear)
mudcrack	a channel crack and including the subsequent cracking network which are caused by the differential shrinkage of material layers
mullite	$Al_6Si_2O_{13}$, intermediate coat of EBC system (Figure 2)
PIA	Principle of Independent Action
RUC	repeating unit cell
SEM	scanning electron microscope
Si	silicon, bond coat in EBC system (Figure 2)
SiC	silicon carbide, substrate in EBC system (Figure 2)
SPH	smooth particle hydrodynamics method (Sanchez, Osvaldo, and Guimaraes, 2014)
TBC	thermal barrier coating
TGO	thermally grown oxide
YbMS	ytterbium monosilicate, Yb_2SiO_5, topcoat and/or top surface layer of EBC system (Figure 2 and Figure 6)

1.0 Introduction

Thermal and environmental barrier coating (TBC and EBC) systems are used to protect hot-section components in aerospace gas turbine engines that are exposed to the highest temperature environment. They are typically multilayered material systems that are intended to provide both thermal insulation and environmental protection (against chemical attack) of the underlying substrate. EBCs are applied to ceramic substrates (typically silicon-carbide- (SiC-) based composite) whereas TBCs are primarily applied to superalloy substrates. TBCs based upon yttria-stabilized zirconia are now widely used in combination with alumina forming metallic bond coats to slow the thermally activated degradation of internally cooled superalloy substrates (by oxidation and hot corrosion). They often exploit porosity to reduce the in-plane coating modulus and increase their resistance to delamination during thermal cycling. Conversely, EBCs are designed to protect silicon-carbide-based ceramic matrix composite (CMC) components that are increasingly being used in gas turbine engines (Lee and Miller, 1996; and Lee, 2000a, 2000b, and 2015). The main objective of an EBC is to impede access of oxidizing species to the underlying SiC component while maintaining adherence over long durations (typically 25,000 hours). Porosity cannot be used to reduce thermal strain incompatibilities of the system components, leading to increased vulnerability to failure by delamination (when layer coefficients of thermal expansion (CTEs) are less than that of the substrate) or by formation of cracking networks known as "mudcracks" (Wikipedia contributors, 2019; discussed in Section 2.1, Mudcracking) if EBC layers have higher CTEs than the substrate. Failure of an EBC leads to a rapid reduction in CMC component life by allowing oxidation of the Si and then

oxide layer erosion by reactions with water vapor. Key contributors to EBC and CMC failure therefore include oxygen-induced oxidation, water-vapor-induced recession, water-vapor-induced oxidation, degradation by calcium-magnesium-aluminum-silicate, (CMAS: CaO-MgO-Al_2O_3-SiO_2) deposits, thermal and thermomechanical strains, particle erosion, and foreign object damage (FOD). In this report a thermal-driven damage mechanism that leads to formation of mudcracks in an EBC is simulated using a specialized computer program: FEAMAC/CARES, which integrates finite element analysis (FEA) with the MAC/GMC (Micromechanics Analysis Code with Generalized Method of Cells) and the CARES/*Life* (Ceramics Analysis and Reliability Evaluation of Structures / Life Prediction) programs. A key aspect here is using a probability distribution function to describe the initiation of mudcracking events along with a stochastic cellular automaton approach to promote crack propagation. Some of the experimental results from Richards (2015) and Richards et al. (2016) are used for an example to demonstrate this. The physical basis we assumed and the heuristic approach we employed to approximate the crack growth process, is described herein. The results ultimately show that self-organizing mudcrack formation can result from a Weibull distribution that is used to describe the stochastic strength response of the bulk brittle ceramic material layers of an EBC.

The report is organized as follows: Section 2.0 describes the overarching chemical stability issues that are confronted when trying to develop operational EBCs. Section 3.0 defines and describes the aspects of mudcrack formation that we are attempting to simulate, describes our solution approach, and outlines the demonstration problem we chose to analyze. Section 3.0 also describes the software used to perform this work. Section 4.0 describes in detail the example problem, taken from open literature, of mudcracking that occurred in an EBC when the material was cooled down from an annealing temperature of 1,300 °C to room temperature. Section 5.0 describes simulation of mudcrack growth through the individual material layers of the EBC and how average crack segmentation length changes with the value of Weibull modulus. Section 6.0 describes simulation of mudcrack growth on a 1.0-cm-diameter EBC-coated disk on a ceramic substrate. This section shows how mudcrack-patterned damage develops on the EBC-coated surface and how the density of the mudcrack cells are affected by the value of the Weibull modulus assumed. Section 7.0 summarizes the key findings of this report. An appendix briefly reviews the literature on failure mechanisms, mudcrack characterization, and modeling.

2.0 EBC Thermochemical Challenges

EBCs are designed to help protect the SiC materials in the CMC. In the high-temperature environment of the turbine engine, oxidizing species such as H_2O and O_2 react with SiC to form gaseous CO and a solid SiO_2 layer on the SiC surface. In a dry oxidizing environment, this silica layer provides a level of protection to the SiC substrate. However, in a water-vapor-rich combustion environment, rapid reactions of the silica layer with water vapor leads to the conversion of the silica to gaseous $Si(OH)_4$ and other silica hydroxides. As a result, the SiC is eroded (volatilized) at a rate that increases with temperature, water vapor pressure, and flow rate over the surface (Costello and Tressler, 1986; Opila and Hann, 1997; Opila, Fox, and Jacobson, 1997; Opila et al., 1999; and Opila, 1999 and 2003).

Commercially viable EBCs need to be thermochemically stable, highly impervious to moisture and oxygen transport, phase-stable over the operating temperature range, tolerant to thermal strains arising from the cyclic nature of the operation, and resistant to impact from foreign particles. They need to provide protection from oxidizing species penetration (either by gas phase permeation through pinholes and cracks or solid-state diffusion through the coating) and remain adherent to the substrate during prolonged thermal cyclic exposures and thermal shock loading. EBC integrity is challenged further by the presence of siliceous minerals (e.g., dust, sand, volcanic ash, and runway debris) ingested with the intake air. These contaminants deposit onto the coated surfaces of the components, yielding glassy melts of CMAS at high operating temperature (e.g., see Levi et al., 2012).

EBC systems seek to impede this loss of SiC by using coating materials that inhibit transport of oxidizers to the SiC, ideally by intercepting and reacting with the oxidizer species to form a stable thermally grown oxide (TGO) layer. For applications that have substrate temperatures up to 1,316 °C, an applied layer of Si (bond coat) is widely used to help the other EBC layers adhere to the substrate since its CTE is similar (within about 10 percent) to that of SiC (Ghosn, Zhu, and Miller, 2005; and Richards et al., 2016). This similarity greatly reduces the difference in the stress that would develop between the bond coat and substrate during application of a thermal load (due to CTE mismatch). However, thermal cycling with these materials cause the progressive formation of a β-cristobalite TGO layer that undergoes a large contraction upon cooling because of a $\beta \rightarrow \alpha$ phase change upon cooling. This results in the development of internal tensile stresses, which leads to cracking of the TGO as it thickens. The repetition of this phase transformation (from thermal cycling) with progressive cracking leads to further growth of the TGO layer and failure of the system by spallation (e.g., Richards, Begley, and Wadley, 2015). Lee (2018) provides a discussion of this topic and particular TGO growth mitigation efforts.

The rate of bond coat oxidation in an EBC system is usually reduced by the deposition of a diffusion barrier layer on the

bond coat to reduce the flux of oxidizing species that reaches the bond coat surface. Numerous rare earth silicates have been explored, but the system with the best thermal expansion coefficient match to the SiC/bond coat system was identified as $Yb_2Si_2O_7$ (ytterbium disilicate). However, this system suffers significant erosion when exposed to steam, and an attempt has been made to use more steam-erosion-resistant Yb_2SiO_5 (ytterbium monosilicate; YbMS) on the topcoat of the EBC system (Richards, Begley, and Wadley, 2015).

2.1 Mudcracking

For the EBC reported in Richards et al. (2016), the higher CTE of YbMS than the other coating layers of the EBC and substrate resulted in the development of high tensile stresses in the topcoat (made of YbMS) of the EBC multilayered system as both the EBC and substrate cooled from an initial (stress free) annealing temperature. The differential thermal contraction of the individual EBC coating layers and substrate led to the development of high tensile stresses in the top layer, which resulted in the formation of surface-exposed cracks, otherwise known as channel cracks, on the top exposed surface. A channel crack is a crack that intersects and is perpendicular to a surface, where the length of the crack along the surface is substantially larger than the penetration depth of the crack. The crack is v-shaped in cross section where the "v" is open at the exposed surface and tapers downward with depth. These cracks provide rapid transport paths for oxidizers to the bond coat. TBCs are also susceptible to channel cracking.

Individual channel cracks grow in length as cooling proceeds and/or with additional cyclic thermal loading. During these processes, the cracks intersect one another, eventually forming an interconnected network of cracks. The undamaged EBC material that is surrounded or enclosed by these cracks form polygonal-shaped cells (when viewed from above the surface, a birdseye view). This formation of cracking is classified as a "mudcrack" or "mud crack" (e.g., Richards et al., 2016) and is also related to, and can be referred to as, "mudflat cracks" (e.g., Strangman et al., 2007), "desiccation cracks" (e.g., Sanchez, Manzoli, and Guimaraes, 2014) or "shrinkage cracks" (e.g., Kindle, 1917). This type of crack is hereinafter referred to as a "mudcrack," and an interconnected network of mudcracks, as "mudflat cracks." Mudcracks are most commonly associated with the outcome of the fracturing process of drying mud. The formation of mudcracks, and the subsequent cracking network, are caused by the differential shrinkage of material layers:

1. Complete mudcracks form an interconnected tessellating network (mudflat cracks).
2. Incomplete mudcracks are not connected to each other but still form in the same region or location as the other cracks.

Figure 1 provides two examples of complete mudcracking. Figure 1(a) shows the mudcracking network on an EBC after heat flux testing. These cracks are formed by the differential shrinkage of the EBC material layers due to their CTEs. Figure 1(b) provides an example of fossilized mudcracks formed from desiccation of Martian soil approximately 3.5 billion years ago.

Application of mechanical loads (such as tensile or bending) also provide a means to induce channel cracking. In addition, with the application of larger or cyclically applied steady-state

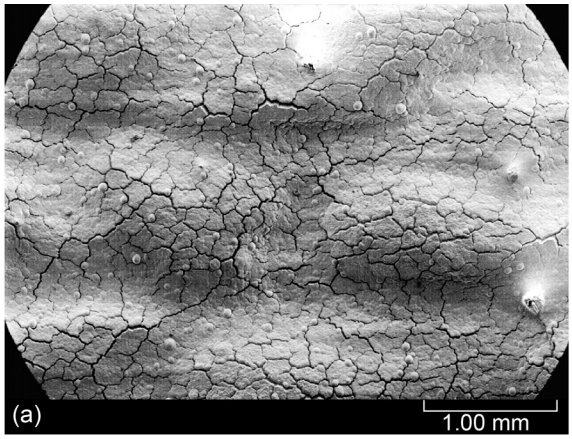

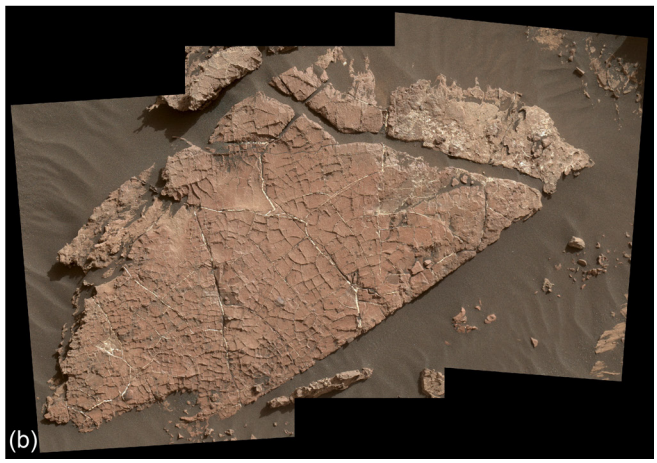

Figure 1.—Examples of complete mudcracking.
(a) Multicomponent (multilayered) rare earth silicate EBC after heat flux testing (photo provided by D. Zhu).
(b) Fossilized desiccation mudcracks solidified on Martian rock: Mastcam image of Old Soaker rock slab taken on Sol 1,555. The red-toned bed is covered by ridges that are remnants of sediment that filled cracks that formed in a drying lake in Gale Crater approximately 3.5 billion years ago. Slab is about 80 cm across.

loading, mechanical loads can form patterns of regularly spaced channel cracks on the EBC. We consider this kind of cracking as being phenomenologically separate from thermally induced or desiccation mudcrack formation, although the mechanics behind the process of crack initiation and growth will be similar. The existence of channel cracks (which include mudcracks as a type of channel cracking) provide a fast transport path of heated combustion products and air that attacks and damages the underlying coating layers. It is therefore important to understand the mechanisms behind this process and be able to replicate, through computer simulation, the formation of mudcracking. Achievement of this would help enable development of a more physically based, and accurate, life prediction and simulation methodology, which could be used to provide more informed safe-life design margins and ultimately provide a new means to help develop coatings that have improved performance.

TBCs and EBCs can show similar mechanical failure modes such as mudcracking, layer delamination, and spallation, but each for different reasons. Mostly, these failure modes are driven by stresses that develop because of the thermal expansion mismatch between the different material constituents of the coating layers and the substrate from temperature change. Generally, it is the substrate that drives the response of the system, because of the substrate thickness being much larger relative to the coating layers. In the TBC system, the CTE of the metallic substrate is generally larger than that of the ceramic overcoatings, and this compresses the coating layers as they cool from an initial annealing processing temperature. In the EBC, the CTEs between the coating constituents and the substrate are likely to be more evenly matched, usually resulting in tensile residual stress profiles in at least some of the individual coating layers in the fabricated system.

Failure or damage in coatings are determined by a variety of factors. These factors include the nature of the stress states in the various coating layers, whether they are compressive or tensile, magnitude of stresses, in what combination and relative location to one another, the nature and orientation of intrinsic flaws within the coating layer (such as porosity), and the localized undulations and roughness (topography) of the coating surface and material interfaces. This topography consists of local (and usually periodic) undulations in the coating layers that provide locations for stress concentration and therefore cracking initiation sites. Herein, the effect of coating layer topology (the geometrical description of the periodic nature of these undulations) on failure initiation and propagation via changes in crack-driving forces (albeit an important topic) is not considered, as each material layer constituting the coating architecture is assumed to be uniform (or flat). However, the effects of local layer topography and coating microstructure are accounted for by adjusting the averaged or bulk material properties imposed; for example, the average strength associated with a given layer. In this way a probability distribution for the various properties can be invoked to indirectly account for local fluctuations in topography as well as microstructure. This would enable all calibrations of the model to be done through material parameter adjustment for both deformation and damage.

Related technical literature regarding coating mechanics and failure mechanisms, mudcrack characterization, and mudcrack modeling, are provided in the appendix (which is only a limited survey of these research areas).

2.2 Simulation of Mudcracking in an EBC

This report examines the feasibility of using the FEAMAC/CARES (Nemeth et al., 2016a) stochastic strength-based damage simulation software tool to predict the formation and coalescence of mudcracks due to cooldown of an EBC system placed on a ceramic substrate. The EBC analyzed here is a YbMS system on a SiC substrate as described in Richards et al. (2016) under a cooldown from an initial (residual stress free) annealing temperature to room temperature. The buildup of residual stresses in the EBC coating layers from thermal expansion mismatch caused the formation of mudcracks as the EBC cools. We consider this to involve both a thermal (driven by temperature) process and a mechanical (resulting from the initiation and growth of cracks) process. The complex chemical and mechanical synergistic interactions that take place on the EBC while operating in a turbine engine is not considered here (i.e., transport and reaction of chemical species such as formation of a TGO layer or surface recession from volatilization). Nor is the existence of any viscous or creep effects assumed to be present. The current methodology employs elastic modulus reduction of randomly damaged finite elements (FEs) to represent discrete cracking events in FEA. The use of many small-sized low-aspect-ratio FEs,[1] along with a simplified cellular automaton failure procedure of the highest failure probability elements, enabled the formation of crack boundaries that led to the development of mudcrack patterned damage. This is demonstrated with examples involving FE models of a button-sized disk-shaped 3D (three-dimensional) specimen, and a 2D (two-dimensional) plane stress model of through-the-thickness cross section of a multilayered EBC coating on a ceramic substrate. The 2D model has a highly detailed mesh (element density) through the depth of the coating layers. This enabled the locations of mudcracking initiation and the

[1] Aspect ratio is the measure of an element's deviation from having all sides of equal length. An aspect ratio of 1.0 means an element has all sides of equal length. Low-aspect-ratio means the aspect ratio is closer to 1.0 (unity) in value.

subsequent crack growth progression through the coating layers to be observed. The 3D model of the button-sized disk was, by necessity, a lower fidelity model because of limitations of the available computer resources. It has larger sized elements and therefore fewer elements through the coating layers compared to the 2D model. Limitation of available computer memory and excessively long computation times involved necessitated this approach. All simulations were performed with an Intel Xeon E5-1650 v4 processor running at 3.6 GHz with 64 GB of memory using a single central processing unit. Memory was allocated with heap arrays using the Intel® Fortran compiler (Intel® Visual Fortran Composer XE 2013). The heap array enables large-sized arrays to remain in memory and avoid paging. The FEAMAC/CARES code had not been optimized for parallelized computation. The 3D model simulations had sufficient fidelity to enable the depiction of the polygonal-patterned mudcrack network formation on the disk surface. All models were subjected to a progressive cooldown from an initial annealing temperature of 1,300 °C to room temperature, and it was assumed there was no thermal gradient present (an isothermal condition). This established the initial damage state and residual stress state profile of the material prior to any service application. Mudcrack damage in the coating system resulted from the buildup of residual tensile stresses between the individual material constituents from thermal expansion mismatch. A two-parameter Weibull distribution was used to characterize the coating layer stochastic strength response and the effect of three different values of Weibull moduli m_V where m_V = 2.5, 5.0, and 10.0, on the formation of mudcrack damage is contrasted here on the 2D and 3D models. The spontaneous initiation of cracking and crack coalescence resulted in progressively smaller mudcrack cells as loading progressed, consistent with a fractal-behaved fracture pattern.

3.0 FEAMAC/CARES

FEAMAC/CARES was initially developed to simulate the stochastic-based, discrete-event progressive damage of composite material structures. It involves coupling three independently developed software programs: (1) the Micromechanics Analysis Code with Generalized Method of Cells (MAC/GMC) (Aboudi, Arnold, and Bednarcyk, 2012; Bednarcyk and Arnold, 2002a and 2002b) with finite element analysis (FEAMAC) (Bednarcyk and Arnold, 2007), (2) the Ceramics Analysis and Reliability Evaluation of Structures Life Prediction Program (CARES/*Life*) (Nemeth et al., 2003; and Nemeth, Jadaan, and Gyekenyesi, 2005), and (3) the Abaqus FEA program (Dassault Systèmes, 2013). MAC/GMC contributes multiscale modeling capabilities and micromechanics relations to determine stresses and deformations at the microscale of the composite material repeating unit cell (RUC). FEAMAC combines MAC/GMC with FEAs and enables progressive damage to develop over time (or with sequentially applied loading steps). CARES/*Life* contributes stochastic multiaxial failure criteria that can be applied to the individual brittle material constituents of the RUC, including anisotropic strength and damage orientation response (Nemeth, 2013a, 2013b, 2014a, and 2014b). Abaqus is used at the global scale to model the overall geometrical structure of the component and imposed loading. An Abaqus user-defined material interface, referred to here as "FEAMAC/CARES," was developed that enables MAC/GMC and CARES/*Life* to operate seamlessly with the Abaqus FEA code. For each FEAMAC/CARES simulation trial, the stochastic nature of brittle material strength results in random, discrete damage events, which incrementally progress over time or dynamic loading.

To represent a discrete failure event, FEAMAC/CARES reduces the elastic modulus of an element's integration point by 99 percent when material failure is indicated at that location during a simulated loading sequence. This failure evaluation is done using CARES/*Life*. The use of many small-sized low-aspect-ratio FEs in the structural model enables the depiction of crack boundaries and formation of mudcrack patterned damage. However, this requires the use of a great many elements to obtain sufficient fidelity to represent individual discrete crack initiation and crack growth events. At the start of a simulation run, the individual FE integration points of a FE model are seeded with randomly assigned probabilities of failures from a uniform probability distribution. When the CARES/*Life* calculated probability of failure (for the particular element integration point and associated element integration point volume) exceeds the randomly assigned probability of failure at some point in the loading sequence, the elastic modulus of the particular element integration point is reduced by 99 percent (which is maintained for the remainder of the simulation). FEAMAC/CARES also employs a simple cellular automaton methodology that adjusts the previously assigned random failure probabilities of elements adjacent to a failed element. This helps produce crack-like or crack-mimicking growth patterns as opposed to more random failure patterns. The methodology is detailed further in Nemeth et al. (2016a). We do not explicitly consider the stress singularity that occurs at the tip of a crack. Instead, a heuristic or approximation methodology is used that captures some of the far-field effects cracking has on the surrounding medium. As such, it was adequate for our purposes of demonstrating the spontaneous formation and self-organization of mudcracking and how it originates from a Weibull distribution that is used to describe brittle material strength response.

In this report FEAMAC/CARES is applied in its original form as described in Nemeth et al. (2016a) to a novel application—the simulation of mudcrack formation. It is a follow-on or companion report regarding the development and applications of FEAMAC/CARES. This approach uses the Weibull distribution to describe and characterize the fracture strength and failure

probability of the various brittle material constituents (coating and substrate) of the overall structural system. This use of the Weibull distribution to describe the stochastic strength response of the brittle material constituents of thin films has been previously employed (in the literature we examined) by Cassenti (1991), who derived a crack spacing segment size probability distribution from simple tensile loading, and by Yanaka et al. (2001), who use FEA and Monte Carlo simulation to determine the distribution of mudracking fragment lengths. In the current study a single-material MAC/GMC subcell is used to represent each FE Gaussian integration point. We do not consider, in this report, the further possibility of using FEAMAC/CARES with more complicated RUC architectures to define the particular constituents/phases of each coating layer in a multiscale manner (e.g., various crystallite phases, porosity, or nanotube reinforcement). That further analysis is saved for future work. Regardless, FEAMAC/CARES provides the necessary progressive damage analysis capability and provides all the bookkeeping required to track damage at the individual element integration point level. The multiscale capability of the MAC/GMC framework is a defining feature of FEAMAC (Bednarcyk and Arnold, 2007). FEAMAC/CARES was originally developed to model the multiscale response of ceramic- and polymer-matrix composite materials. Here, this software is used to simulate how mudcracks naturally arise from the variability of the extant natural flaws in the coating material layers.

The core of the CARES/*Life* software (Nemeth et al., 2003; and Nemeth, Jadaan, and Gyekenyesi, 2005) is used as a callable subroutine within MAC/GMC, and it describes the probabilistic nature of brittle material strength using the Weibull cumulative probability distribution function (Weibull, 1939). For uniaxially stressed components, the two-parameter Weibull distribution for volume-residing flaws describes the, in what is termed "fast-fracture" or strength-based fracture, as

$$P_{fV} = 1 - \exp\left[-\frac{1}{\sigma_{0V}^{m_V}} \int_V \sigma(x,y,z)^{m_V} \, \mathrm{d}V \right] \tag{1}$$

where V is the volume (terms that are a function of volume have V in the subscript), $\sigma(x,y,z)$ is the uniaxial stress at a point location in the body with spatial coordinates x, y, and z; and m_V and σ_{0V} are the shape and scale parameters of the Weibull distribution, respectively. The shape parameter is a measure of the dispersion of strength, and the scale parameter is the strength of a unit volume of material in uniaxial tension at 63.21 percent probability of failure. Three values of m_V = 2.5, 5.0, and 10.0 were chosen for this study and are representative values of brittle materials. As the value of m_V increases, the strength dispersion (scatter in strength) decreases.

Equation (1) is the basic two-parameter Weibull equation used within CARES/*Life* and is provided here for convenience because of its simplicity and ease of understanding. However, CARES/*Life* has extensions to this equation for handling the effect of multiaxial stresses on stochastic strength response. This is done with the Batdorf Unit Sphere theory (Batdorf and Crose, 1974; and Batdorf and Heinisch, 1978). The Batdorf model was used for this report. The Batdorf Unit Sphere theory incorporates concepts of linear elastic fracture mechanics by assuming a brittle material incorporates randomly oriented strength-controlling flaws of an assumed geometry. A mixed-mode fracture criterion describes how these flaws respond to a multiaxial stress state. The various references cited here by Nemeth and coauthors describe extensions of this methodology for situations such as slow crack growth, cyclic loading and fatigue, transient loading, and transversely isotropic strength response. Those extensions are not described further here. The strength-controlling flaws distributed in the material volume are assumed to be penny-shaped cracks, governed by a mixed-mode fracture criterion of Shetty (1987), having a shear-sensitivity parameter of $\overline{C}$ = 1.0 (a moderately strong shear-sensitive or mode II response) that describes the relative role modes I and II stress intensity factors have on one another with regard to crack growth initiation (see also Nemeth et al., 2003; and Nemeth, Jadaan, and Gyekenyesi, 2005).

In this report we do not consider failure from compression. The CARES/*Life* methodology does have a simple Tresca, or maximum shear stress, failure mode that is applied to the Batdorf Unit Sphere methodology for isotropic brittle materials (see Nemeth, 2013a and 2014b). That failure mode analysis option was not used here. Generally, brittle materials are substantially stronger in compression fracture than in tension fracture (not considering a buckling failure mode).

4.0 Simulated EBC System

The EBC considered here is a YbMS system on a SiC substrate as described in Richards et al. (2016). The YbMS EBC system was subjected to a cooldown from the residual-stress-free annealing temperature of 1,300 °C to room temperature (23 °C). The buildup of residual stresses in the EBC coating layers from thermal expansion mismatch caused the formation of mudcracks as the EBC cooled. A component composed of this EBC and substrate combination will similarly have an initial residual stress and damage state in the material system prior to being placed into a service load condition. It is necessary to know, and account for, this initial residual stress profile and damage state in the EBC/substrate material system so that allowable service loads and safe life can be more accurately determined. This report examines a modeling methodology that can establish this initial state of residual stresses and damage within an EBC material system. The FEAMAC/CARES software is generalized so that it should be capable of simulating the additional damage that develops in

the EBC from subsequent (and repeated) service loadings. This more generalized capability is not demonstrated in this report.

The system studied consisted of a silicon carbide (SiC) substrate with a trilayer EBC consisting of a silicon (Si) bond coat, a mullite ($Al_6Si_2O_{13}$) intermediate coat, and a ytterbium monosilicate (YbMS) topcoat with the chemical formula Yb_2SiO_5. The bond coat helps impede transport of oxygen or water vapor that had penetrated the outer coating layers by forming a protective TGO. This TGO reaction consumes oxidizing species that reach the bond coat and creates a diffusion barrier to delay the transport of oxidizing species to the substrate. The intermediate mullite layer serves as an oxidizing diffusion barrier while also preventing potential solid-state reactions between thermally grown silica on the bond coat and the topcoat. The YbMS topcoat serves as a low-silica-activity compound with a very low recession rate in environments containing water vapor. The EBC system was deposited using an air plasma spray (APS) process (see Richards et al., 2016; and Richards, 2015 for further details). A schematic of the coating system is shown in Figure 2 with average individual layer thicknesses indicated.

The trilayer coatings were deposited onto the grit-blast-roughened 25.4-mm by 12.7-mm rectangular-shaped surface of a 4.8-mm-thick α-SiC Hexoloy™ substrates (Saint Gobain Ceramics). The deposition of all layers was performed at 1,200 °C with each layer requiring roughly 10 s to deposit, and the coated samples were subsequently annealed at 1,300 °C in laboratory air for 20 h to transform metastable phases typically found in the as-deposited YbMS and mullite layers.

In this report a different specimen geometry was used for simulation than the original rectangular specimen Richards et al. (2016) used: instead, a round disk-shaped specimen was chosen. This was a somewhat arbitrary choice, but it avoided any issues with resolving the stresses at the specimen's four corners and provided a desirable situation of a uniform constant stress profile about the specimen periphery. This geometry also provided an opportunity to visually compare (in a subjective manner) our simulated mudcrack polygonal fracture cell formation to an experimental result of drying mud in a round petri dish (Figure 25 shown in Section 6.0, 3D Finite Element Model of Disk With EBC and Substrate).

The CTEs of the YbMS and (to a lesser extent) mullite layers were significantly higher than that of the SiC substrate (see Table I), and they are assumed to be responsible for the mudcracking of the YbMS and mullite layers after stabilization annealing at 1,300 °C. The FEAMAC/CARES simulations used the same elastic moduli values as were used by Richards et al. (2016). These values were somewhat arbitrarily reduced 50 percent from corresponding dense (bulk) material properties.

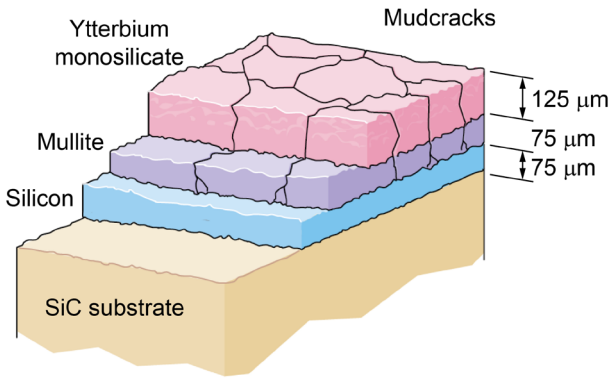

Figure 2.—Ytterbium monosilicate EBC on SiC substrate with mudcracks sketched in. Average coating layer thicknesses are indicated. Figure adapted from Richards et al. (2016).

TABLE I.—TENSILE AND WEIBULL PARAMETERS OF TRILAYER EBC SYSTEM

[Weibull modulus values set at 2.5, 5.0, and 10 m_V.]

Material: layer position	Young's modulus,[a] E, GPa	Poisson's ratio, ν	Coefficient of thermal expansion, α, m/m/°C · 10^{-6}	Weibull scale parameter, σ_{0V}, MPa · mm^{3/m_V}
Top surface layer:[b] ytterbium monosilicate	86	0.27	7.5	40
Topcoat: ytterbium monosilicate	86	0.27	7.5	56
Intermediate coat: mullite	110	0.28	5.3	56
Bond coat: silicon	82	0.223	4.1	80
Substrate: SiC (monolithic)	430	0.14	4.6	321

[a]Young's modulus used by Richards et al. (2016).

[b]Top surface layer refers to exposed surface of topcoat and adjoining nearby material. It describes a thin layer of material having different stochastic strength response (different Weibull parameters) than the rest of the topcoat.

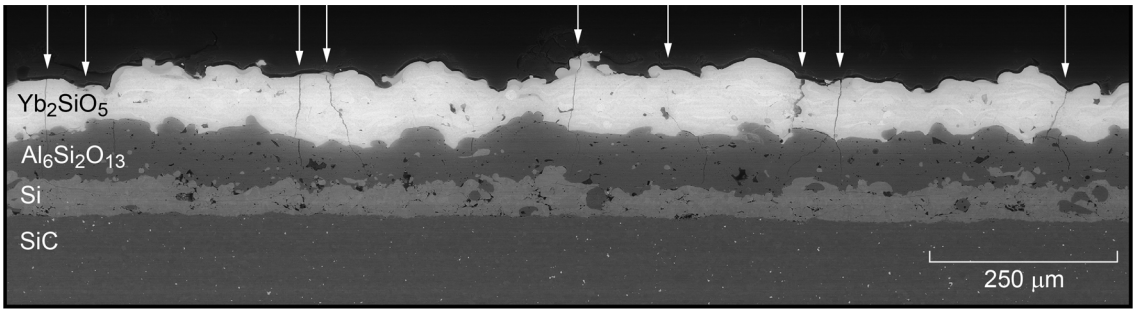

Figure 3.—Periodic crack spacing: image of stabilization-annealed trilayer EBC on SiC substrate, showing periodic spacing of mudcracks (indicated by arrows). Reproduced from Richards et al. (2016).

This reduction was done by Richards et al. to reflect values representative of lower porosity APS-deposited material (e.g., DeMasi, Sheffler, and Ortiz, 1989; Meier, Nissley, and Sheffler, 1991; Cruse, Johnsen, and Nagy, 1997; Leigh, Lin, and Berndt, 1997; Li and Ohmori, 2002; Richards, Begley, and Wadley, 2015; and Richards et al., 2015).

Figure 3, reproduced from Richards et al. (2016), shows a scanning electron microscopy (SEM) micrograph of a cross section of the EBC coating and substrate system after stabilization annealing and indicates the presence of periodically spaced mudcracks in the coating (highlighted by the arrows). The average mudcrack spacing was determined to be 240 μm, determined from a 25-mm span of the coating cross section. Pore volume fraction was found to be ~1 percent in the YbMS layer and ~5 percent in the $Al_6Si_2O_{13}$ and Si layers. Mudcracks were observed to have penetrated the Yb_2SiO_5 and $Al_6Si_2O_{13}$ layers. Unfortunately, no overhead view of the EBC surface showing the surface cracking network of the mudcracks (mudflat) was available (Wadley, 2017, personal communication).

Richards et al. (2016) observed that the mudcracks in the trilayer system frequently branched as they entered the $Al_6Si_2O_{13}$ layer system, and in many cases bifurcated into two cracks. Bifurcation of mudcracks occurred at either the $Yb_2SiO_5/Al_6Si_2O_{13}$ interface (Figure 4(a)), within the $Al_6Si_2O_{13}$ layer (Figure 4(b)), or at the $Al_6Si_2O_{13}$/Si interface (Figure 4(c)). Bifurcation at these three locations was observed with equal frequency, and all bifurcation locations resulted in cracks that propagated along a trajectory towards or within the Si bond coat. Richards et al. developed FE models of double-sided kink cracks that could have emerged from the tips of mudcracks.

Figure 5 provides another interesting visual example of mudcrack bifurcation. The photomicrograph shows vertical "T-shaped" and "Y-shaped" bifurcated oblique-angle mudcracks in immediate proximity to one another. This photomicrograph was taken from a different multicomponent rare earth EBC material system than Richards et al. (2016). In Figure 5 the EBC had undergone thermal gradient cyclic loading with CMAS deposition. This photomicrograph illustrates that different cracking modes can occur in the same material system and can

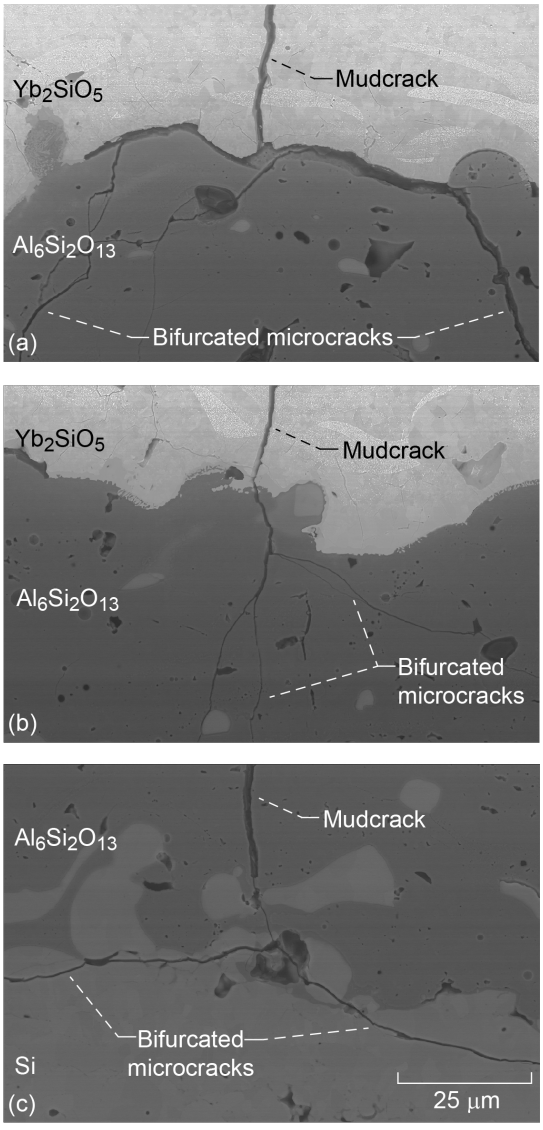

Figure 4.—Examples of mudcrack bifurcation. In all cases, the resultant trajectory of bifurcated crack ligaments was directed toward the silicon bond coat. Figure reproduced from Richards et al. (2016). (a) Bifurcation at the $Yb_2SiO_5/Al_6Si_2O_{13}$ interface. (b) Bifurcation within the $Al_6Si_2O_{13}$ layer. (c) Bifurcation at the $Al_6Si_2O_{13}$/Si interface.

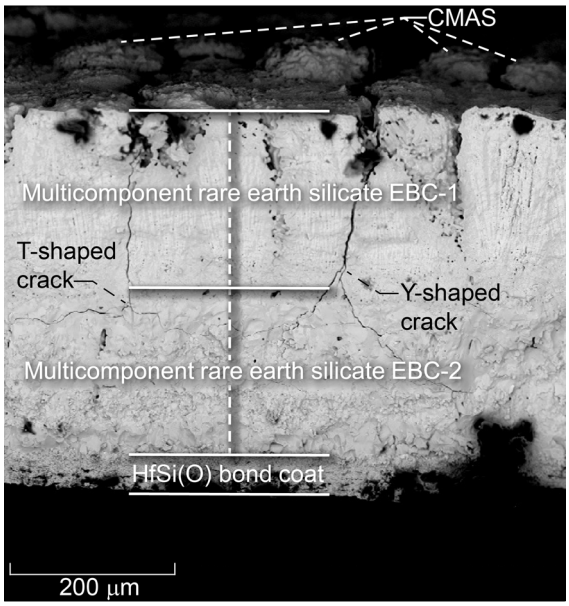

Figure 5.—Multicomponent (multilayer) EBC cracking with calcium-magnesium-aluminum-silicate (CMAS) deposits on top, showing T-shaped and Y-shaped side-by-side mudcrack profiles. Photomicrograph courtesy of D. Zhu.

be located alongside one another. It also indicates that local material fluctuations can lead to different cracking results. The simulations in the current study were capable of capturing the layer delamination that occurred with the T-shaped crack; however, they did not indicate unambiguous instances of oblique-angle crack growth as shown with the Y-shaped crack. Modeling deficiencies greatly suppressed this mode of cracking.

For the YbMS EBC system investigated by Richards et al. (2016), stress calculations indicated that the high CTE of the Yb_2SiO_5 and $Al_6Si_2O_{13}$ layers relative to the SiC substrate result in substantial tensile residual stresses in the YbMS topcoat and mullite intermediate coat layers and result in compressive stresses in the Si bond coat after cooling from the annealing temperature to room temperature. Their calculations assumed material isotropy and ignored any anisotropies present from crystalline phases or textures induced from processing (e.g., splat boundaries from the plasma spray). The mudcracking observed in Figure 3 is consistent with the stress calculations, indicating that the mudcracks appear to have initiated in, or were mostly confined to, the topcoat and less so the intermediate and bond coat layers.

Richards et al. (2016) stated "it should be noted that coating anisotropy can play a significant role in the development of stress and the cracking behaviors that develop in spray-coated systems. However, the present coatings were deposited under conditions that resulted in limited spherical droplet spreading during deposition…Furthermore, the coatings did not exhibit evidence of preferential texture…while as deposited inter-splat boundaries contained microporosity, the stabilization annealing process resulted in substantial sintering and reduction in this porosity before testing. The propagation of cracks during coating failure did not therefore appear to follow splat boundaries." This helps support our (and their) justification in analyzing the coating layers as isotropic materials. However, anisotropies introduced by preferential texture could be handled in a more generalized fashion by transversely isotropic multiaxial strength methodology extensions developed by Nemeth (2013a, 2013b, 2014a, and 2014b) based on Batdorf's Unit Sphere methodology (Batdorf and Crose (1974); and Batdorf and Heinisch (1978)).

5.0 2D Finite Element Model of EBC-With-Substrate Cross Section

Figure 6 shows a 1.8-mm-wide portion of a FE model with overall dimensions of 4 mm wide by 1 mm thick, depicting a 2D cross section of the three coating layers and the substrate. Showing the whole model would cause difficulty in viewing the closely spaced mesh gridlines. The model is composed of shell elements, and therefore plane stress conditions apply (stress in the z-direction is always zero in Figure 6). This model provides a high-density mesh through the thickness with many low-aspect-ratio elements that span each coating layer. This enables the detailed depiction of individual mudcracking events. The "top surface layer" is actually part of the topcoat, as it is composed of the same material. Its presence and purpose in the model is described in the subsequent paragraph. The top surface layer and the topcoat are YbMS material. The intermediate coat in the figure is mullite. The bond coat is Si and the substrate is SiC. The width and thickness dimensions of the FE model were arbitrarily chosen, but with a width sufficient such that edge effects are negligible for the majority of the width of the model. The edges were unconstrained, which allowed the effect of the edge on the stress distribution and failure modes in these regions to also be examined. The FE model consisted of 55,200 reduced integration S4R shell elements constructed using Abaqus version 6.13 (Dassault Systèmes, 2013). The S4R element type has three centrally located integration points through the thickness of the shell. Our previous experience with FEAMAC/CARES indicated that there was no discernable difference in cracking damage patterns whether reduced integration elements were used or not. Since the reduced integration elements provided faster computation times with a reduced memory requirement, they were used in all of the FE models in this report. Note, the 2D FE model did not account for the effect out-of-plane strains would have had on the in-plane stresses (the term "$\nu\varepsilon_z$" in the generalized stress-strain equations for σ_x and σ_y stress components). To account for this effect in the FEAMAC/CARES damage simulations, a stress

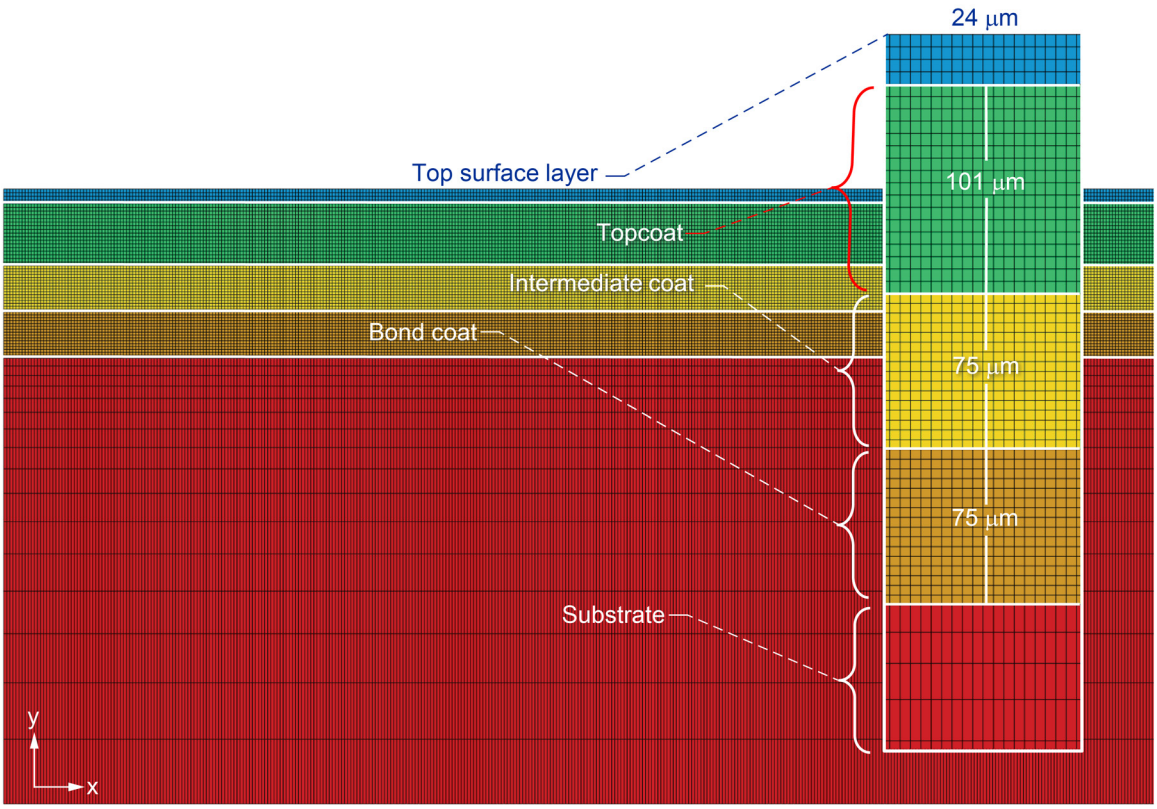

Figure 6.—Shown is a portion of a finite element mesh of the EBC coating layers and substrate. Shown is a 1.8-mm-wide portion of the 4-mm-wide by 1-mm-thick cross section. The top surface layer is ytterbium monosilicate, the topcoat is ytterbium monosilicate, the intermediate coat is mullite, the bond coat is silicon, and the substrate is silicon carbide.

multiplication factor was used (explained later in this section). Regardless, in the FE stress analysis shown here, the trends in the stresses (e.g., tensile versus compressive) in the various material layers relative to each other remained the same despite not considering the out-of-plane strains. Each simulation with FEAMAC/CARES was broken down into 410 temperature load increments: the first 10 equally space increments cooled from 1,300 to 1,200 °C (a range where minimal damage typically occurs) as a ramp load and the next 400 equally spaced temperature increments as a ramp load cooled from 1,200 to 23 °C. No thermal gradient was assumed to be present.

As shown in Figure 6, the elements in the coating layers have low height-to-width aspect ratios of about 1.20 in the top coating layer (top surface layer and topcoat) and a 0.93 height-to-width ratio in the intermediate and bond coat layers. The elements modeling the SiC substrate have higher aspect ratios that increase with the distance away from the boundary between the bond coat and the substrate. This use of high-aspect-ratio elements helped to reduce the total element count. The substrate is significantly stiffer and thicker than the coating layers so that the deformation the substrate experiences from the contraction dominates the response of the system (i.e., the coating has little influence on the overall deformation response of the substrate). In the FE model the bottom of the substrate was constrained in the direction normal to the surface (the y-direction). This was done so that the substrate would act in a more rigid manner and mimic the behavior of a thicker substrate. This constraint enables using fewer elements to model the action a thicker substrate would have.

The inclusion of an additional layer, indicated “top surface layer” in Figure 6, allows for different Weibull strength distribution parameters to be designated for this layer versus the bulk of the topcoat material. The 24-μm thickness for this layer is arbitrary and was composed of four layers of elements through the thickness. It was thought that having four elements or more through the thickness (versus having fewer, or even only one element) would more realistically enable any damage that initiated in this top surface layer to proceed through the layer and continue into the topcoat. Here, the “top surface layer” serves as a proxy for the damaging (degrading) effect surface roughness has on the stochastic strength response of a coating layer (e.g., Chen et al., 2002). EBC coatings usually have an irregular or roughened surface layer, as well as irregular interfacial layers, such as shown in Figure 3. The “top surface layer” was intended to separate the potential degrading effects

of localized stress concentrations that result from this surface roughness on strength of the coating surface from the strength response in the interior (or bulk) of the coating. The top surface layer helps provide an additional control on the damage initiation and damage propagation in the coating system.

Figure 7 shows the stress analysis results in the various coating layers and substrate from the FE analysis of the 2D model after a 100 °C cooldown from 1,300 °C annealing temperature using the properties listed in Table I. This limited cooldown was prior to a first damage event in the EBC system. Since the FE model was composed of 2D shell elements, the effect of out-of-plane strains (z-direction) on the in-plane stresses (the x- and y-directions) was not accounted for in the stress analysis (and therefore not in the results shown in Figure 7). In the rectangular specimens tested by Richards et al. (2016) these strains would have been present. Regardless, our FE stress analysis results confirmed the trends reported in the stress calculations performed by Richards et al. Figure 7(a) shows that a substantial normal tensile stress σ_x in the x-direction is present in the topcoat. This stress is lower in the intermediate coat with an abrupt transition at the boundary between the topcoat and intermediate coat layers. In the bond coat and the substrate compressive stresses are seen. These peak compressive values are less than half as large in magnitude as the tensile stresses in the topcoat. Figure 7(a) to (c) also shows the effect of the unconstrained edges (left and right edges in the figure). In Figure 7(a) the σ_x stress is of relatively low magnitude (tensile or compressive) near those edges in all layers and the substrate. The effect of the edge on the magnitude of the stress can be seen to extend about 1 mm in from the edge towards the center. In Figure 7(b), the σ_y (peel) stress is largely compressive in all EBC layers and the substrate, except at the edges where a substantial tensile stress is seen around the boundary between the Si bond coat and the SiC substrate. The high tensile stress at that boundary (about the left and right unconstrained edges) would certainly indicate a likely location for initiation of delamination failure between the bond coat and the substrate. Figure 7(c) shows the through thickness shear stress component τ_{xy} in the coating layers and substrate. The shear stresses are present in the neighborhood of the unconstrained edges, however, the magnitude of the stress is substantially less than the peak normal tensile stress magnitudes in Figure 7(a) and Figure 7(b).

The large tensile stresses that develop in the YbMS and mullite coating layers as the cooldown proceeds drives the initiation and growth of damage within these coating layers. FEAMAC/CARES was used to simulate the progressive damage development in the EBC from a 1,300 °C cooldown, using the thermomechanical properties listed in Table I. The effect three different values of Weibull modulus (m_V = 2.5, 5.0, and 10.0) had on the development of mudcrack damage and crack segmentation length was investigated. In the EBC material system used in Richards et al. (2016), the values of m_V for the various coating layers were not measured. The temperature when microcracking initiated was also not known in that study. The values of σ_{0V} used in the current study and listed in Table I were instead chosen so that the FEAMAC/CARES simulations provided reasonably comparable average mudcrack segmentation lengths to that of the 240-μm average mudcrack spacing reported by Richards et al. The σ_{0V} parameter values used are one-half of the average coating strengths for the different layers of the EBC material system reported by Abdul-Aziz et al. (2014). There, the topcoat material was barium strontium aluminosilicate (BSAS), the intermediate coat was a mixture of BSAS and mullite, and the bond coat was Si. These were applied by air plasma spray coating. Their material properties and strength values were experimentally determined. The values we chose to use for the Weibull scale parameter provided relatively high crack densities (smaller crack segmentation lengths) compared to the experimental data of Richards et al. This was purposely done so that the final damage (at the end of the simulation) presented more exaggerated or more pronounced failure modes than experimental evidence indicated. Doing so allowed other failure modes, such as delamination, to become more observable. Because of the lack of information regarding measured parameter values and when damage first initiated, the simulation results we subsequently show are more of a qualitative nature rather than a quantitative nature. Regardless, the principles of the methodology and how the stochastic strength of the coating brittle material constituents relate to crack segmentation length are illustrated. Note that it could be possible to back out Weibull modulus and scale parameter values from the damage patterns and failure modes displayed by deposited EBCs, provided sufficiently detailed forensic (and diagnostic) information could be gathered. This process was performed by Yanaka et al. (2001) on a silicon oxide film deposited on a polyethylene terephthalate substrate.

As previously mentioned, the 2D FE model used shell elements, and therefore it did not account for how the out-of-plane strains affected (in the z-direction) the in-plane stresses of a loaded (stressed) 3D body. To help compensate for this deficiency, a stress multiplication factor of 1.363 was used when the FEAMAC/CARES simulations were run. This multiplication factor multiplied all the stress component results from the FE model by a constant value when the CARES/*Life* reliability analysis calculations were being performed within the FEAMAC/CARES simulations. This affected the average mudcrack segmentation length, making it smaller. Note this did not affect stress calculations internally within Abaqus. The value of 1.363 was determined from the ratio of the peak σ_x value (on the topcoat surface in the center of the FE model) of the 3D model of the 10-mm-diameter specimen, described

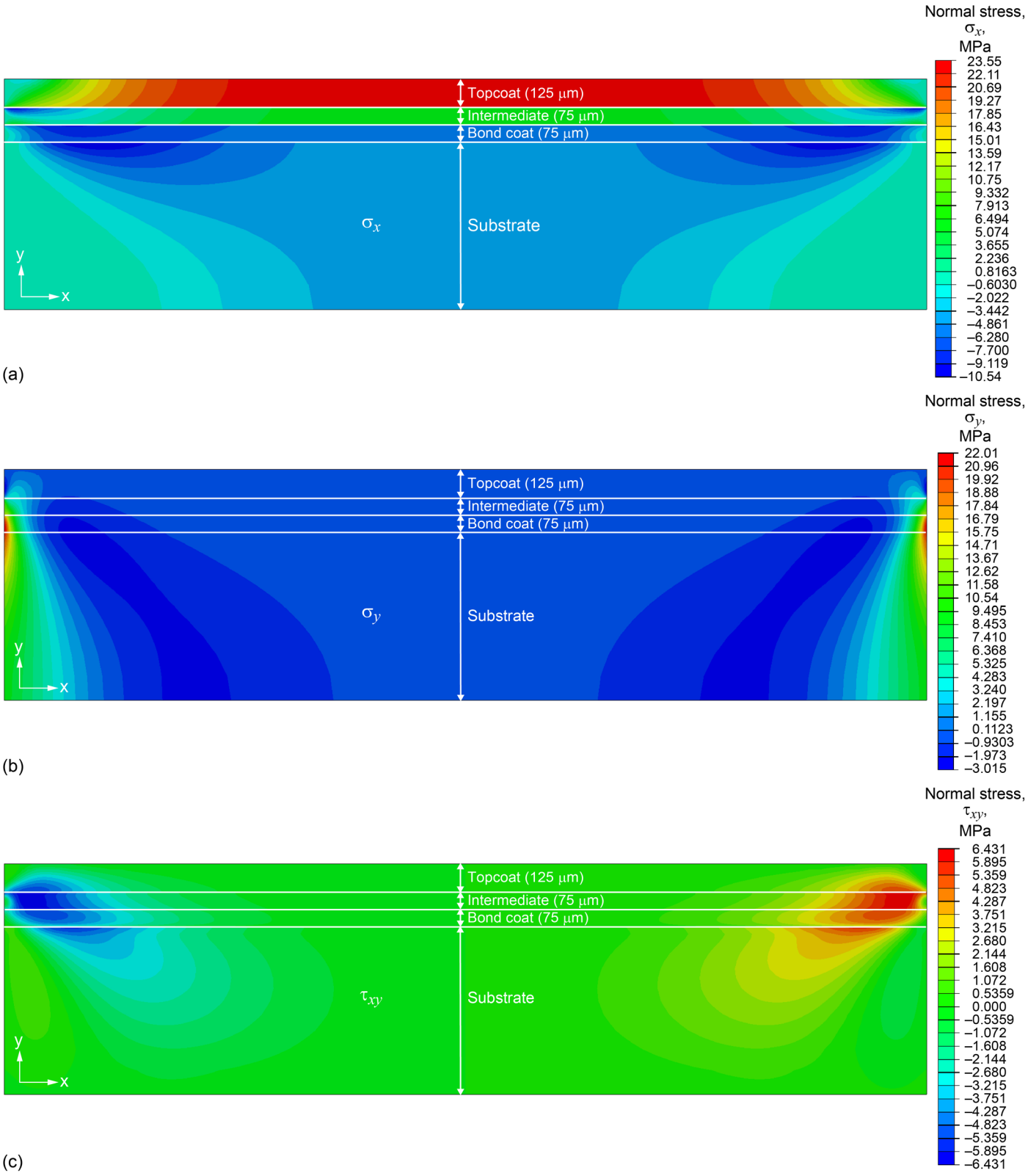

Figure 7.—Stress analysis results from 2D FE model (partially shown in Figure 6) prior to development of damage in EBC layers after 100 °C cooldown from 1,300 °C. Left and right edges are unconstrained, and bottom of substrate is constrained in y-direction. (a) σ_x normal stress profile. (b) σ_y normal stress profile. (c) τ_{xy} shear stress profile.

in Section 6.0, "3D Finite Element Model of Disk With EBC and Substrate," and the peak σ_x value (on the topcoat surface in the center of the FE model) of the 4-mm-wide 2D cross-sectional model per degree of applied cooling (prior to any damage). This meant that the peak stress on the 2D FE model would match the peak stress on the 3D model for a cooldown from 1,300 °C if no damage occurred. This assumed that the effect of the biaxial stress state that occurred on the topcoat surface of the 3D FE model, compared to the uniaxial stress state that occurred on the topcoat surface of the 2D FE model, was less important on the development of damage, such as average crack segmentation length, than the effect of the magnitude of the stress on this development. This contention can be somewhat supported by a simple calculation of failure probability on damage initiation with the PIA (Principle of Independent Action) (Barnett et al., 1967) stochastic strength multiaxial failure model for brittle materials with a uniaxial versus an equibiaxial stress state applied on a unit volume of material (the same comparable calculation can be made with the CARES/*Life* implementation of the more complicated Batdorf Unit Sphere model). This stress multiplication factor was adjusted so that the amount of cracking damage from the 2D cross-sectional FE model simulation runs were, to a reasonable degree, comparable with that of the 3D FE model of the disk and also with the experimental results of Richards et al. (2016). However, the amount of damage in the 3D FE model turned out to be less than expected as will be discussed in Section 6.0, "3D Finite Element Model of Disk With EBC and Substrate."

Figure 8 shows four sequential snapshots of the simulated progressive mudcrack damage development as the 2D model cools down from the initial annealing temperature of 1,300 to 23 °C for a Weibull modulus $m_V = 2.5$ from FEAMAC/CARES. The individual element boundaries in the FE model are not shown. Shown are the individual layers in the EBC system and the corresponding failed elements. The small relative size of the elements and the near 1:1 aspect ratio of the element height (thickness) and width dimensions enables the depiction of the mudcracks, which comprise the progressively (sequentially) failed columns of connected elements as the damage progressed. The formation of this crack-like damage is encouraged by the cellular automaton methodology as described in Nemeth et al. (2016a). Failure can occur anywhere in the FE model. It occurs where a high tensile stress exceeds the local strength of the material. A highly stressed area may also be a high-strength area and therefore will not fail. Crack growth is driven by the concentration of stress (at the crack tip) from the applied loading. When a failure condition is reached at an element integration point, the stiffness of that point is reduced by 99 percent. On the subsequent loading step there is a global redistribution of stresses that occur at and away from the damage. Where there is an intensification of stress, failure could potentially occur. Crack growth direction is largely driven by where damage initiation (element failure) occurs, how stress redistributes about that damage on subsequent loading steps, and the resistance to failure (the local strength) of the element integration point. The cracking depicted here tends to be vertical in nature (normal to the surface, except at the edges) and does not tend to propagate at an oblique angle to the plane of the surface. This is a mesh-dependent issue with the FE model. The cracking pattern closely follows the element layout of the FE mesh. Further investigation and development in the FEAMAC/CARES methodology will be needed to obtain simulation results that also yield oblique angle mudcracking. This remediation may be as simple as using different element types such as prismatic elements or using more sophisticated methodologies to determine preferred crack tip growth orientation trajectories (e.g., O'Brien and Hodgins, 1999; and Paluszny and Matthäi, 2009, both of which involve dynamic local remeshing at a crack tip as the crack advances).

In Figure 8 (and subsequent similar figures) the bottom portion of the substrate is not shown since damage never initiated nor propagated into that portion of the FE model. The cooldown (applied as two sequences of ramp load) occurred over 410 load increments. The first 10 increments were over evenly spread temperature load increments from 1,300 to 1,200 °C, where little or no damage was initiated. The subsequent 400 load increments involved cooling over evenly spaced temperature changes from 1,200 to 23 °C. Each of these FEAMAC/CARES 2D simulations typically took about 3 weeks to run on a personal computer.

In Figure 8(a) the first damage events occurred in the top surface layer, topcoat, and intermediate coat. Once initiated, cracking damage could proceed growing vertically upwards (towards the exposed surface) and downwards (towards the substrate) simultaneously. It would often stop or arrest at a material interface as shown in the remaining Figure 8(b) to (d). As cooling proceeded, new mudcracks would form at dispersed locations. These cracks were usually spaced some distance away from existing cracks. Damage initiation occurred in the region of highest σ_x normal tensile stress shown in Figure 7(a). In Figure 8(b) additional cracks form predominantly in the top surface layer and the topcoat. The cracks appear to arrest at a material interfacial layer. One crack initiated in the intermediate coat, and there appears to be an element failure event in the bond coat at the interface between the bond coat and the substrate (towards the right-hand side of Figure 8(b)). This occurred at 611.5 °C in a region where compressive stresses were present and is an unexplained event. Also there was some cracking initiation in the top surface layer. Proceeding from Figure 8(a) to (e) there was development of multiple cracks in the topcoat that are spaced apart from one another in a somewhat periodic crack spacing arrangement. It is observed that the cracks, for the most part, arrest at the interface between

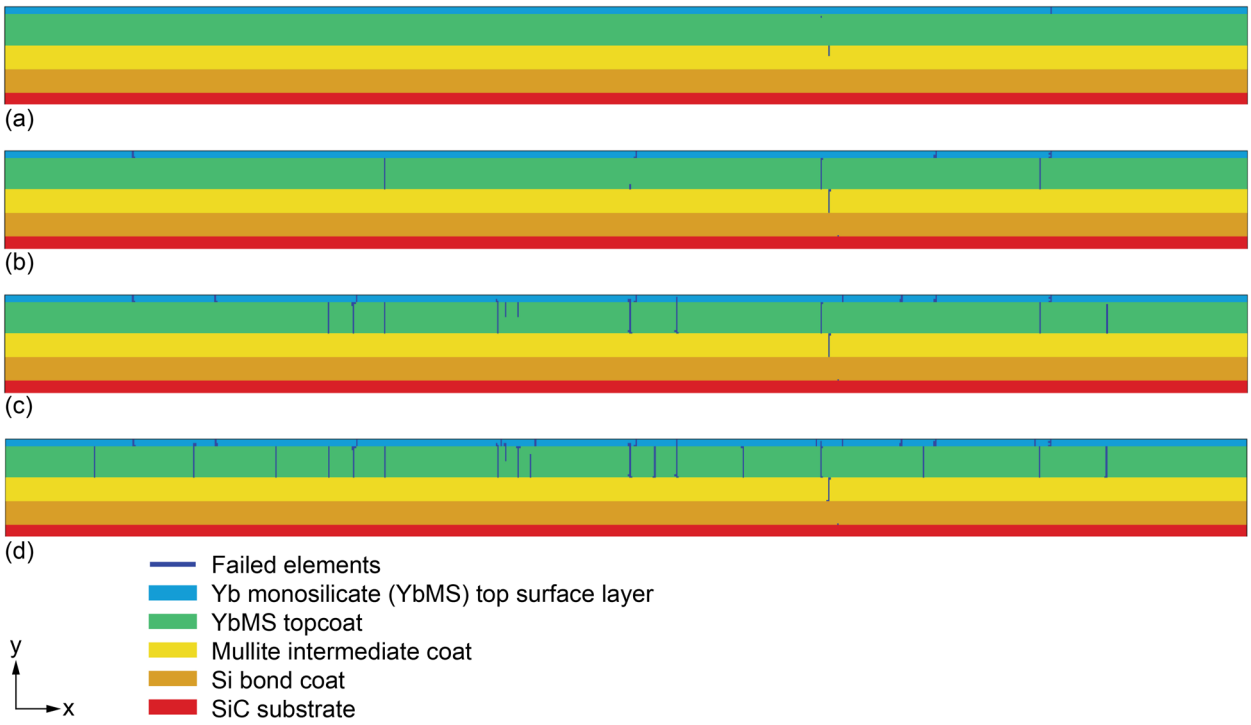

Figure 8.—Sequential snap shots of simulation of progressive crack damage development as the 2D model cools down from the initial anneal temperature of 1,300 °C down to 23 °C for Weibull modulus m_V = 2.5. Complete substrate is not shown. (a) At 905.8 °C. (b) At 611.5 °C. (c) At 317.3 °C. (d) At 23 °C.

the topcoat and the intermediate coat. There were some events of crack initiation and growth in the top surface layer, but they tended not to penetrate into the topcoat. The properties of the top surface layer and the topcoat only differed by the top surface layer having a somewhat smaller Weibull scale parameter σ_{0V} as indicated in Table I. Because of this, it would be expected that cracks would be more likely to initiate in the top surface layer than the topcoat, and once initiated, these cracks would propagate into the topcoat. However, this did not happen here. In the simulation the top surface layer was given only a marginally reduced Weibull scale parameter value of σ_{0V} = 40 MPa·mm$^{3/m}$ from the topcoat value of 56 MPa·mm$^{3/m}$, while m_V = 2.5 was kept the same for both regions (the top surface layer and the topcoat). In that case one would not expect to see a great difference in crack formation from the two regions of YbMS material. However, the fact that cracks that initiated in the top surface layer did not propagate into the topcoat is largely because the crack tip stress singularity is not explicitly modeled. Instead, at the root of the crack (tip) is an unfailed square-shaped element that experiences an elevated stress from a stress concentration, but not to the magnitude associated with a sharp crack (in the vicinity of the crack tip since a stress singularity exists at the crack tip). The behavior is more akin to a blunt notch rather than a sharp crack tip. Also, the Weibull scale parameter for the topcoat is higher than that for the top surface layer. This likely creates a resistance to crack propagation that could retard and even arrest crack growth. However, it can also be observed that mudcracks that initiate in the topcoat appear to arrest at the interface between the topcoat and the top surface layer. This was unexpected and should not have happened. For the simulations with the higher Weibull modulus values of m_V = 5.0 and 10.0, this appears to be much less or not an issue.

This problem appeared to be due to an anomalous stress discontinuity between the two layers and was not corrected during the preparation of this report. We considered it to be a somewhat minor, although annoying, issue that could be addressed at a later time. Figure 9 shows a closeup view of the σ_x normal stress (units of Pa) of the top surface layer and the topcoat at the center of the 2D FE model at 1,200 °C, prior to any damage. There appears to be a slight discontinuity (jog) in the stress distribution between the top surface layer and the topcoat. This discontinuity should not be present since the elastic properties of the two layers are identical. It is unclear how much this influenced the apparent crack growth arrest between the two layers shown in Figure 8. This barrier also appears to be present in Figure 10(a) toward the upper left (first crack on the left) and Figure 10(b) and in Figure 10(c) towards the top of the figures (indicated with arrows). This issue would require further investigation. The presence of the top surface layer was maintained in all models throughout this report.

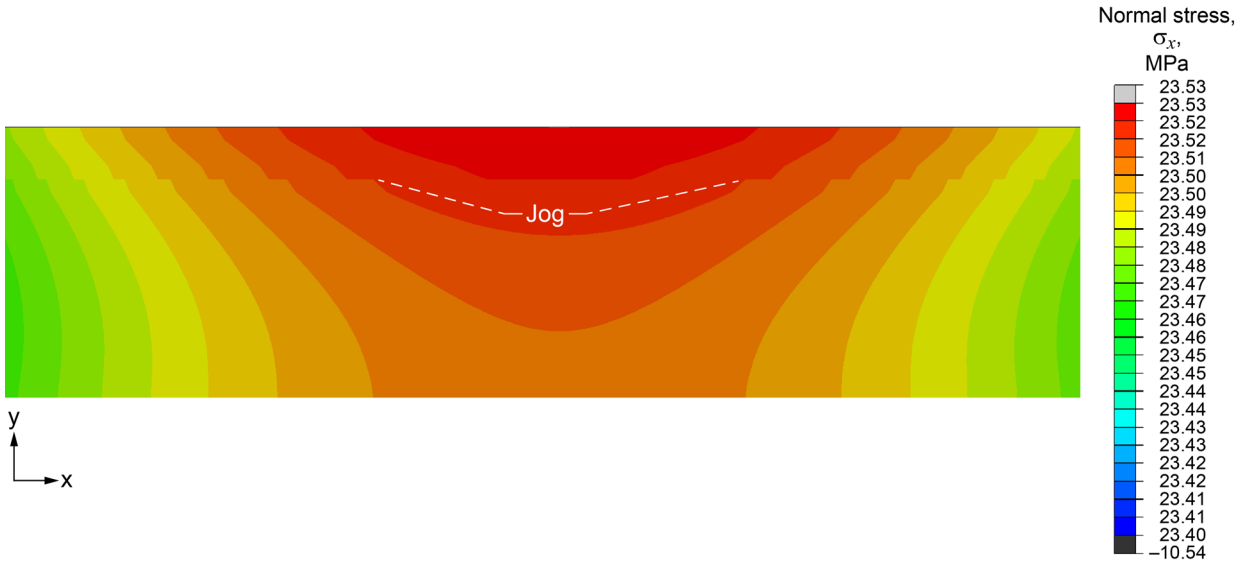

Figure 9.—Magnified plot of σ_x normal stress (units of Pa) of top surface layer and topcoat at center of 2D FE model at 1,200 °C, prior to any damage. A slight discontinuity (jog) in stress contour appears at interface between top surface layer and topcoat.

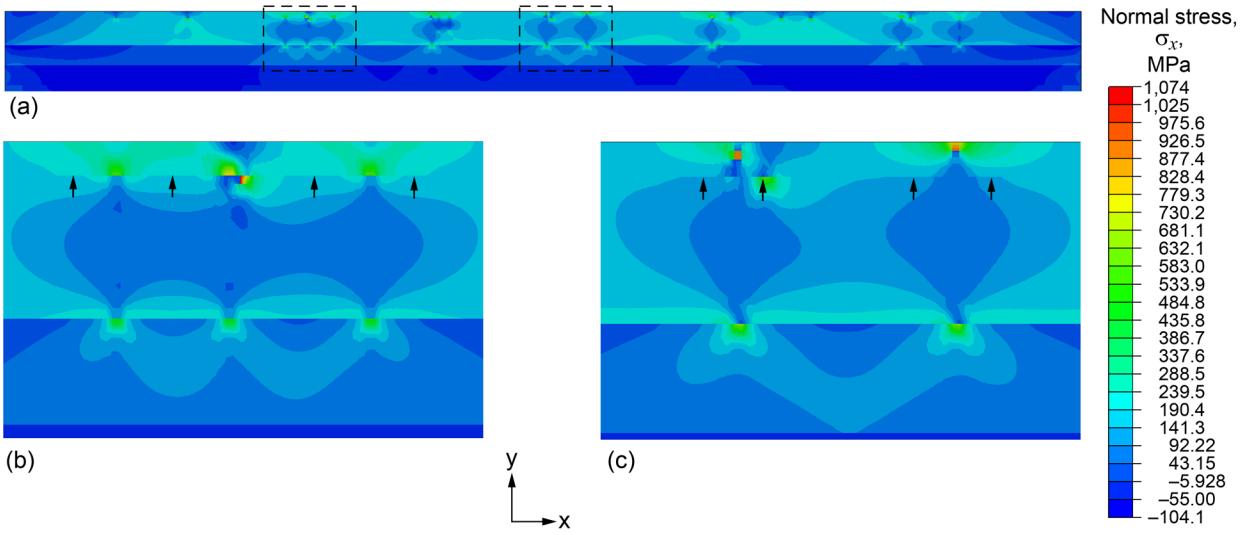

Figure 10.—Plot of σ_x normal stress profile at 317.3 °C for Weibull modulus m_V = 2.5. Arrows indicate stress discontinuity at boundary of top surface layer and topcoat (a). Stress plot of whole 4-mm-wide 2D finite-element (FE) model. (b) Closeup portion of FE model (towards left side). (c) Another closeup portion of FE model towards center. Complete substrate is not shown.

In Figure 8, at the center 3-mm span of the specimen (mudcracks within 0.5 mm of the unconstrained left and right edges were not counted because of edge effects on stress as shown in Figure 7(a)) there are approximately 14 mudcracks that span the topcoat layer for an average crack spacing of 210 µm. This is comparable to the average crack spacing, determined to be 240 µm in Figure 3. This only included mudcracks that spanned the whole topcoat and did not include the cracks that were in the top surface layer. Including those cracks that were in the top surface layer but were somewhat isolated from the mudcracks in the topcoat layer decreased the average crack spacing to about 140 µm.

Figure 10 shows a plot of the σ_x normal stress (units of Pa) profile at 317.3 °C, for m_V = 2.5, corresponding to the damage profile in Figure 8(c). Closer views are shown in Figure 10(b) and (c). As would be expected, stresses are relieved (reduced) around the mudcracks away from the crack tip region.

Figure 11 shows five sequential snap shots of the progressive crack damage development as the 2D model cools down from the initial annealing temperature of 1,300 °C down to 23 °C for

m_V = 5.0 (all other conditions and parameters were unchanged). Similar to Figure 8, the mudcracks tend to initiate on the top surface layer and topcoat, although they tend to start at a higher temperature than when m_V = 2.5. In Figure 11(a) there is only initial damage occurring in the topcoat near the interface between the topcoat and the intermediate coat. In Figure 11(b) there is more damage initiation and damage in the top surface layer that now appears to propagate into the topcoat, unlike in Figure 8. There appears to be resistance for cracks to penetrate from the topcoat into the intermediate coat as shown in Figure 11(b) to Figure 11(e). By the later increment shown in Figure 11(e), a fair portion of the mudcracks appear arrested at this interface. Ultimately, only a few cracks penetrate into the intermediate coat, and no mudcracks penetrate into the bond coat. In Figure 11(c) a delamination crack initiates in the bond coat (right side), and in Figure 11(d) a delamination (horizontal) crack initiates midway through the intermediate coat on the left-hand side, consistent with the location of the high σ_y stress seen in Figure 7(b) on the left and right unconstrained edges. Some horizontal delamination cracking can be seen to initiate at the interface between the topcoat and intermediate coat layers and fail in the topcoat elements (failed elements that jog to the left or right of a mudcrack). There is no element failure in the bond coat layer. The higher value of m_V = 5.0 results in the mudcracks initiating at a higher temperature than when m_V = 2.5 and more forming across the 4.0-mm span of the FE model. Also, events of crack initiation and growth in the top surface layer tends to penetrate into the topcoat layer, unlike the situation in Figure 8 when m_V = 2.5. Apparently the stress barrier previously discussed and associated with Figure 9 and Figure 10 is more easily breached with the higher value of Weibull modulus. The character of the mudcracks in Figure 11 is also different than in Figure 8. In Figure 8 the mudcracks typically consist of a single column of failed elements. In Figure 11 some of the mudcracks involved multiple columns of connected elements. Some mudcracks tend to group close together or appear related to the same main mudcrack event. Others seemed to be offset or "sheared" off. Perturbed stress fields from nearby damage could have affected

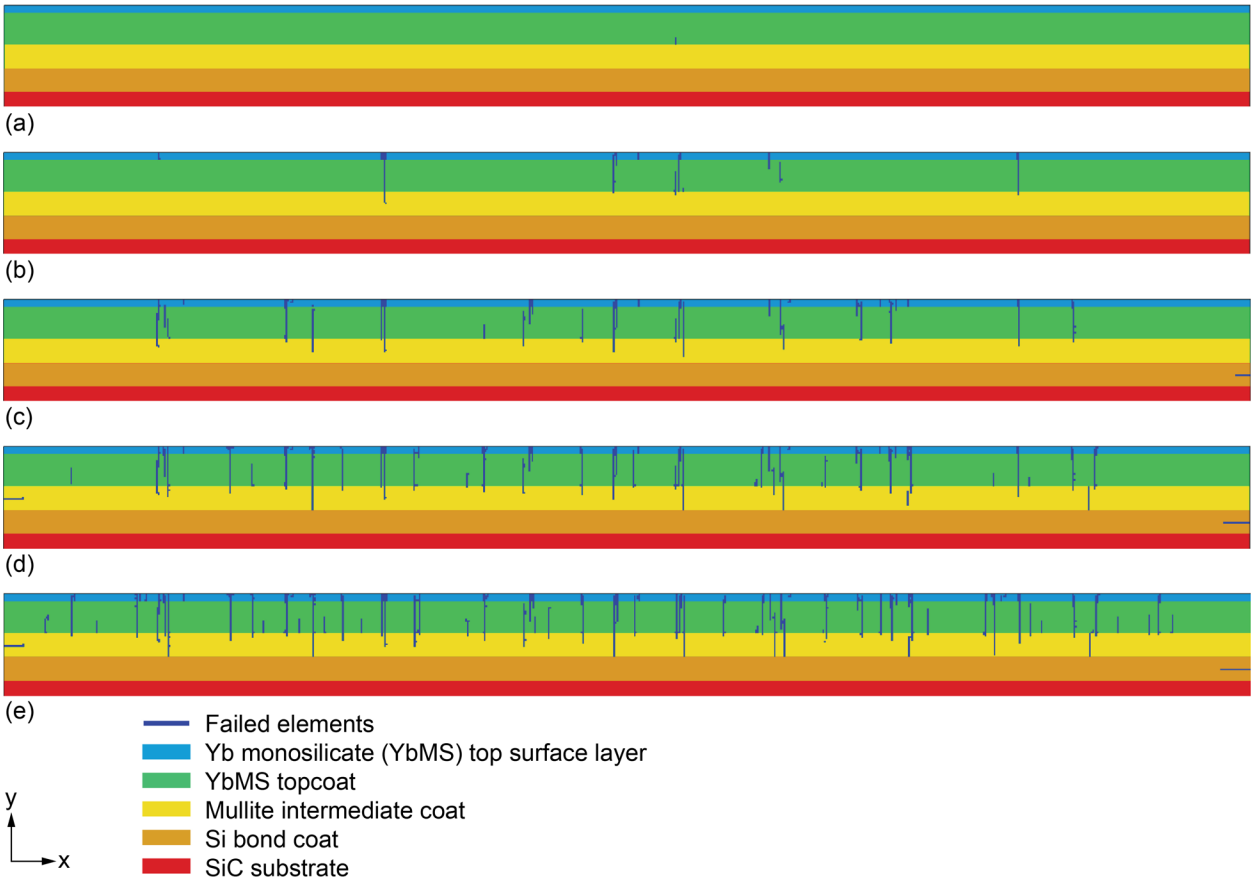

Figure 11.—Sequential snap shots of crack damage progressive development as 2D model cools down from initial annealing temperature of 1,300 °C down to 23 °C for Weibull modulus m_V = 5.0. Complete substrate is not shown. (a) At 1,053 °C. (b) At 905.8 °C. (c) At 611.5 °C. (d) At 317.3 °C. (e) At 23 °C.

this behavior. It is unclear if this behavior has any physical meaning (such as related to oblique cracking or crack bifurcation) or is solely anomalous behavior. (This is discussed more with the results of $m_V = 10.0$). Regardless, it is an outcome of the stochastic modeling. Approximately 28 mudcracks formed in the topcoat over a 3-mm center span (mudcracks within 0.5 mm of the unconstrained left and right edges were not counted because of edge effects on stress as shown in Figure 7(a)), for an average crack spacing of about 100 µm when the cooling was complete. This includes counting the occurrence of a group of very closely spaced or connected columns of failed elements as a single occurrence of a mudcrack. One instance of mudcracking that did not penetrate into the topcoat layer was discarded.

Figure 12 is a plot of the σ_x normal stress profile at 611.5 °C (corresponds with the cracking damage shown in Figure 11(c)). The figure indicates high values of σ_x normal stress in the topcoat layer located at the interface between the topcoat and the intermediate coat. This would imply a shifted damage initiation site that can be seen in some of the cracking damage development in Figure 11(d) and Figure 11(e). The stress profile shown in Figure 12 can be compared to the undamaged σ_x normal stress profile shown in Figure 7(a). The mudcracks that initiate in the top surface coat and topcoat results in stress relief on the exposed surface (the surface exposed to the ambient environment), which increased the σ_x normal stress in the topcoat at the interface between the topcoat and the intermediate coat.

Figure 13 shows five sequential snap shots of the progressive crack damage development as the 2D model cools down from the initial temperature of 1,300 °C down to 23 °C for m_V = 10.0. Mudcracks tend to initiate at a higher temperature than when $m_V = 5.0$. Also, as previously stated for the simulations when $m_V = 5.0$, events of crack initiation and growth in the top surface layer tend to penetrate into the topcoat, unlike the situation in Figure 8 when $m_V = 2.5$. Apparently the stress barrier previously discussed and associated with Figure 9 and Figure 10 is more easily breached with the higher value of Weibull modulus. However, in this case (Figure 13(b)) the character of the mudcracking is different from those shown in Figure 11(c) and Figure 8(d) in the manner that the mudcracks may also involve (failed) adjacent elements near the root of the crack or along the side wall to the original mudcrack as cooling progressed. Continuation of this behavior reduces by Figure 13(c). Also, some of this early damage appears to meander or shift left or right as damage progresses through the coating layers (at a slightly oblique angle). In Figure 13(c) to (e) mudcracks tend to initiate in the topcoat at or near the interface between the topcoat and intermediate coat. The newly developed mudcracks then have a more linear appearance mostly composed of single columns of failed elements, more similar to that seen in Figure 8 and Figure 11. Damage development in Figure 13(d) and Figure 13(e) show that a delamination between the topcoat and the intermediate coat has begun to form, where the elements in the topcoat fail at this material boundary (results from other simulations, not presented here, with more exaggerated loading conditions clearly showed complete delamination). Horizontal delamination cracks can be seen to form at the left and right unconstrained boundaries in Figure 13(e) in the intermediate coat at the interface between the intermediate coat and the bond coat—again consistent with the high σ_y stress seen in Figure 7(b) on the left and right unconstrained edges.

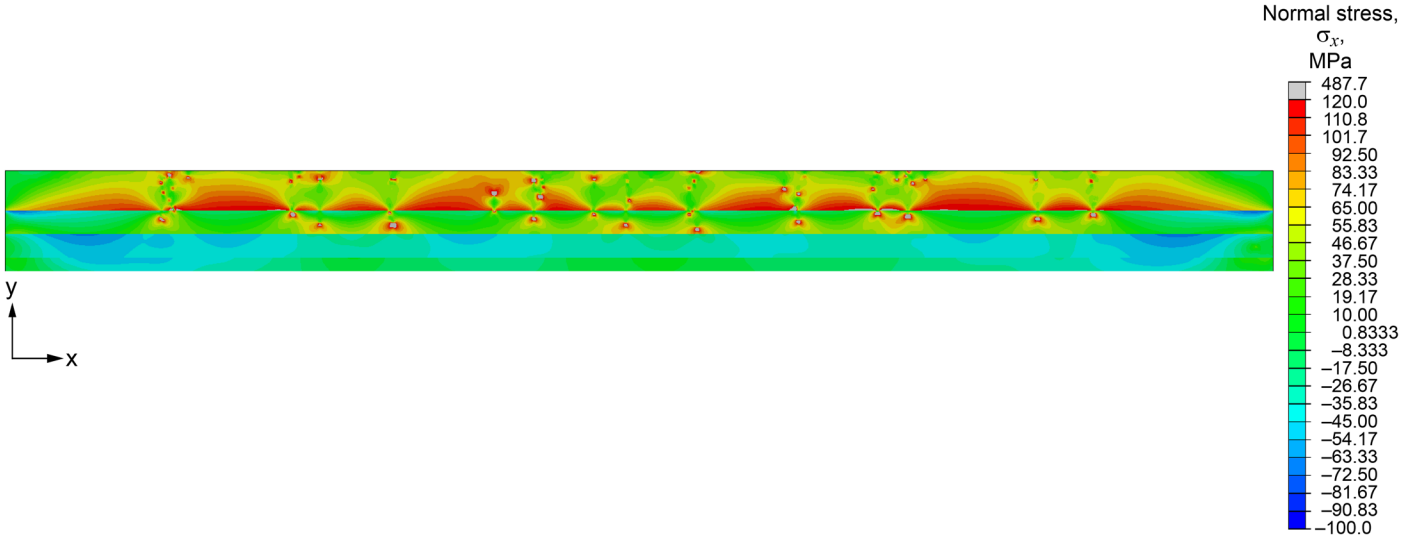

Figure 12.—σ_x normal stress profile at 611.5 °C.

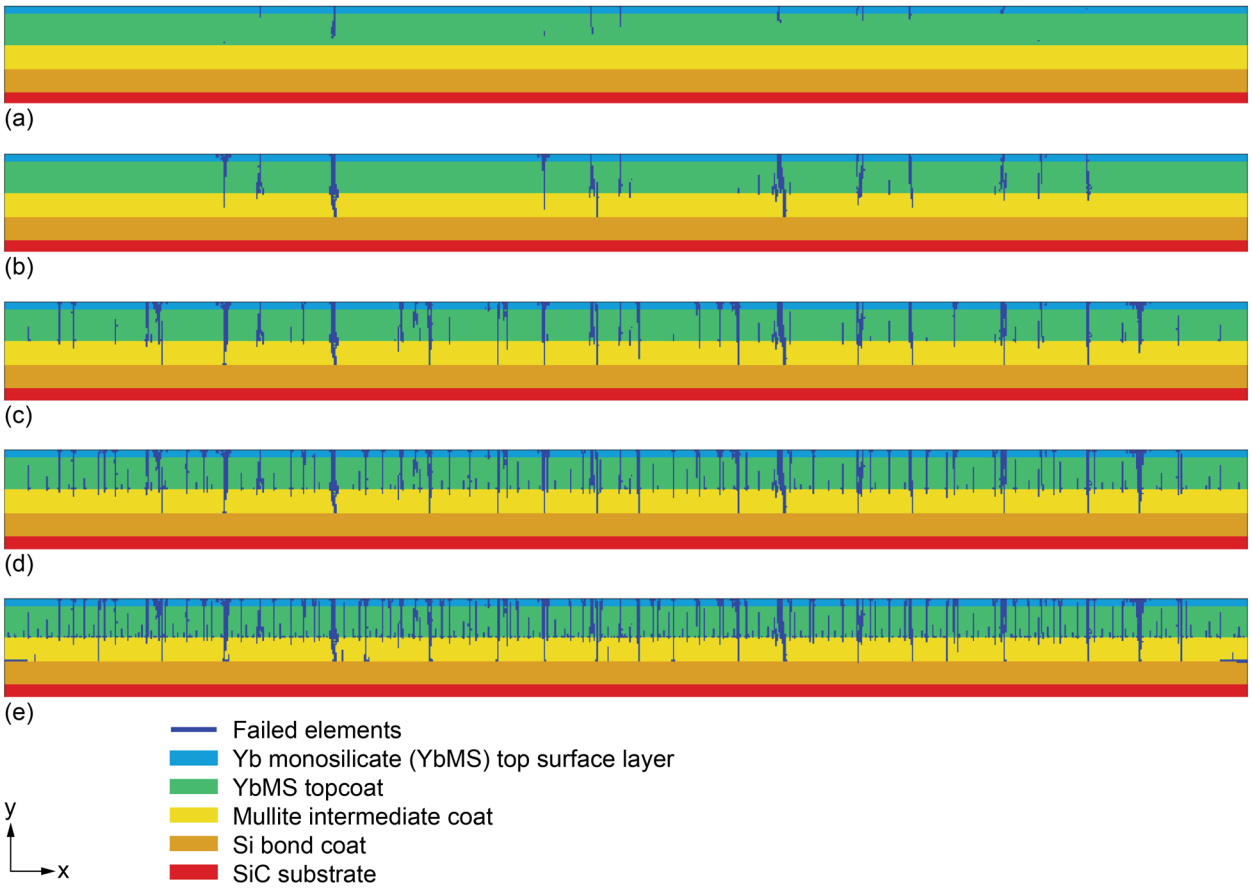

Figure 13.—Sequential snap shots of crack damage progressive development as the 2D model cools down from the initial anneal temperature of 1,300 °C down to 23 °C for Weibull modulus m_V = 10.0. Complete substrate is not shown. (a) At 1,053 °C. (b) At 905.8 °C. (c) At 611.5 °C. (d) At 317.3 °C. (e) At 23 °C.

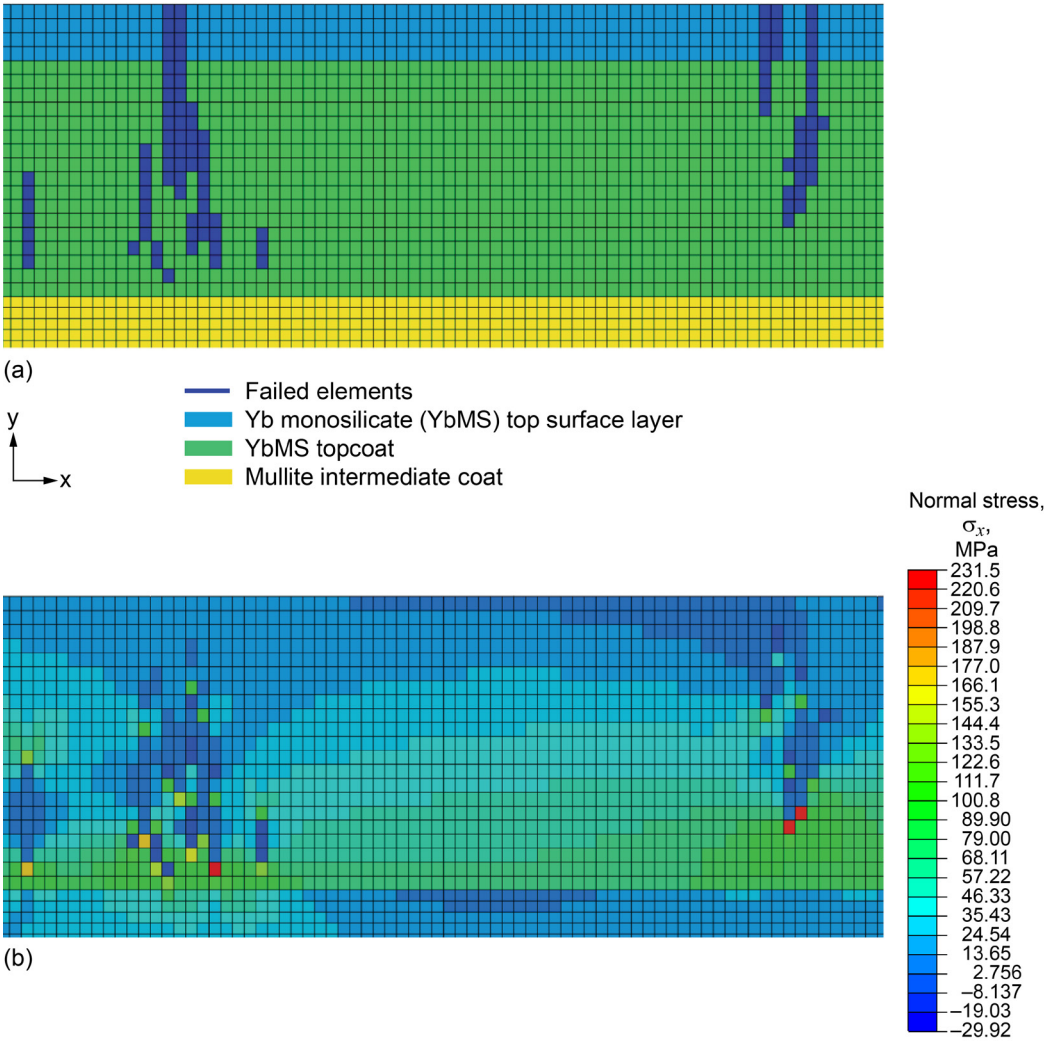

Figure 14.—Closeup view of 2D model at 1,021 °C, for m_V = 10.0. (a) Failed elements. (b) σ_x normal stress.

Figure 14 shows a closeup of the damage and stress profile at 1,021 °C for two mudcracks. Figure 15 shows a closeup of the damage and stress profile at 1,044 °C for a single mudcrack. These figures show a more complex and possibly bifurcated element failure damage evolution than previously for the smaller values of m_V = 2.5 and 5.0 that are shown in Figure 8 and Figure 11, respectively. Figure 14(b) and Figure 15(b) show elements with high stresses located in the vicinity of the developed damage front. Figure 16 shows a closeup of damage, possibly involving splitting or formation of attached ligaments of unfailed elements. Figure 14(b) and Figure 15(b) show the σ_x normal stress profile of the damage. The σ_y and the τ_{xy} stress components were considerably lower in values and are not shown. For the higher value of m_V = 10.0, element failure appears to be more sensitive to local stress fluctuations that occur around developing damage. This may be a contributing cause to the more complex failure behavior observed here.

Figure 17 is a plot of the σ_x normal stress profile at 905.8 °C (resulting from the cracking damage in Figure 13(b)). The figure indicates high values of σ_x normal stress in the topcoat at the interface between the topcoat and the intermediate coat. The mudcrack damage that occurred previous to this load increment relieved the stresses in the top surface layer and the upper portion of the topcoat (compare to the σ_x normal stress distribution shown in the top surface layer and the topcoat, depicted in Figure 7(a)). This would imply a damage initiation site shifting as evidenced by the cracking damage development in Figure 13(c), Figure 13(d), and Figure 13(e).

What could be interpreted as a “spallation” event, consisting of a connected path of failed elements that terminate at the surface, is seen in Figure 13(e) towards the left-hand side of the figure. A closeup of this region is shown in Figure 18. In Figure 13(e) approximately 57 mudcracks were counted in the topcoat over the length of a 3-mm span about the specimen

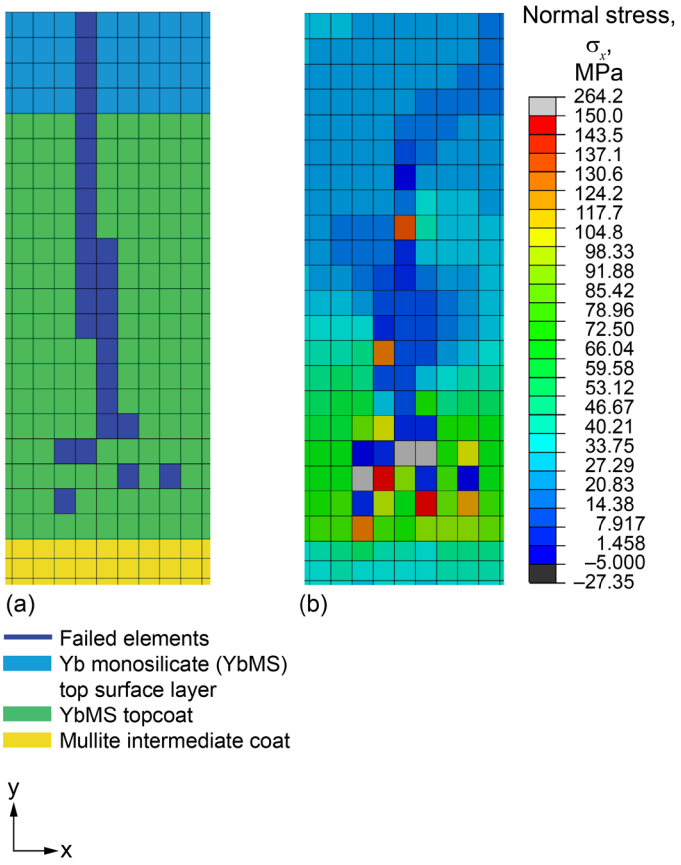

Figure 15.—Closeup view of 2D model at 1,044 °C. (a) Failed elements. (b) σ_x normal stress.

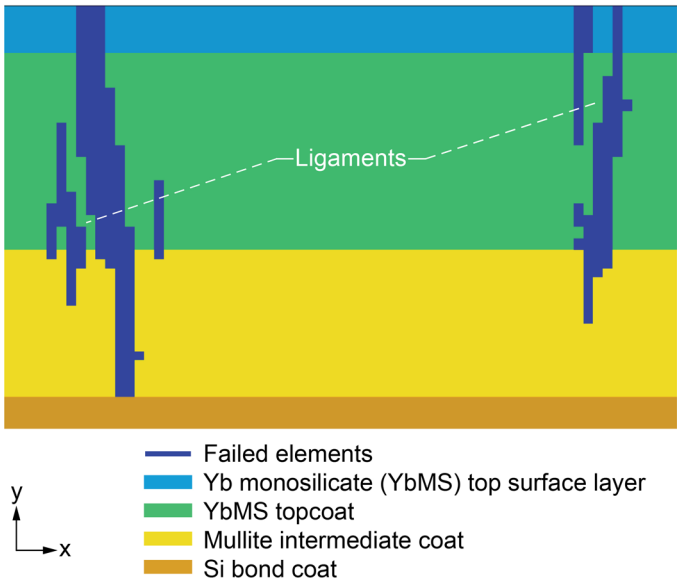

Figure 16.—Closeup view of failed elements at 852.8 °C, indicating possible formation of ligaments of unfailed elements. Gridlines have been turned off in figure.

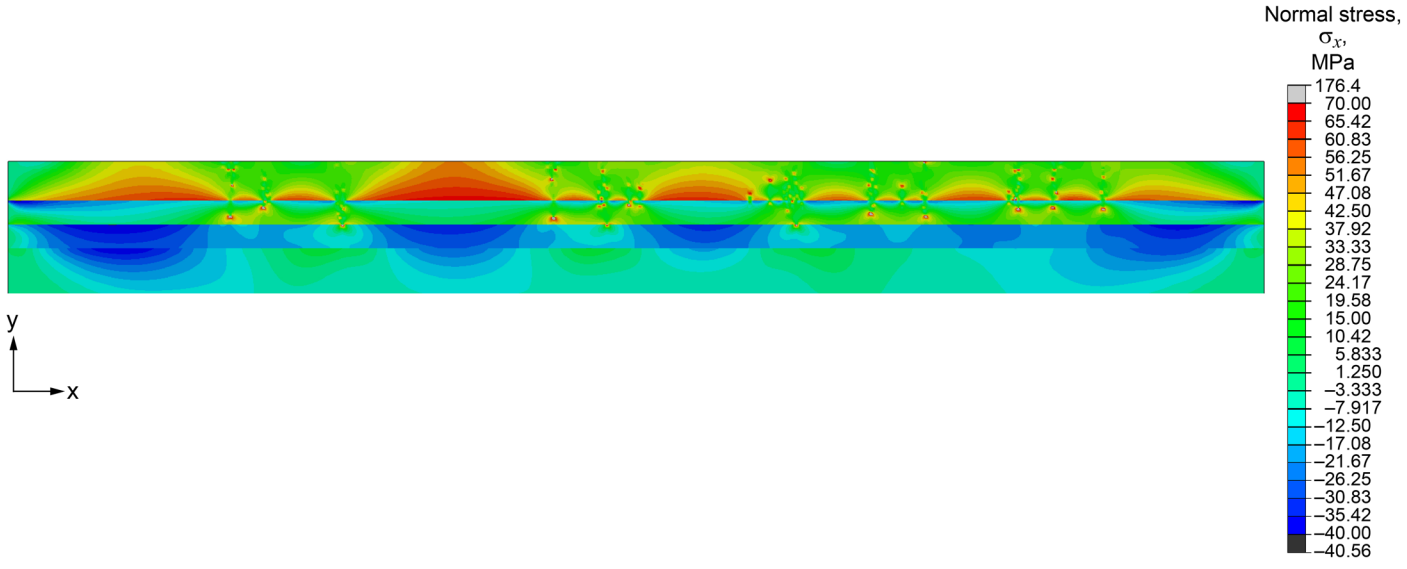

Figure 17.—σ_x normal stress profile at 905.8 °C.

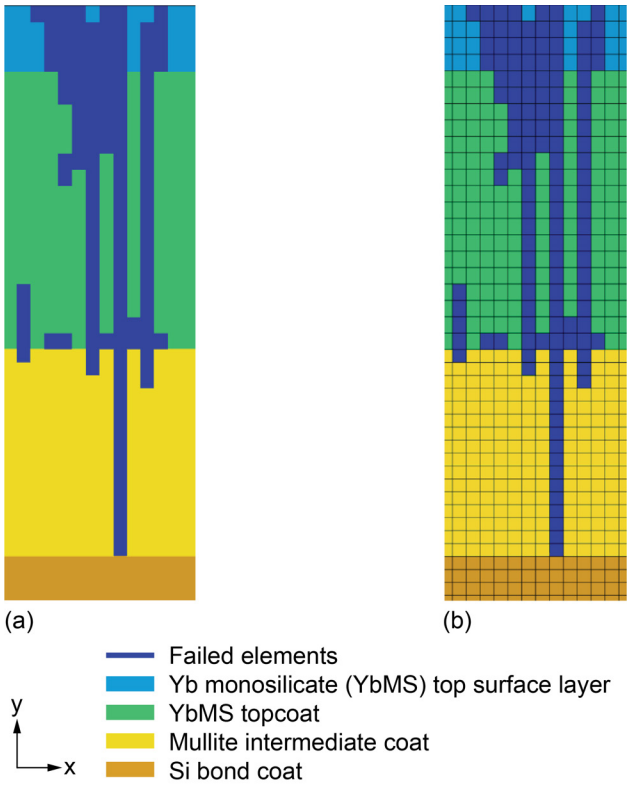

Figure 18.—Possible spallation event consisting of path of connected failed elements to exposed surface. Closeup of a region in Figure 13(e) damage at 23 °C, towards left-hand side of figure. (a) Shown with the mesh gridlines turned off. (b) Showing the mesh gridlines.

midpoint (mudcracks within 0.5 mm of the unconstrained left and right edges were not counted because of edge effects on stress as shown in Figure 7(a)), for an average crack spacing of about 53 μm.

As described in this section, FEAMAC/CARES was able to mimic the formation and growth of crack-like damage events from cooldown. This was demonstrated on a 2D FE model of a 4.0- by 1.0-mm cross section of a three-layer EBC deposited on a SiC substrate (the FE model is shown in Figure 6). The FE model was assumed to have had an initial annealing temperature of 1,300 °C and was subsequently cooled to room temperature. The cooldown elicited the buildup of large residual stresses within the coating layers (see Figure 7), which caused the spontaneous initiation of mudcracking (see Figure 8, Figure 11, and Figure 13). The FE model of the multilayered EBC with substrate was modeled with a sufficient mesh density such that mudcracks were able to be individually resolved. The simulations that were performed resulted in the formation of mudcracks with an overall periodic crack spacing. The effect of three different values of Weibull modulus m_V = 2.5, 5.0, and 10.0 on the character of damage development was investigated. The crack segmentation length (or conversely the crack density) was dependent on the value of m_V when the Weibull scale parameter σ_{0V} and all other parameters were held constant. This crack density increased as the value of m_V increased. Other failure modes could also be reproduced, such as the beginning of edge cracking delamination in Figure 11 and Figure 13 and the development of layer delamination of the topcoat layer from the intermediate coat shown in Figure 13(e). The effect of the development of mudcracks on the top surface layer and the topcoat was to relieve stress nearer to the coating-exposed surface and redistribute these stresses towards the boundary between the topcoat and intermediate coat, localized in the topcoat material, as shown in Figure 12 and Figure 17. A potential spallation event was shown in Figure 18. The FEAMAC/CARES methodology as employed here was highly mesh dependent: crack propagation was primarily perpendicular to the surface or parallel to it. Crack propagation at an oblique angle to the surface was not as clearly evident although it is frequently observed in experiments with EBCs.

6.0 3D Finite Element Model of Disk With EBC and Substrate

A FE model was made for an EBC-coated disk having overall dimensions of 10 mm in diameter by 1 mm thick so that mudcrack formation over the surface area of the EBC could be simulated with FEAMAC/CARES. This specimen geometry was not tested by Richards et al. (2015, 2016). The disk FE model is shown in Figure 19. Individual layer thicknesses and material properties are the same as those shown in Figure 2 and Table I, respectively. The disk shape is investigated instead of the rectangular shape specimen geometry used by Richards et al. so that any effects of the rectangle's four sharp corners on the stress (and subsequent damage) distribution about the outside periphery (perimeter) of the model did not have to be considered. Unfortunately, as previously stated, no overhead view of the EBC surface showing the surface cracking network of the mudcracks (the mudflat) is available. The overall disk dimensions were arbitrarily chosen by the authors for the current study. The FE model consisted of 266,310 C3D8R 3D continuum reduced integration elements. In Figure 19, the top surface layer is the first layer of elements on the exposed surface of the model, and the rest of the topcoat is the next two layers of elements. The intermediate coat is the adjoining two layers of elements, and the bond coat comprises the next two layers of elements through the thickness, followed by the remaining layers of elements of the substrate. Figure 19(a) shows the disk without the mesh lines. Figure 19(b) shows a closeup of the edge of the disk highlighting the coating layers. Figure 19(c) shows representative details of the mesh layout (the whole element mesh of the disk is not shown because of the difficulty of viewing the closely spaced mesh

gridlines). The damage patterns that are subsequently shown are influenced by the mesh. The coating truncates at the edge of the disk rather than extending over the edge. This assumes the EBC was either not applied to the edge of the disk or it was removed by polishing, machining, or grinding. The "top surface layer" consists of the same material as the topcoat material (same as was done with the 2D cross-sectional model in Figure 6). The bottom of the disk is constrained in the z-direction (through the thickness) to prevent warpage. This was done so that the substrate would act in a more rigid manner and mimic the behavior of a thicker substrate. This constraint enables using fewer elements to model the action than a thicker substrate would have. There are fewer layers of elements through the thickness (the z-direction) than the 2D cross-section model (Figure 6). Reducing the element count and using the C3D8R reduced integration element type helped reduce the amount of memory and computation time needed to run a simulation.

Figure 20 and Figure 21 show the stress profile of the disk FE model prior to any damage for a 10 °C incremental cooldown from an initial temperature of 1,300 to 1,290 °C for various in-plane stress components. Figure 20 shows the top surface of the disk. Here, the x- and y-axes are in the plane of the paper and the z-direction is through the thickness. Comparing Figure 20(a) for σ_x and Figure 20(b) for σ_y with Figure 20(d) for von Mises stress it is clear that the stress state on the top surface of the coating is an equibiaxial tensile stress. This situation occurs approximately 1.2 mm from the disk edge and towards the disk center. At the edge of the disk there is a uniform uniaxial tensile stress oriented perpendicular to the edge and going around the perimeter of the disk.

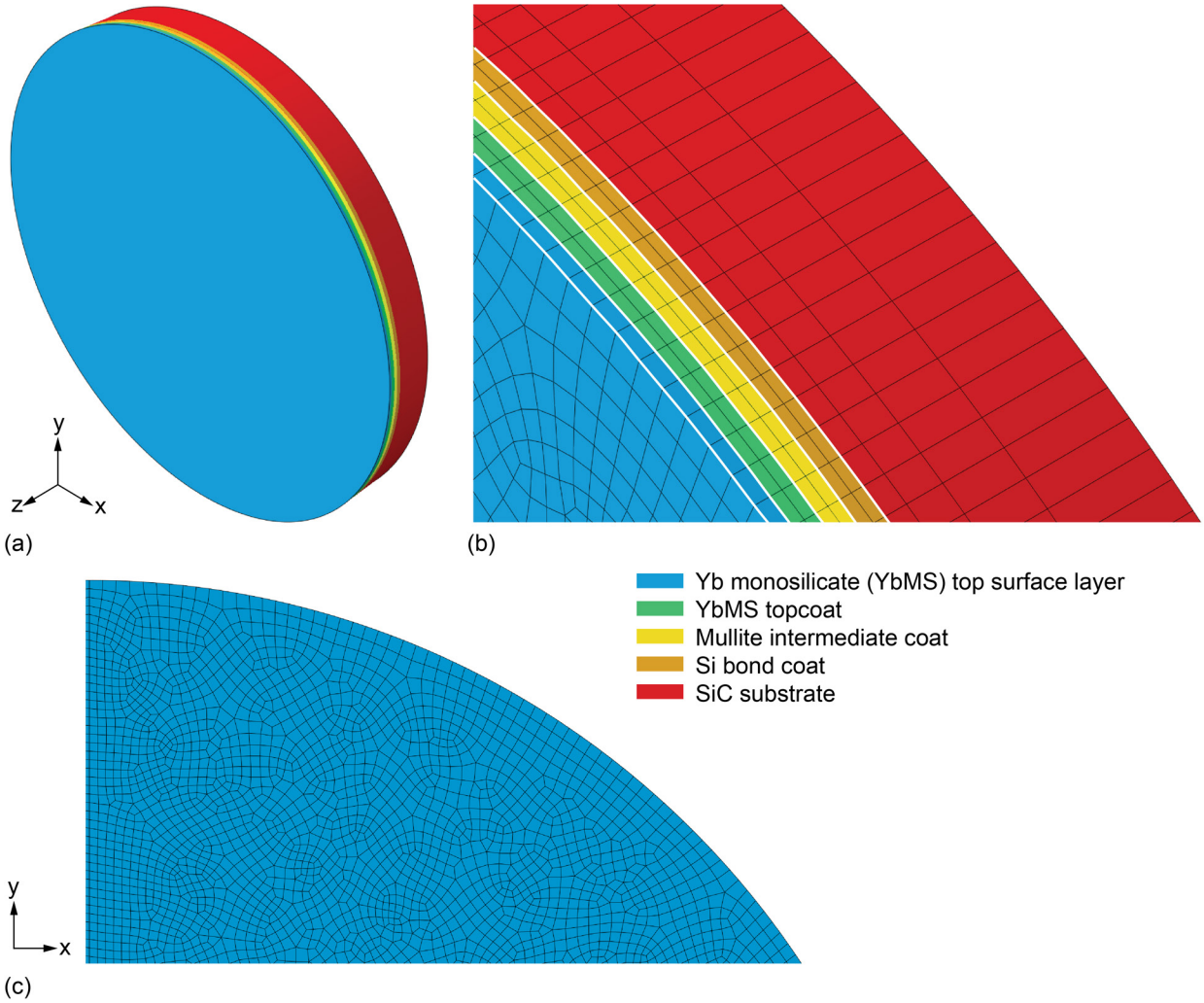

Figure 19.—3D FE model of 10-mm-diameter by 1-mm-thick disk of EBC material and substrate. (a) Whole model, without mesh lines shown. (b) Closeup of edge. White lines added to contrast material borders. (c) Portion of the top surface element mesh. x- and y-directions are in the plane of disk surface, and z-direction is through the thickness. Bottom of disk substrate was constrained in z-direction.

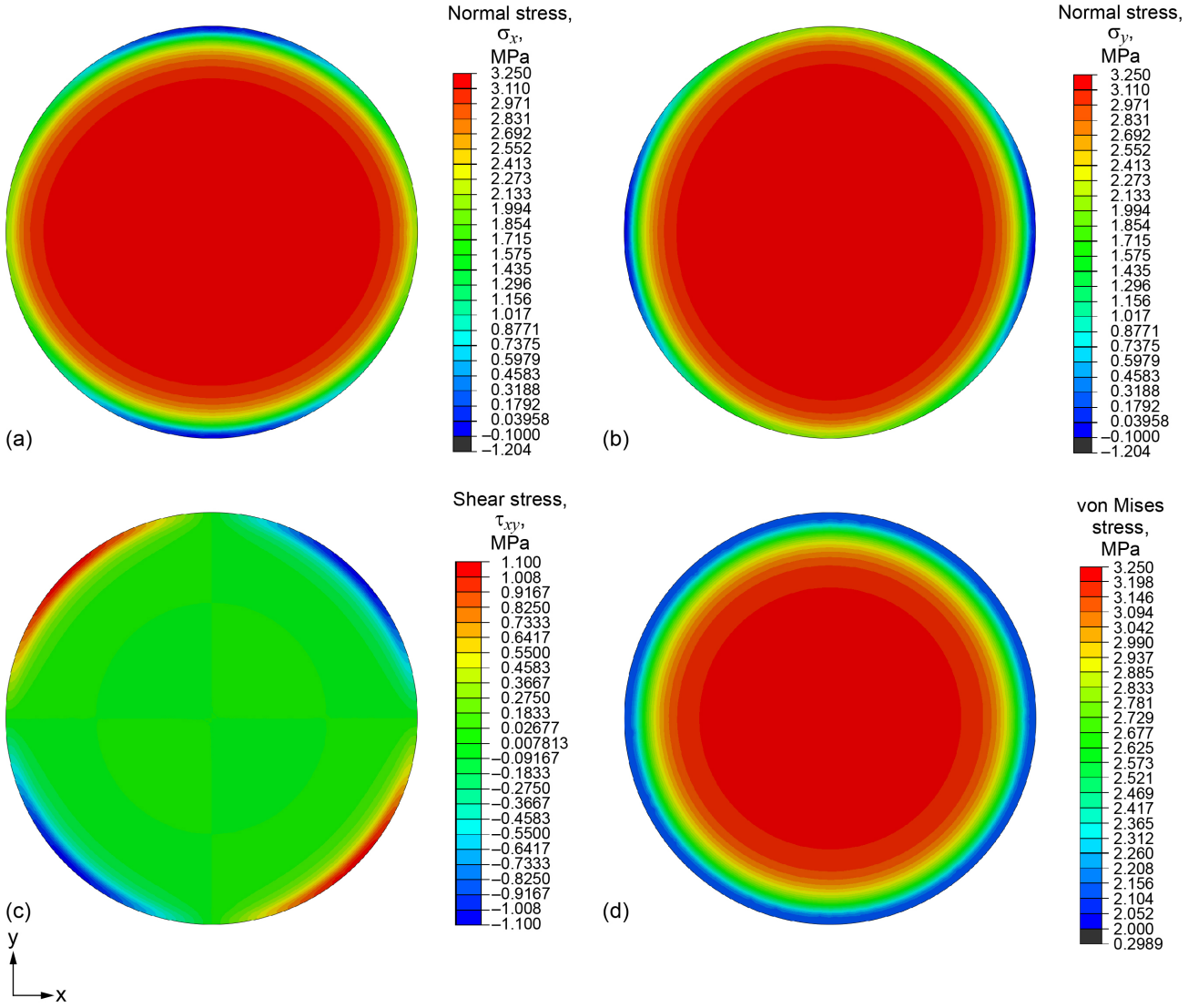

Figure 20.—Stress profiles on disk of top surface layer of EBC for 10 °C incremental cooldown from 1,300 to 1,290 °C for various stress components. z-direction is through the thickness. Plots shown without gridlines. (a) σ_x stress component. (b) σ_y stress component. (c) τ_{xy} shear stress component. (d) von Mises stress.

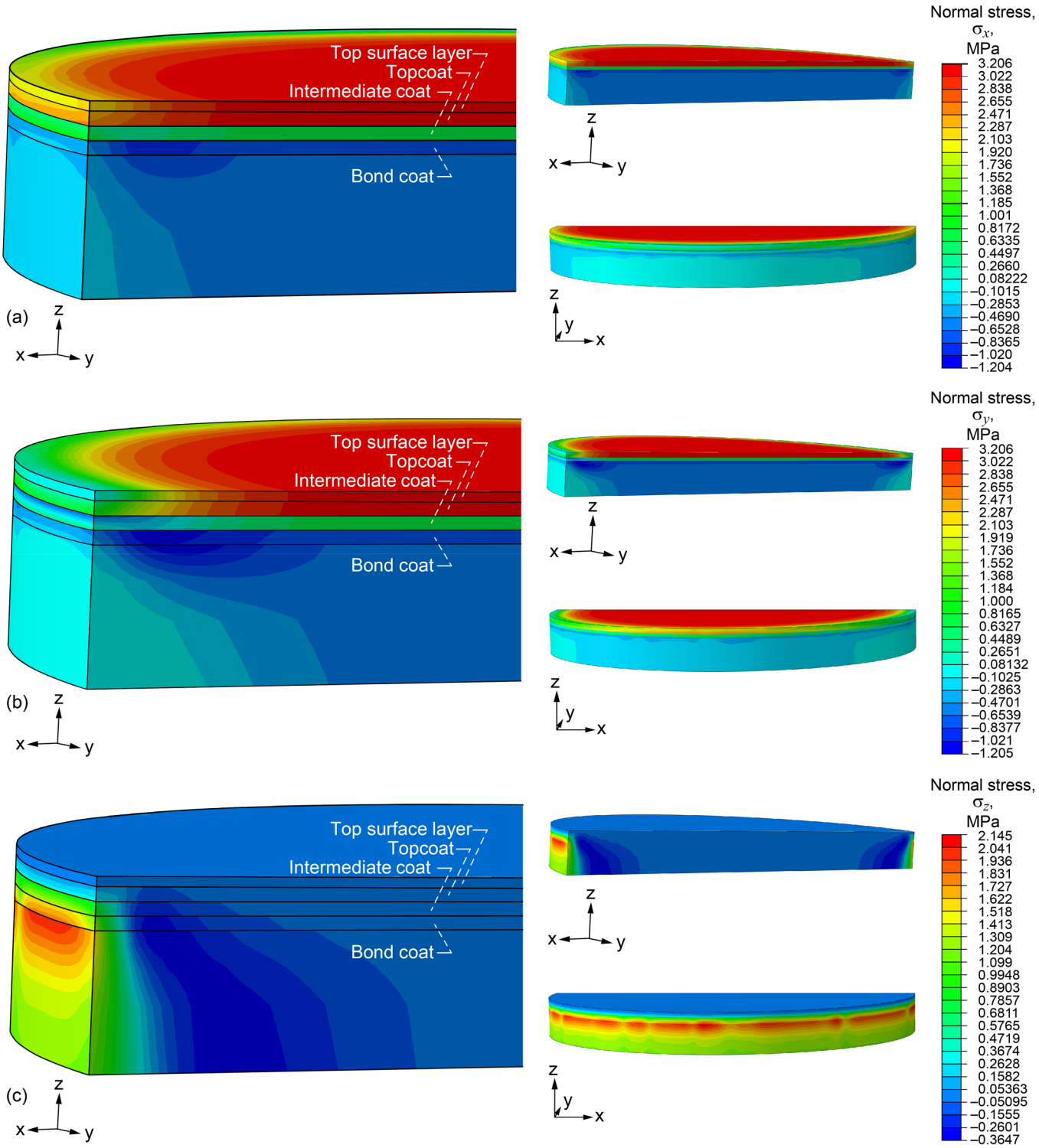

Figure 21.—Stress profile for various stress components through a center-cut cross section of disk for 10 °C incremental cooldown from 1,300 to 1,290 °C. The z-direction is through the thickness. Plots shown without gridlines. (a) σ_x stress component. (b) σ_y stress component. (c) σ_z stress component. (d) τ_{xy} shear stress component. (e) τ_{yz} shear stress component. (f) τ_{zx} shear stress component. (g) von Mises stress component.

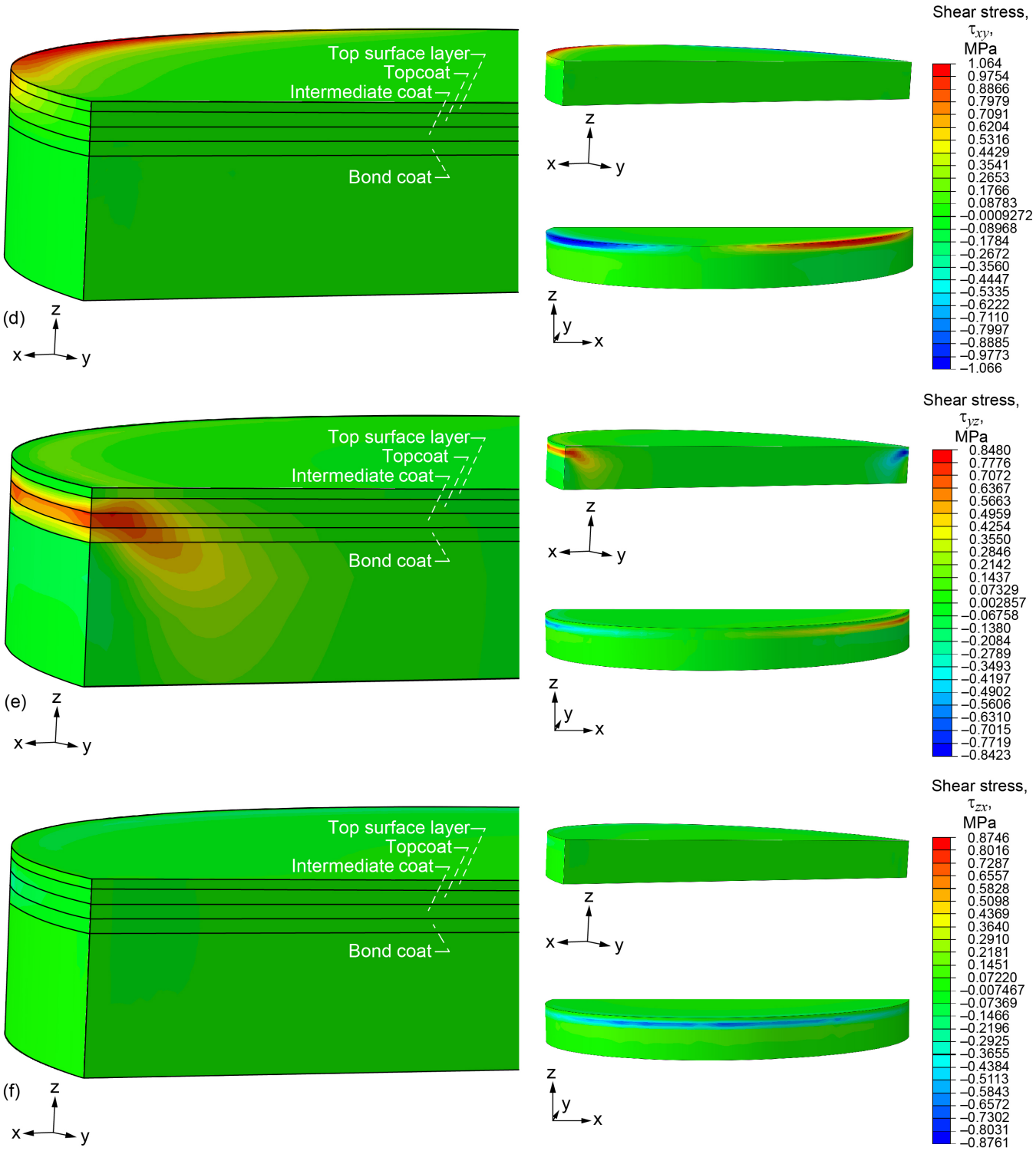

Figure 21.—Continued.

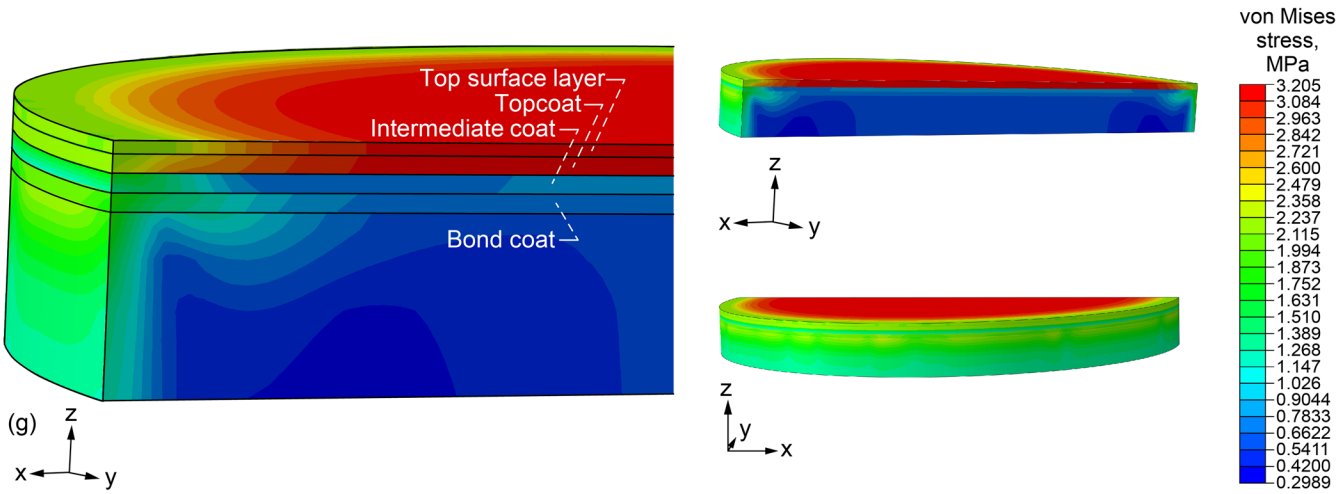

Figure 21.—Concluded.

Figure 21 shows the stress profile for various stress components of a center-cut cross section of the disk for a 10 °C cooldown from 1,300 to 1,290 °C. The z-direction is through the thickness. Figure 21(c) shows the σ_z stress component distribution. There is significant nonuniformity in the magnitude of this stress component about the disk circumference at the interface between the bond coat and the SiC substrate. The cause of this non-uniformity was not established. It would require further investigation but may be related to lack of mesh refinement at this interface and the abrupt transition of the Young's modulus E between the bond coat and the substrate (see Table I). Also, it is unclear if a stress discontinuity between the top surface layer and the topcoat is present in Figure 21 of similar nature to that shown in Figure 9. This uncertainty is partly because the top surface layer of the disk is spanned by only a single C3D8R-type reduced integration element (whereas four elements span the top surface layer of the 2D FE model, as shown in Figure 6). The trends in the stress distributions in Figure 21 are comparable to those of Figure 7, although Figure 7, Figure 20, and Figure 21 each display results for different cooldown temperatures.

As was done for the 2D cross-sectional model of the EBC and substrate system, FEAMAC/CARES is applied to simulate progressive damage in the 3D disk FE model of the EBC coating layers and substrate using the thermomechanical properties listed in Table I for the three different values of Weibull modulus m_V of 2.5, 5.0, and 10.0. Here the formation of mudcrack damage is investigated. In addition, the mudcrack segmentation length is examined around the periphery of the disk. Each simulation is broken down into 410 incremental temperature load increments: the first 10 equally spaced increments, cooling from 1,300 to 1,200 °C (a range where minimal damage typically occurred) as a uniformly decreasing ramp load and the next 400 equally spaced temperature increments as a uniformly decreasing ramp load, cooling from 1,200 to 23 °C. No thermal gradient was assumed to be present. The 410 temperature increments were the largest number of solution steps practicable within memory and solution time constraints. Having a large number of temperature increments allowed damage to better equilibrate by reducing the amount of potential damage accumulation with each temperature increment. A FEAMAC/CARES simulation of this model typically took over 2 weeks to run on one CPU of a personal computer.

In the 3D EBC stochastic progressive damage simulation, there was a spontaneous development of mudcracks that would coalesce into complete network of mudcracks. As the cooling progressed, the mudcracks would continue to fragment into progressively smaller sizes. Figure 22 shows an example of a simulated damage pattern that developed on the exposed surface of the disk for $m_V = 5.0$. Failed elements are shown, and the display of element mesh grid lines have been turned off (because of the high mesh density). Early damage development is shown in Figure 22(a), and development of damage is shown in Figure 22(b) to (f) as it sequentially progresses. Figure 22(a) shows that early damage is diffuse: randomly distributed and located away from the disk edge. Early damage tends to initiate away from the periphery because the magnitude of the in-plane stress away from the periphery was higher than it was towards

the edge (see Figure 20(d)). The damage represents discrete mudcrack events and takes on a filamentary appearance of randomly distributed strings of connected elements (incomplete mudcracks). This behavior was encouraged by the cellular automaton technique that was employed. Damage initiated at multiple locations about the disk within a short range of cooling. The simulation shows stable crack growth as cooling proceeded. This seems reasonable because the substrate constrained and controlled the development and growth of the mudcracks. Failure initiated in random elements according to the Weibull-related criterion described in Section 3.0, "FEAMAC/CARES." A closer look at the mudcracking damage that forms along the disk edge is shown in Figure 23. There, the mudcracks are primarily oriented perpendicular to the disk edge. This is a result of the stress state along the disk edge being uniaxial—tensile in a direction perpendicular to the disk edge—and cracks tend to grow perpendicular to the direction of maximum stress. Away from the edge, the path of failed elements ran in more random directions because of the development of the equibiaxial stress state. The pattern of cracking also exhibits a mesh dependency, whereby the path of the failed elements follow the layout of the mesh. This can be seen in Figure 24, which is a closeup of the damage away from the disk edge. Towards the center of the figure the mesh pattern shows a more ordered grid-like appearance (as a network of lines that cross each other to form a series of squares or rectangles). In that region the mudcracks also take on a more square or rectangular shape. This mesh dependency may be reduced by various means, but that was not attempted for this report. Mostly the mesh of the disk has a somewhat irregular appearance (see Figure 19(c)) rather than a regular defined grid work arrangement of elements, and because of this the cracking pattern itself also has a somewhat irregular appearance to it.

The progressive development of the mudcracking in Figure 22 is indicated by filaments of connected failed elements that eventually connect and segregate into closed cells (mudflat). As the cooling proceeds, the individual crack filaments intersect and stop growing while new filaments of cracking form. This further segments existing cells into smaller groups of cells. Eventually, a dense network of cracks forms, consisting of closed regions of undamaged elements surrounded by boundaries of failed elements. This increasing fragmentation into smaller closed cells of undamaged elements as cooling proceeds, develops in a manner consistent with a fractal type of fracture pattern. This cracking is mostly confined in the top surface layer of the top layer of coating but can penetrate to the intermediate coating layer as can be seen in Figure 23. In nature, mudflat crack shapes can vary between quadrilateral (rectangular) to other polygonal shapes (e.g., Figure 1(a) and Figure 1(b)).

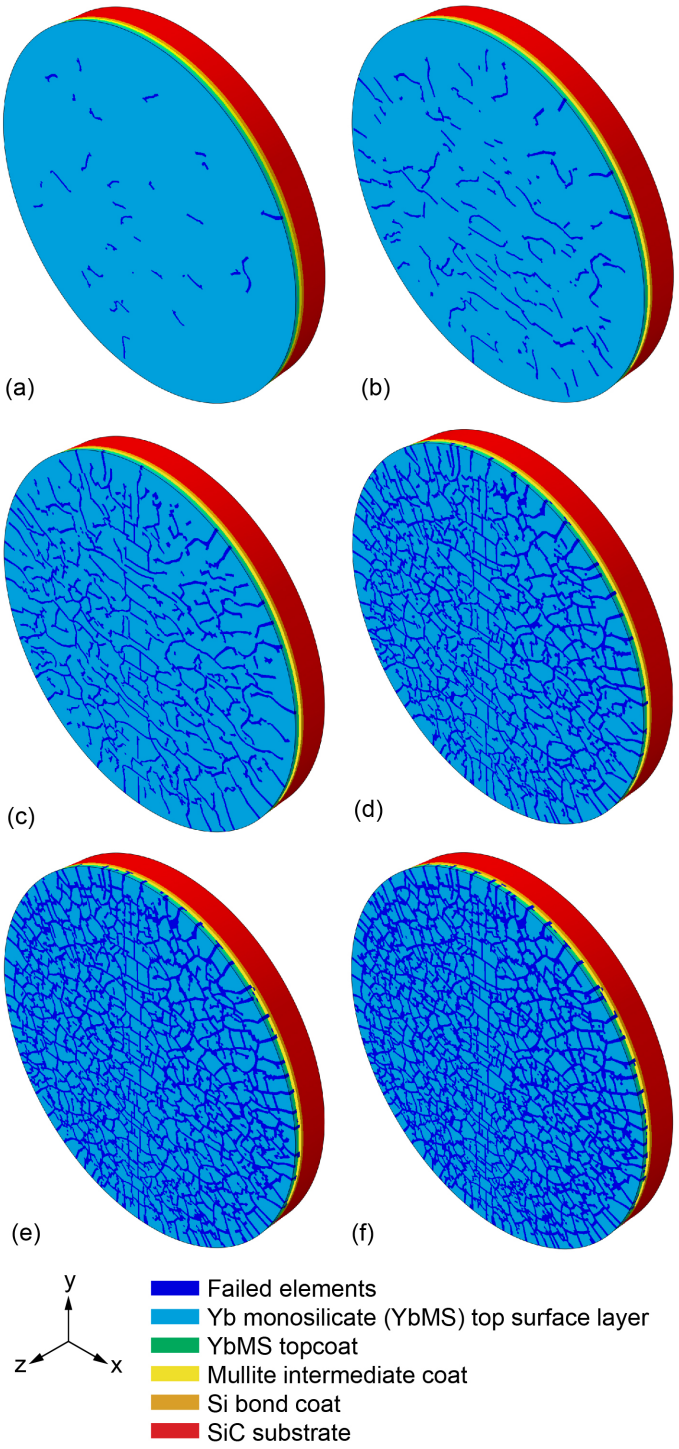

Figure 22.—Example of damage development on cooling disk of EBC on SiC substrate for Weibull modulus m_V = 5.0 for coating layers. Shown are individual layers in EBC system and corresponding failed elements. (a) At 1,126 °C. (b) At 1,053 °C. (c) At 905.8 °C. (d) At 611.5 °C. (e) At 317.3 °C. (f) At 23 °C.

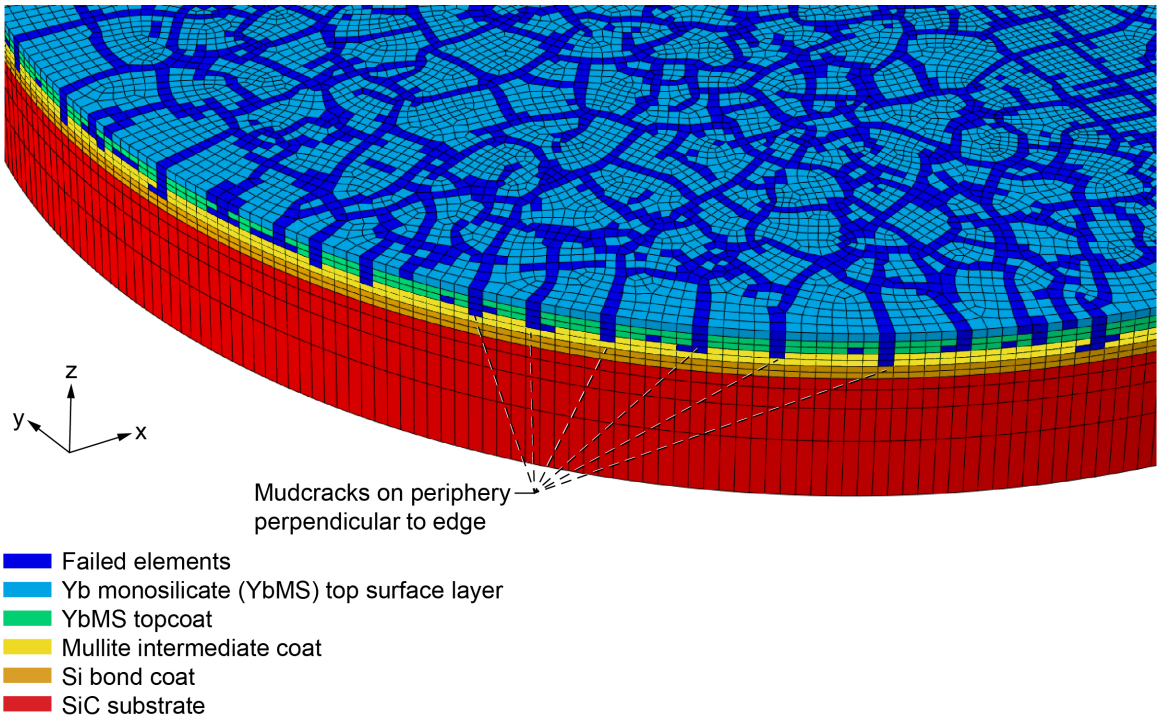

Figure 23.—Mudcracks on disk periphery. Shown are individual layers in EBC system and corresponding failed elements. Failed elements are shown with single darker color and regardless of the color associated with material layer. Failed elements showing arrangement of mudcracks on top surface of disk and along disk periphery during simulation run for Weibull modulus m_V = 5.0 at 23 °C. Mudcracks on periphery are perpendicular to edge.

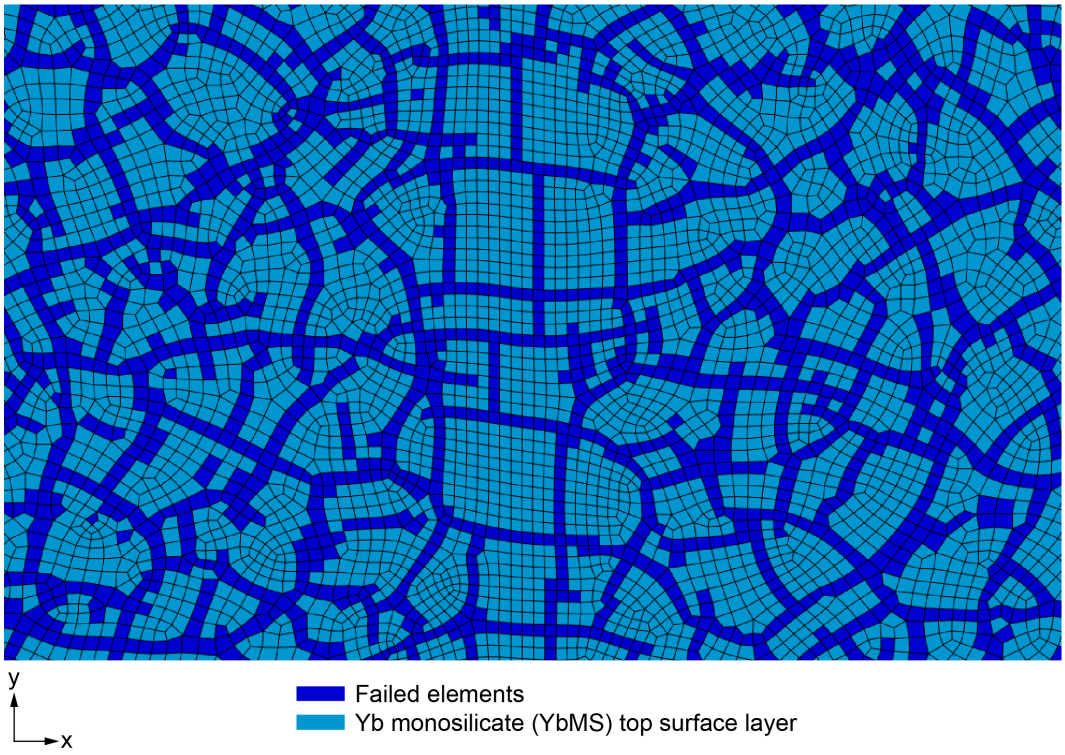

Figure 24.—Closeup of cracking damage for Weibull modulus m_V = 5.0 at 23 °C.

Figure 25 shows a side-by-side comparison of a FEAMAC/CARES simulation of the YbMS EBC material system for m_V = 5.0 at 317.3 °C (corresponding to Figure 22(e)) to a photo of desiccated layer of synthetic clay suspension in a circular petri dish (reproduced from Sadhukhan et al., 2007). The two images are not to scale. The disk of the FEAMAC/CARES simulation is 1.0 cm in diameter, and the circular petri dish is 10.0 cm in diameter. Regardless, the FEAMAC/CARES simulation shows a clear qualitative resemblance to the desiccated synthetic clay suspension, particularly with the mudcracks along the periphery. This visual similarity of fracture pattern occurs for completely different material systems and environmental conditions and implies that similar stress distribution and fracturing processes occur. As mentioned before, the shape of the mudflat cells are influenced by the FE mesh layout. However, the irregular layout of the FE mesh (e.g., see Figure 19(c)) appears to have provided a better visual resemblance to the synthetic clay suspension in the petri dish. The clear resemblance between Figure 25(a) and Figure 25(b) appears to display a level of self-similarity or scale invariance of the crack pattern.

Figure 26 shows x- and y-plane cut views from FEAMAC/CARES simulations of the damage through the coating layers for Weibull moduli m_V = 2.5, 5.0, and 10.0 after cooldown (at 23 °C). The cut-plane graphics rendering feature is useful to view internal damage, such as depth of penetration of mudcracks, formation of delamination, and spallation. It was originally anticipated that cut views would provide a straightforward means to determine mudcrack spacing, similar to the SEM micrograph results of Figure 3 and the results of the 2D FE model of Figure 8, Figure 11, and Figure 13. Figure 26 shows that some failed element crack boundaries (the fracture plane of the crack) can run parallel to the cut-plane view (largely due to the element mesh arrangement). These exposed fracture (crack) planes appear as patches of connected failed elements in the cross section in these figures. This made the determination of mudcrack spacing or crack density of the FE model more problematic. It was decided to ignore (not count) the patchy areas and instead count the mudcracks that intersected these regions that were also directly connected to the plane of the cut view. The only mudcracks counted were those located within the 8.0-mm center section span of the disk cross section (ignoring the 1.0-mm section away from the disk edge on either side). The crack spacing or density about the periphery of disk FE model was also determined since mudcracks there were mostly perpendicular to the disk edge (e.g., see Figure 23).

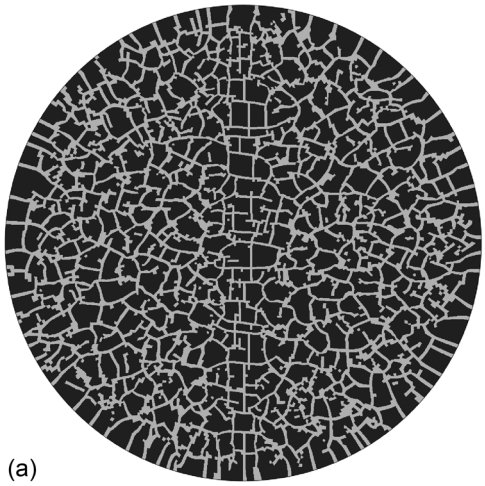
(a)

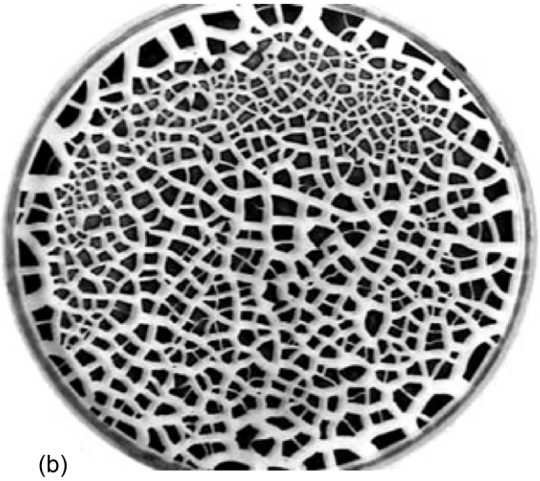
(b)

Figure 25.—Comparison of mudcrack pattern from FEAMAC/CARES simulation of ytterbium monosilicate (YbMS) EBC and desiccated layer of synthetic clay suspension in petri dish. (a) FEAMAC/CARES simulation of 1.0-cm-diameter disk of YbMS EBC material system for Weibull modulus m_V = 5.0 at 317.3 °C (corresponding to Figure 22(e)) shown without FE mesh grid lines. The failed elements are shown with lighter shading. (b) Desiccated layer of synthetic clay suspension in 10.0-cm-diameter petri dish (from Sadhukhan et al., 2007).

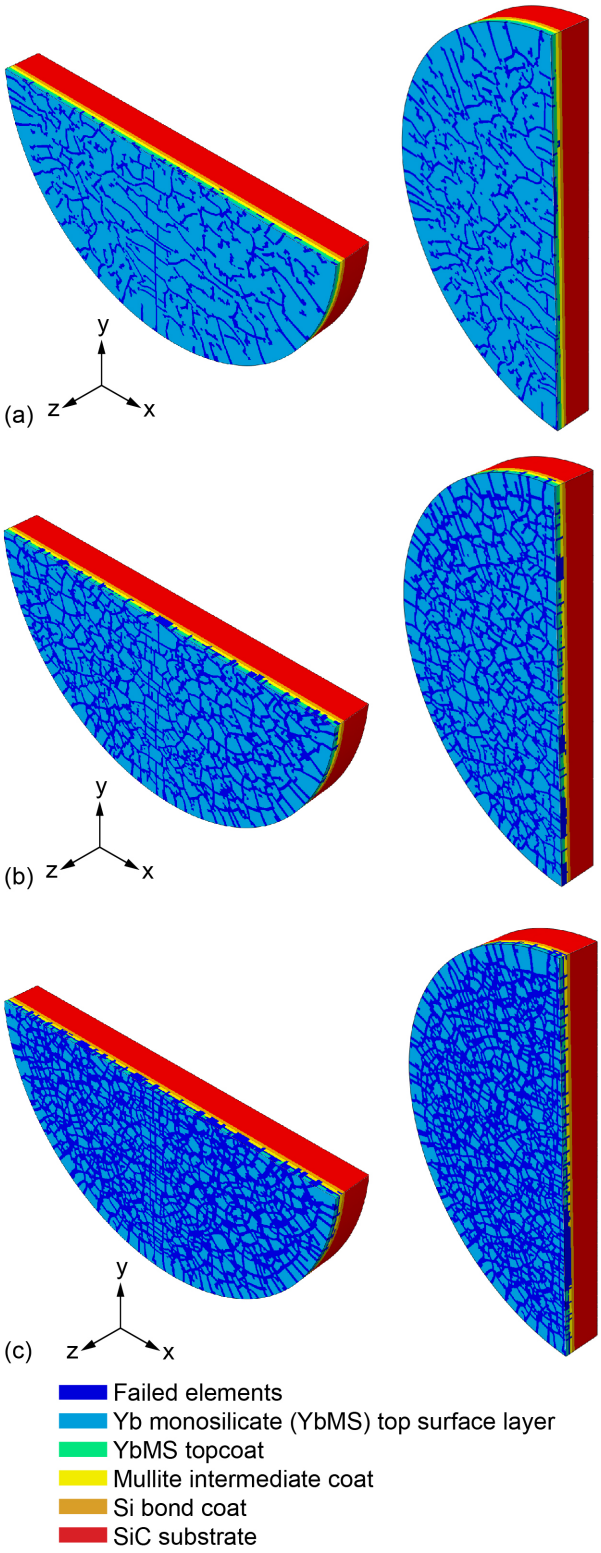

Figure 26.—Cut view of damage through EBC layers for FEAMAC/CARES simulation at 23 °C; y-plane (left) and x-plane (right) cut views. (a) Weibull modulus m_V = 2.5. (b) m_V = 5.0. (c) m_V = 10.0.

TABLE II.—COMPARISON OF AVERAGE CRACK SPACING VERSUS WEIBULL MODULUS m_V AND FE MODEL OVER CENTER SPAN OF EBC COATING SYSTEM[a]

[At 23 °C.]

FE model		Average crack spacing,[b] µm		
		m_V = 2.5	m_V = 5.0	m_V = 10.0
Two-dimensional cross section[c]		210[d] / 140[e]	100	53
Three-dimensional disk (cut-view cross section)[f]	x-plane	320	333	190
	y-plane	360	350	200
Three-dimensional disk (periphery)		698	413	349

[a]Yb_2SiO_5 topcoat, $Al_6Si_2O_{13}$ intermediate coat, Si bond coat, and SiC disk substrate.

[b]For comparison, average crack spacing from Richards et al. (2016) is 240 µm.

[c]See Figure 8, Figure 11, and Figure 13, over 3 mm across center.

[d]Not including top surface layer.

[e]Including top surface layer.

[f]See Figure 26, over 8 mm across center.

Table II summarizes the results for average crack spacing for the various FE models. Most obvious is that there is a large disparity in the crack spacing between the cut-view cross section of the 3D FE model of the disk and the 2D FE model cross section. Unfortunately, the reason for this disparity has not been resolved. Recall that the element stresses in the 2D model are proportionally increased by a factor of 1.363 to match the peak stresses in the 3D FE model. It is expected that this would have made the crack densities between the two models more comparable. Instead, it appears to have had an opposite effect. The 2D cross-section FE model has a substantially denser mesh than the 3D FE disk model. As previously mentioned, it was not practical to make the element sizes (and number of element layers) of the 3D model more closely match the 2D FE model because of computer memory limitations and the long simulation runtimes involved. The relative coarseness of the 3D mesh compared to that of the 2D cross-section model may not have allowed stress relaxation and stress redistribution to more completely develop as damage progressed. There may be other factors involved as well. The stress states for the 2D and 3D models are different, and the fracturing process in a 2D versus 3D space may behave differently with the FEAMAC/CARES algorithm as well. The disparity in the crack densities between the 2D and 3D models is a valid criticism that will have to be left for future work to better resolve.

Some of the differences in the average crack spacing between x- and y-plane cut views for the 3D disk model might be

explained as artifacts of the layout of the mesh geometry. Also, as shown in Table II, there is not as clear of a correlation of results as the Weibull modulus increases in value for the 3D disk model. This is seen for $m_V = 5.0$ where the average crack spacing is almost identical to that for $m_V = 2.5$. We expected that the actual value would have been more in the middle between that of $m_V = 2.5$ and 10.0. We do not believe that this lack of a difference could be explained as a statistical outlier since the length of the cross section we examined should have been sufficiently large that the stochastic effects are minimized (that is, there were many mudcracks found over the length). Again, this lack of disparity requires further investigation.

The average crack spacing about the periphery of the 3D disk FE model is also listed in Table II. The periphery of the disk was 31.4 mm in length with a more regular mesh spacing as opposed to the 8.0-mm examined length of the cut-plane views. Because the peak principal stress at the edge of the disk is lower than at the interior of the disk towards its center as seen in Figure 20 (on the disk exposed surface), the average crack spacing at the periphery is larger than at the cut-view cross section, as would be expected. Also, the average crack spacing for $m_V = 5.0$ is substantially smaller than that for $m_V = 2.5$ and closer to that for $m_V = 10.0$. This is converse to the results listed for the cut-view cross section. We had expected that the actual value would have been more in the middle between that of $m_V = 2.5$ and 10.0; however, this does not mean the results listed are clearly wrong either.

Figure 27, Figure 28 (Figure 29 associates with Figure 28, as explained later), and Figure 30, show the damaged elements on the disk surface and through the coating layers for Weibull modulus $m_V = 2.5$, 5.0, and 10.0, respectively, at the cooling temperature of 611.5 °C and room temperature 23 °C. Figure 28 shows the results from the simulation of Figure 22. The undamaged (unfailed) elements are made invisible in the figure parts ii and iii, leaving only the failed elements visible. This is a very convenient way to see damage through the coating layers and see how the cracking damage links up into filaments of connected failed elements. The front and back sides of the disk are shown in this manner. In the three figures it can be seen that as the Weibull modulus increases, the amount of damage increases and more (and subsequently smaller sized) mudflat cells form or segment. Aside from the amount of damage that lead to more fully developed failure modes (e.g., delamination, spallation), there did not appear to be a particularly distinguishing feature in the damage pattern development versus the value of Weibull modulus.

In Figure 27 part iii, for Weibull modulus $m_V = 2.5$, there are some failed elements in the bond coat along the rim of the disk. A similar failure in the bond coat can be seen in the right-hand side of Figure 11(c), (d), and (e), the only analogous bond coat failure shown in the 2D FE model of the EBC cross section. This adds some credence to the conclusion that this may be a valid failure mode as opposed to it being an anomaly. Failed elements in the top surface did not uniformly penetrate into the additional material layers, as can be seen in part iii of Figure 27. Early damage (element failure) appeared to develop in both the top surface layer and the topcoat practically simultaneous and independent of one another, with some bias (more damage) appearing in the top surface coat. After complete cooldown at 23 °C there were approximately 45 mudcracks along the disk periphery with a 698-µm average crack spacing.

In Figure 28 for Weibull modulus $m_V = 5.0$, a clear mudflat cracking damage pattern develops (with complete mudcracks). The early damage (element failure) appears to develop primarily in the top surface layer and then later in the topcoat. In this case, the damage that develops in the top surface layer tends to quickly penetrate into the topcoat. The damage in the topcoat tends to be directly connected to the crack filaments of the top surface layer damage. There is one instance of bond coat initial delamination in the simulation. Closeups of this bond coat failure are shown in Figure 29 at 779.2 and 23 °C. The figure also shows the individual element boundaries. Delamination can be seen to be developing in the topcoat layer at the interface between the topcoat layer and the intermediate coat layer. This failure mode was not clearly developed in the 2D FE model of the EBC cross section in Figure 11(e) for $m_V = 5.0$, but can be seen to be forming for $m_V = 10.0$ in Figure 13(e). After complete cooldown at temperature 23 °C, there were approximately76 mudcracks along the disk periphery with a 413-µm average crack spacing.

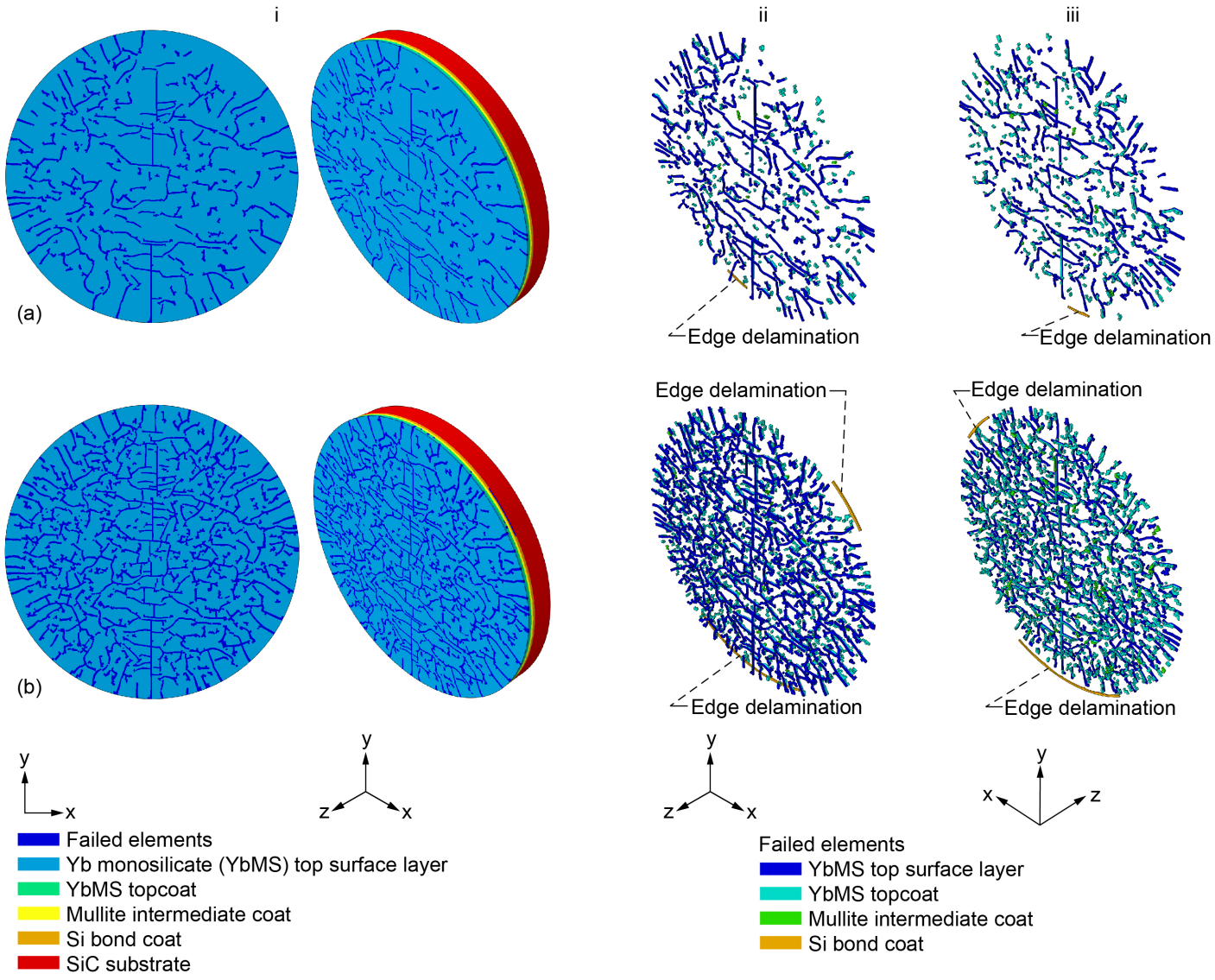

Figure 27.—Damage through EBC layers for Weibull modulus m_V = 2.5, showing (i) rotated views, (ii) damaged elements on front side, and (iii) damaged elements on back side. (a) At 611.5 °C. (b) At 23 °C.

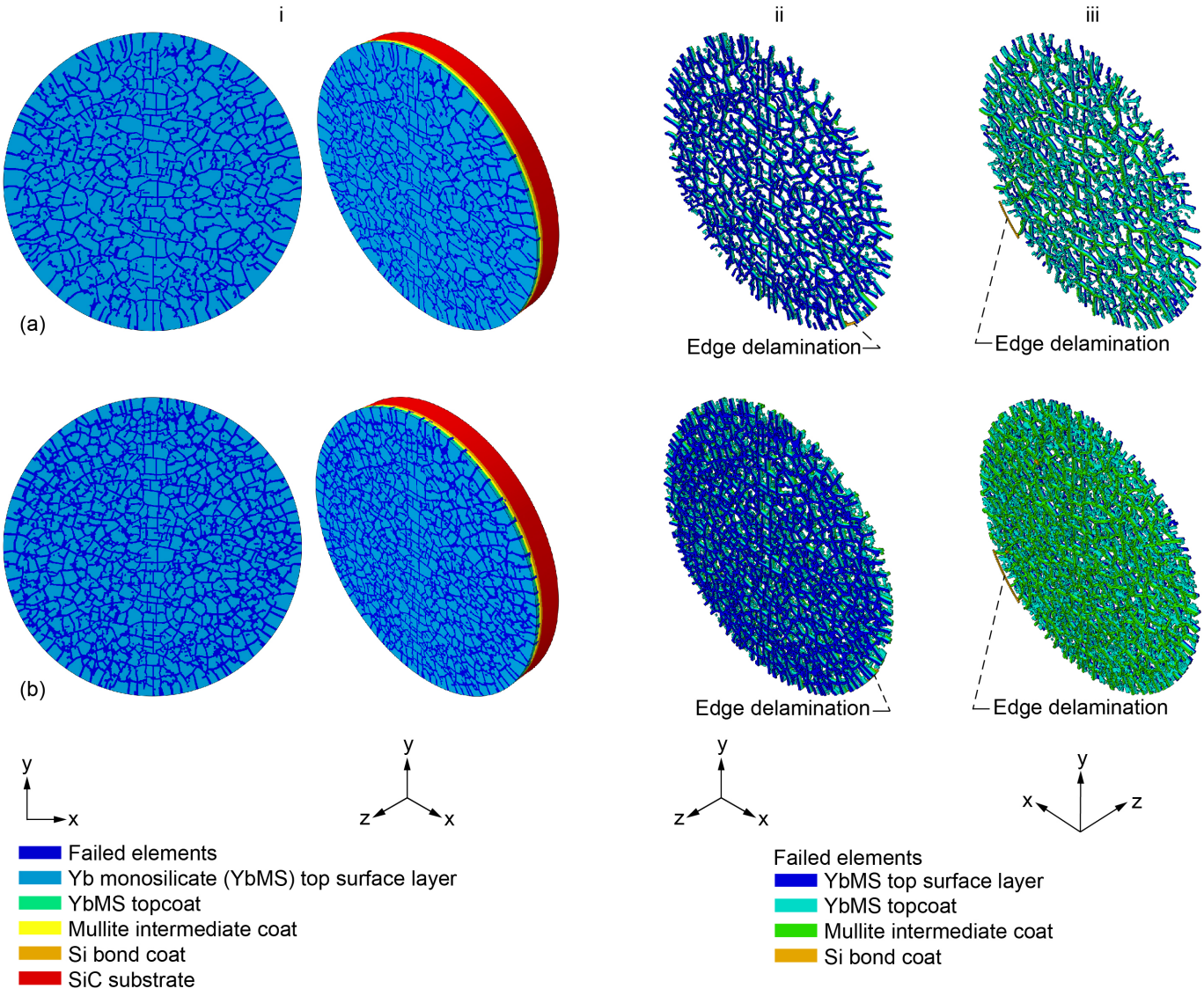

Figure 28.—Damage through EBC layers for Weibull modulus m_V = 5.0, showing (i) rotated views, (ii) damaged elements on front side, and (iii) damaged elements on back side. (a) At 611.5 °C. (b) At 23 °C.

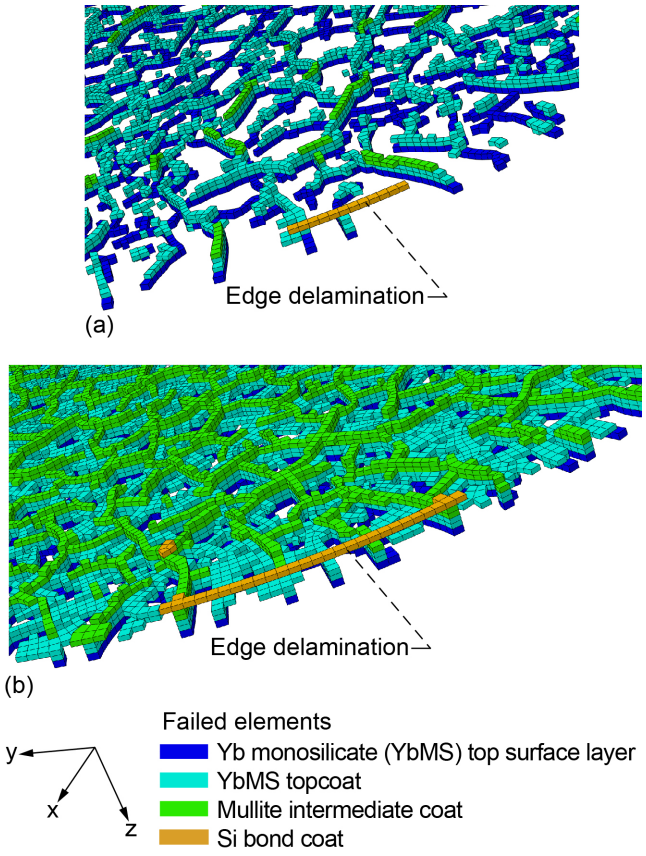

Figure 29.—Closeup views of bond coat failure, showing the individual element boundaries; underside (bottom up) perspective view. (a) At 779.2 °C. (b) At 23 °C.

In Figure 30 for m_V = 10.0 the mudflat cracking pattern has developed to a greater degree of saturation than for the case of m_V = 5.0 in Figure 28, and it develops in the same manner. Elements adjacent to (touching) mudcrack planes did not initially fail, unlike they did for the 2D FE cross-section model shown in Figure 14. Figure 30(b) parts ii and iii show that where the failure occurs in the topcoat layer of elements, there is a complete or near-complete delamination at the interface between the topcoat layer and the intermediate coat layer. There does not appear to be any instance of bond coat failure, unlike that shown in Figure 27 to Figure 29. The reason for this is unclear. After complete cooldown at temperature 23 °C there were approximately 90 mudcracks along the disk periphery with a 349-μm average crack spacing.

Summarizing the findings of this section, we show that a FEAMAC/CARES 3D model can be used to simulate the formation and growth of crack-like damage events and the spontaneous formation of mudflat cracking patterns from thermal loading (see Figure 22, Figure 27, Figure 28, and Figure 30). The effect of three different values of Weibull modulus, m_V = 2.5, 5.0, and 10.0 on the character of damage development were investigated. To do this, we used a highly refined mesh consisting of low-aspect-ratio brick elements to model a 3D FE model of an EBC multilayered coating system attached to a ceramic substrate, along with a simple methodology of an abrupt 99-percent reduction of the elastic modulus of FEs when a failure condition was achieved. A 3D FE model of a 1.0-cm-diameter by 1.0-mm-thick disk composed of a three-layer thin-film EBC deposited on a SiC substrate was prepared (Figure 19). The disk was assumed to have an initial annealing temperature of 1,300 °C that was subsequently cooled to room temperature. The cooldown elicited the buildup of large residual stresses that were equibiaxial tensile on the surface of the disk towards the disk center and uniaxial tensile on the edge of the disk, but parallel to that edge, as shown in Figure 20. These residual stresses caused the spontaneous initiation of mudcracking, which led to the subsequent development of mudflat cracking such as that shown in Figure 22. The uniaxial tensile stress at the edge of the disk and oriented parallel to that edge initiated the development of mudcracks at that edge, oriented perpendicular to the disk edge, as shown in Figure 23. As the cooling progressed, the mudflat refragment into progressively smaller sizes in a manner consistent with a fractal-governed geometric behavior. The average crack segmentation length (or conversely the average crack density) was determined versus the value of m_V when the Weibull scale parameter σ_{0V} and all other parameters were held constant (shown in Table II). This crack density increased as the value of m_V increased. However, the relative coarseness of the mesh (Figure 19 compared to the 2D model of the EBC cross section of Figure 6) and mesh layout affected the accuracy of these results. Other cracking failure modes could also be reproduced from the simulations, such as the beginning of edge cracking delamination in Figure 27, Figure 28, and Figure 29, and developing layer delamination of the topcoat layer from the intermediate coat shown in Figure 28 and Figure 30, parts ii and iii. The fracture pattern followed the path of the FE mesh layout. Individual failed elements could be visually isolated from the unfailed elements so that the entire structure and organization of the damage development through the coating layers could be clearly observed.

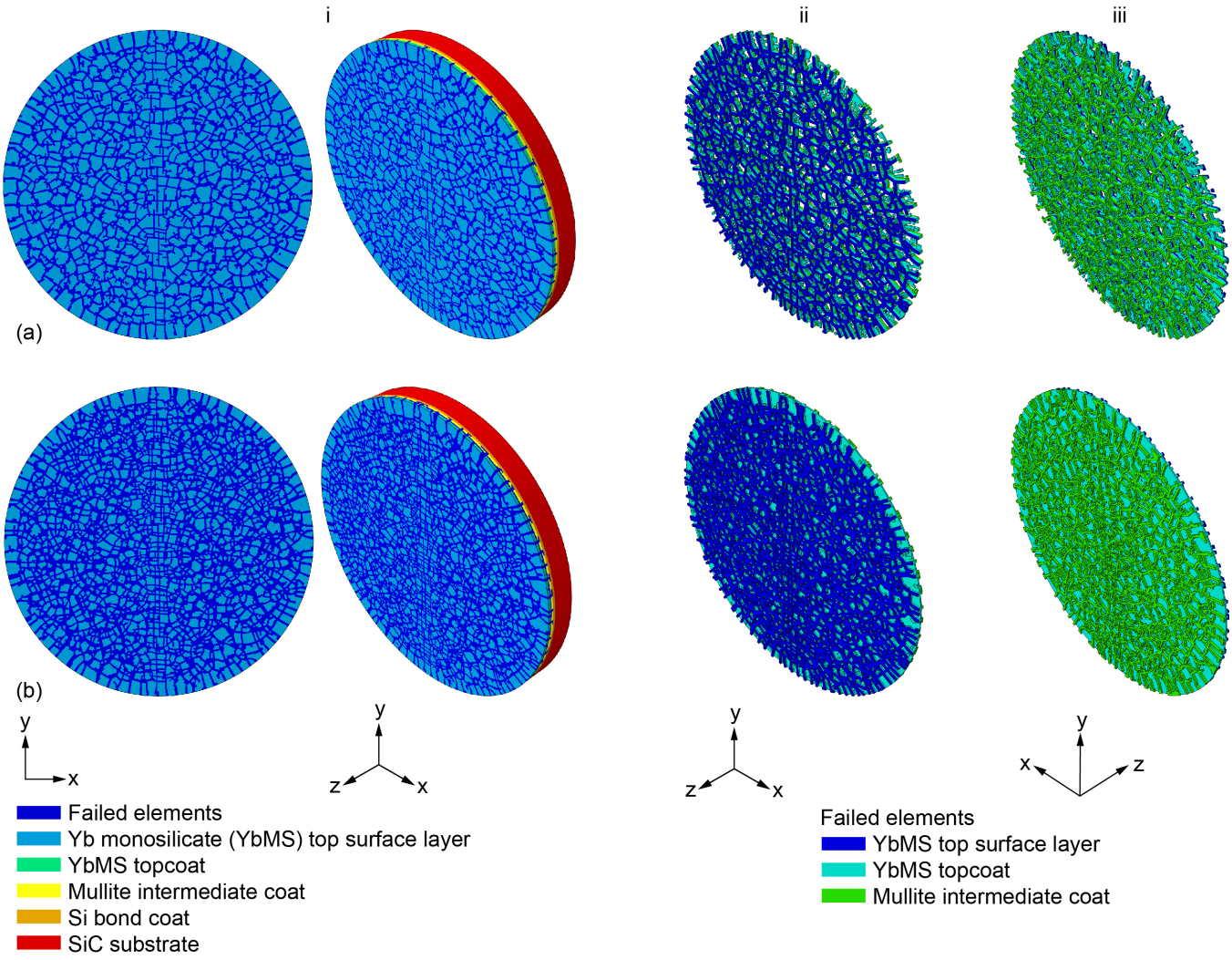

Figure 30.—Damage through EBC layers for Weibull modulus m_V = 10.0, showing (i) rotated views, (ii) damaged elements on front side, and (iii) damaged elements on back side. (a) At 611.5 °C. (b) At 23 °C.

7.0 Summary and Conclusions

The Finite Element Analysis—Micromechanics Analysis Code/Ceramics Analysis and Reliability Evaluation of Structures (FEAMAC/CARES) program was used to simulate the formation of mudcracks from cooldown on a multilayered environmental barrier coating (EBC) system deposited on a ceramic substrate. FEAMAC/CARES combines the Micromechanics Analysis Code with Generalized Method of Cells MAC/GMC multiscale composite micromechanics code with the CARES/*Life* probabilistic multiaxial failure criteria code and the Abaqus finite element (FE) analysis code. The EBC analyzed here was a three-layered ytterbium monosilicate (topcoat), mullite (intermediate coat), and silicon (bond coat) system on a silicon carbide substrate. The EBC experienced a cooldown from an initial (residual stress free) annealing temperature to room temperature. This resulted in the buildup of tensile residual stresses in the topcoat and intermediate coat layers and compressive stresses in the bond coat layer due to thermal expansion mismatch of the constituent materials. This caused the formation of mudcracks as the EBC cooled. A two-dimensional (2D) FE model of a cross section of EBC material system on a ceramic substrate and a three-dimensional (3D) FE model of a small disc-shaped specimen of the same material arrangement were prepared. The FE models were composed of many small-sized low-aspect-ratio elements, which enabled the formation of crack boundaries that led to mudcracking. At the start of a simulation, the individual FE Gaussian integration points of a FE model were seeded with randomly assigned probabilities of failures (chosen from a uniform probability distribution). When the CARES/*Life* calculated probability of failure (for the particular element integration point and associated element integration point volume) exceeded the randomly assigned probability of failure at some point in the loading sequence, the elastic modulus of the particular element Gaussian integration point was reduced by 99 percent (which was maintained for the rest of a simulation). FEAMAC/CARES also employed a simple cellular automaton methodology that adjusted the previously assigned (seeded) random failure probabilities of elements adjacent to a failed element. This approach has been shown to produce crack-like or crack-mimicking growth patterns.

A two-parameter Weibull distribution was used to characterize the coating layer stochastic strength response, and the effect of three different values of Weibull modulus, m_V = 2.5, 5.0, and 10.0, on the formation of mudcrack damage was examined. During a simulation, a pattern of mudcracking would spontaneously form. As the simulated cooldown proceeded in the 2D FE model of the cross section, additional mudcracks would form, and eventually a periodic arrangement of mudcracks would result. The average crack spacing or crack spacing length was shown to be dependent on the value of the Weibull modulus, where a higher value of Weibull modulus resulted in smaller average mudcrack spacing length. In the simulations with the FE model of the EBC cross section, various failure modes were observed such as the mudcracking, layer delamination, edge delamination, and spallation. In the 3D FE model of the disk, mudcracks would form and link up into mudflat cells. This would progressively develop into smaller and smaller mudflat cells as the cooldown proceeded in a manner consistent with a fractal behavior. In the simulations with the 3D FE model of the EBC-coated disk on ceramic substrate, failure modes were observed such as mudcracking (incomplete early on), mudcrack cell formation (complete and closed cells), layer delamination, edge delamination, and mudcracks that would form perpendicular to the edge of the disk. The average crack spacing or mudcrack cell size was dependent on the value of the Weibull modulus, where higher value of Weibull modulus resulted in smaller average mudcrack spacing length or mud cell sizes.

This work also revealed some shortcomings with the methodology reported here. For example, crack trajectories tended to follow the FE grid layout. Crack tip singularities were not explicitly modeled, nor was the mechanics of crack penetration and deflection at bi-material interfaces included. Further work and development in these areas is needed. Nevertheless, this fairly straightforward approach was able to capture many relevant factors observed in mudflat cracking.

Clearly, a two-parameter Weibull distribution describing the individual strength responses of the brittle material constituents of the EBC layers can be used to simulate the development of thin-film failure modes such as mudflat cracking, delamination, and spallation. This initial work can serve as a foundation for which further modeling of enviromechanical phenomena that evolve with time and loading can be added. FEAMAC/CARES was developed to investigate and provide a more physically based, and accurate, life prediction and simulation methodology for an EBC on a component. With further development, it could be used to help determine optimized safe-life design margins, and ultimately provide an additional means to help develop and verify coatings on components with improved performance.

Appendix—Related Literature on Failure Mechanisms, Mudcrack Characterization, and Modeling

In this report a physical basis and heuristic computational methodology is described that is capable of simulating the initiation of channel cracking and fully formed mudcracks on an environmental barrier coating (EBC) surface. This appendix provides the technical literature that was found regarding the physics and simulation modeling of this phenomena. This is only a limited survey.

Information on coating mechanics, mechanical failure mechanisms, and failure modes for thin-film coatings and multilayers can be found in references like Hutchinson and Suo (1991), Evans and Hutchinson (1995), and Hutchinson (1996), and those more specifically for thermal barrier coatings (TBCs) include Evans, Wang, and Mumm (1998); Evans et al. (2001); Mumm and Evans (2001); and Levi et al. (2012), who includes degradation mechanisms for calcium-aluminum-magnesium-silicate (CMAS: CaO-MgO-Al_2O_3-SiO_2). Hutchinson and Evans (2002) and Evans and Hutchinson (2007) examine delamination of TBCs in a thermal gradient. Mercer et al. (2005) and Krämer et al. (2008) look at cracking and delamination due to CMAS penetration. Evans, He, and Hutchinson (2001) examine the effect of local layer undulations and the growth of thermally grown oxide on the development of cracking and buckling from compressive stresses on a TBC. Ricks, Arnold, and Harder (2018) perform a sensitivity study to examine the influence of uniformly and nonuniformly grown oxide layer on the associated driving forces leading to mechanical failure (spallation) of an EBC layer. Crack-driving forces in a multilayered coating is examined by Ghosn, Zhu, and Miller (2005).

There is much technical literature available in the subject areas of "mudcracks," "mudflat cracks," or "desiccation cracks," and these technical papers address or model various aspects of the phenomena. First, desiccation cracks generally show a scale invariance of the crack pattern and has been shown to be fractal by various groups such as Colina and Roux (2000), Mal et al. (2006) and Baer, Kent, and Anderson (2009). The technical literature regarding desiccation cracks spans different application areas from geotechnical analysis to computer graphics. For example, an early investigation by Kindle (1917) examines the variation of conditions of mudcrack pattern formation, including rapid and slow desiccation and composition of mud, for the purpose of helping to determine the likely environmental conditions at the time of the formation of the mudcrack fossils. Nearly 100 years later Khatun, Dutta, and Tarafdar (2015) studied the role of layer thickness on crack patterns developed on desiccating films of bentonite clay on a glass substrate. In another study, Groisman and Kaplan (1994) show there is a linear relation between the scale of the crack pattern and the thickness of the mixture layer, and they propose a scaling law between the thickness of the mixture layer and the characteristic size of the cells. Morris, Graham, and Williams (1992) develop solutions for the mechanics of soil cracking from desiccation using elasticity theory, linear elastic fracture mechanics (LEFM), and the transition between tensile and shear failure and then relate that to crack depths observed in nature. Nahlawi and Kodikara (2006) study clay soil desiccation in narrow rectangular molds. The lengths of the molds are found to be considerably larger than their widths so that parallel cracking to the width direction was generated. The desiccated clay would form regularly spaced cracks (segmentation cracking). The speed of desiccation, crack segmentation length, and statistical distribution of measured lengths for a given set of test conditions were studied. The number of cracked segments per unit length describes the crack density and is usually described from the average number of cracked segments per unit length. Papers such as these demonstrate the complexity of the problem and the numerous factors involved in the formation of the phenomena.

Crack spacing or segmentation length in desiccated materials or relative shrinkage of (thin) films on elastic or rigid substrates under various load conditions have been analyzed and modeled for brittle-material films including drying and embrittled muds, paint, asphalt, and ceramics. These phenomena have also been observed and modeled in fiber-reinforced composites, although those references will not be specifically cited here. Crack spacing, or more to the point, periodic crack spacing is mentioned because it is a direct outcome predicted from the thin-film simulations performed here with the integrated Finite Element Analysis—Micromechanics Analysis Code/Ceramics Analysis and Reliability Evaluation of Structures (FEAMAC/CARES) program. It is therefore appropriate to mention some of the previous literature that investigates and models this phenomenon. For example, Thouless (1990) provides a solution for the minimum spacing that can exist between propagating cracks in thin films, suggesting there is little interaction between cracks that are spaced by more than approximately 8 times the film thickness. Shenoy, Schwartzmann, and Freund (2001) extend this work to account for mismatch in elastic constants between the film and the substrate. Cassenti (1991) derives a segment-size probability distribution based on the Weibull distribution, describing brittle material stochastic strength from simple tensile loading. Yanaka et al. (2001) analyze mudcracking on a silicon oxide film deposited on a polyethylene terephthalate substrate. They use finite element (FE) analysis and Monte Carlo simulation to successfully predict the distribution of fragment lengths as

mudcracking progressed. The Weibull parameters of the film are determined from the scatter of the crack onset strain. Xia and Hutchinson (2000) propose a two-dimensional (2D) model simulating straight and curved crack propagation paths in thin elastic films where single and multiply spaced cracks are considered. Timm, Guzina, and Voller (2003) develop a model of thermal shrinkage of elastic pavement on an elastoplastic, cohesive-frictional base to predict average cracking spacing. Hsueh and Yanaka (2003) analyze and model multiple-film cracking of brittle films on substrates (a major reliability problem in microelectronics components and their protective coatings), by considering a three-dimensional (3D) geometry to predict crack density under unidirectional loading with residual stresses. Conversely, Seghir and Arscott (2015) examine residual stresses that develop on thin-film coatings with the objective to generate and tune crack-based patterns without using lithographic intervention. They speculate that control of mudcrack patterning formation could have useful technological applications. Hsueh and Wereszczak (2004) model crack density as a function of applied strain for mudcracking of well-adhered brittle coatings such as paint. Zhang et al. (2008a and b) perform analyses of periodic film cracking on semiconductor films deposited on silicon substrates with residual stresses and applied strain. Leguillon et al. (2014) describe the need for two conditions to predict crack nucleation involving energy and stress and also discuss fragment size (segmentation length) versus layer thickness. Leguillon et al. (2016) and Leguillon, Li, and Martin (2017) analyze and predict multicracking in brittle thin films using a "finite fracture mechanics" approach based on a "coupled criterion." A novelty of their approach was to incorporate a "periodic representative cell" to handle an increasing number of cracks.

In the computer graphics and animation industry realistic rendering of natural phenomena is required. The works of O'Brien (2000), O'Brien and Hodgins (1999), Iben and O'Brien (2009), and Pfaff et al. (2014) are particularly noteworthy in their ability to simulate photorealistic cracking patterns for a variety of substances including ceramics, glass, and wood as well as mud drying into mudcracked fracture patterns. One key of their technique is local remeshing around advancing crack fronts. In their simulations, they use triangular elements to model the body of interest. The failure criterion they use is deterministic, although the mesh generation introduced a random component to this threshold (O'Brien, 2017, private communication). In their fracture algorithm, after every time step and at each node a tensor that describes how the internal forces were acting to separate that node is determined. If the force was sufficiently large, the node was split into two distinct nodes, and a new fracture plane was computed in a direction that was perpendicular to the direction of the largest tensile load.

Sanchez, Manzoli, and Guimaraes (2014) model the fragmentation behavior of drying soils by inserting high-aspect-ratio elements in between standard elements of a FE mesh. They call their methodology the smooth particle hydrodynamics (SPH) method. The high-aspect-ratio elements act as cohesive elements to provide a cracking path. Bui et al. (2015) extend the SPH method to simulate shrinkage-induced soil cracking.

Valette et al. (2008) model and visualize cracks on the surface of desiccating crusted soil. They use a grid-based approach where the terrain consists of a grid work of small cubic cells. They propose a method to dynamically produce 3D quasi-static fractures using "shrinkage volumes" to get a realistic appearance of cracks and "watershed transformation" to compute crack paths.

Paluszny and Matthäi (2009) describe a FE-based method to propagate multiple fractures simultaneously in geological brittle media. Their method (1) seeds a 2D rectangular region with random flaws, creates a mesh, and solves the FE problem; (2) computes stress intensity factors, propagation lengths, and directions for all crack tips; and (3) then adaptively remeshes the FE model at all crack tips and repeats the FE solution procedure until no growth is recorded for the fixed boundary conditions.

Matsubara et al. (2016) develop a numerical model using 3D FE analysis for mudcrack growth in Bentonite pastes. A smeared crack model is used, and mode I crack propagation is used in all FEs. The Young's modulus and tensile strength are randomly varied within a specified range. They report the fractal dimension of the cracking pattern is consistent between simulation and experimental results.

Some researchers have investigated physical models using a lattice of nodes connected through springs (spring-network model), which break when a critical strain or force is reached. These include Skjeltorp and Meakin (1988); Hirota, Tanoue, and Kaneko (1998) in 2D and 3D network models; and Vogel et al. (2005a) who examine the variety of crack patterns through a systematic exploration of the relevant parameters. Sadhukhan et al. (2007) investigate desiccation cracks on different substrates, and Sadhukhan et al. (2008) investigate cracking and peeling of a desiccating layer of clay simulated using a spring model.

Gobron and Chiba (2001) use cellular automata (see Gobron and Chiba, 1999) to propagate cracks in 3D solid models. A cellular automata technique is also used in Nemeth et al. (2016a and b) to model fragmentation and stochastic toughening in composite materials. The technique was then used by Nemeth et al. (2017) and Nemeth et al. (2018) where the FEAMAC/CARES methodology is first demonstrated to model cracking in an EBC system.

Horgan and Young (2000) present a model based on the geometry of 2D crack growth for the fragmentation of drying soil. This includes modeling crack growth as a random walk and "attraction of cracks" within defined distances.

Regarding probabilistic modeling, Chertkov and Ravina (1998) develop a physically based probabilistic model for the dependence of crack concentration on soil depth for prediction of crack network geometry. Cassenti (1991) develops a probabilistic failure model based on the Weibull distribution of brittle material strength to predict fracture segment size and statistical failure locations in ceramic coatings and ceramic matrix composites (CMCs). The model is added as a postprocessor to a FE code and is used to analyze design concepts for a turbine combustor. Yanaka et al. (2001) also develop a probabilistic failure model based on the Weibull distribution of brittle material strength to predict fracture segment size in a thin-film coating.

Sukumar and Prévost (2003) and Liang et al. (2003) model cracking using the X-FEM method with additional customized software where crack modeling could be carried out without the need to mesh the crack surfaces and where remeshing was not required for crack growth problems. Huang, Sukumar, and Prévost (2003) demonstrate this methodology by simulating the growth of mudcrack patterns. Their simulation uses a seeded model of randomly sized, distributed, and oriented initial cracks in a 2D FE mesh. (Note: the FEAMAC/CARES methodology avoids this approach by instead seeding the individual FE Gaussian integration points of a FE model with randomly assigned probabilities of failures, chosen from a uniform probability distribution.) Huang, Sukumar, and Prévost (2003) also model the spallation of a coating on a substrate from an initial edge precrack. Similar work is done by Liang et al. (2003).

Jabakhanji and Mohtar (2012) and Jabakhanji (2013) develop a coupled peridynamic model for mechanical deformations and transient moisture in unsaturated soils, simulating the initiation and evolution of cracks triggered by volumetric strains in the soil. The peridynamics formulation (Silling, (2000)) avoids the need for the techniques of fracture mechanics.

Minkowski densities and functions have been used to compare real desiccation-crack patterns to simulated crack patterns in Vogel, Hoffmann, and Roth (2005b), Vogel et al. (2005a), and Valette et al. (2008). Roth, Boike, and Vogel (2005) use Minkowski densities and density functions to quantify patterns in permafrost. Minkowski densities and density functions are measures for quantifying arbitrary binary patterns. The study shows the Minkowski functions at a "single scale," which essentially consists of a network of black lines that are of roughly equal thickness for a purely fractal pattern. The single-scale pattern is of the nature of mudcracking. Minkowski functions are a useful descriptor of surface morphology and a means by which surface topology may be described and simulated from a set of mathematical functions.

Abdul-Aziz et al. (2014) predict the life for an EBC-coated CMC specimen using FE analysis with progressive failure analysis that included durability, damage tracking, and a material degradation model. This approach did not include probabilistic modeling or simulate crack formation.

References

Abdul-Aziz, Ali, et al. (2014): Durability Modeling of Environmental Barrier Coating (EBC) Using Finite Element Based Progressive Failure Analysis. Journal of Ceramics, vol. 2014, Article ID 874034, 2014.

Aboudi, Jacob; Arnold, Steven; and Bednarcyk, Brett (2012): Micromechanics of Composite Materials: A Generalized Multiscale Analysis Approach. First ed., Elsevier, Oxford, England.

Baer, J.U.; Kent, T.F.; and Anderson, S.H. (2009): Image Analysis and Fractal Geometry To Characterize Soil Desiccation Cracks. Geoderma, vol. 154, nos. 1–2, pp. 153–163.

Barnett, R.L., et al. (1967): Fracture of Brittle Materials Under Transient Mechanical and Thermal Loading. AFFDL−TR−66−220.

Batdorf, S.B.; and Crose, J.G. (1974): A Statistical Theory for Fracture of Brittle Structures Subjected to Nonuniform Polyaxial Stresses. J. Appl. Mech., vol. 41, no. 2, pp. 459−464.

Batdorf, S.B.; and Heinisch, H.L., Jr. (1978): Weakest Link Theory Reformulated for Arbitrary Fracture Criterion. J. Am. Ceram. Soc., vol. 61, nos. 7−8, pp. 355−358.

Bednarcyk, Brett A.; and Arnold, Steven M. (2002a): MAC/GMC 4.0 User's Manual—Example Problem Manual. NASA/TM—2002-212077/VOL3. http://ntrs.nasa.gov

Bednarcyk, Brett A.; and Arnold, Steven M. (2002b): MAC/GMC 4.0 User's Manual—Keywords Manual. NASA/TM—2002-212077/VOL2. http://ntrs.nasa.gov

Bednarcyk, Brett A.; and Arnold, Steven M. (2007): A Framework for Performing Multiscale Stochastic Progressive Failure Analysis of Composite Structures. NASA/TM—2007-214694. http://ntrs.nasa.gov

Bui, H.H., et al. (2015): Soil Cracking Modelling Using the Mesh-Free SPH Method. Proceedings of the 12th Australia New Zealand Conference on Geomechanics (ANZ 2015), Wellington, New Zealand, pp. 122–129.

Cassenti, Brice N. (1991): Time-Dependent Probabilistic Failure of Coated Components. AIAA J., vol. 29, no. 1, pp. 127–134.

Chen, Kuo-Shen, et al. (2002): Effect of Process Parameters on the Surface Morphology and Mechanical Performance of Silicon Structures After Deep Reactive Ion Etching (DRIE). J. Microelectromech. Syst., vol. 11, no. 3, pp. 264–275.

Chertkov, V.Y.; and Ravina, I. (1998): Modeling the Crack Network of Swelling Clay Soils. Soil Sci. Soc. Am. J., vol. 62, no. 5, pp. 1162–1171.

Colina, H.; and Roux, S. (2000): Experimental Model of Cracking Induced By Drying Shrinkage. Eur. Phys. J. E, vol. 1, nos. 2–3, pp. 189–194.

Costello, John A.; and Tressler, Richard E. (1986): Oxidation Kinetics of Silicon Carbide Crystals and Ceramics: I, In Dry Oxygen. J. Am. Ceram. Soc., vol. 69, no. 9, pp. 674–681.

Cruse, T.A.; Johnsen, B.P.; and Nagy, A. (1997): Mechanical Properties Testing and Results for Thermal Barrier Coatings. J. Therm. Spray Techn., vol. 6, no. 1, pp. 57–66.

Dassault Systèmes Simulia (2013): Abaqus Analysis User's Guide. Version 6.13.

DeMasi, J.T.; Sheffler, K.D.; and Ortiz, M. (1989): Thermal Barrier Coating Life Prediction Model Development. Phase 1—Final Report. NASA CR–182230. http://ntrs.nasa.gov

Evans, A.G.; and Hutchinson, J.W. (1995): The Thermomechanical Integrity of Thin Films and Multilayers. Acta Metall. Mater., vol. 43, no. 7, pp. 2507–2530.

Evans, A.G.; Wang, J.S.; and Mum, D. (1998): Mechanism-Based Life Prediction Issues for Thermal Barrier Coatings. Thermal Barrier Coating Workshop, 1997, NASA/CP—1998-207429, p. 45. http://ntrs.nasa.gov

Evans, A.G., et al. (2001): Mechanisms Controlling the Durability of Thermal Barrier Coatings. Prog. Mater. Sci., vol. 46, no. 5, pp. 505–553.

Evans, A.G.; He, M.Y.; and Hutchinson, J.W. (2001): Mechanics-Based Scaling Laws for the Durability of Thermal Barrier Coatings. Prog. Mater. Sci., vol. 46, pp. 249–271.

Evans, A.G.; and Hutchinson, J.W. (2007): The Mechanics of Coating Delamination in Thermal Gradients. Surf. Coat. Technol., vol. 201, no. 18, pp. 7905–7916.

Ghosn, Louis J.; Zhu, Dongming; and Miller, Robert A. (2005): Crack Driving Forces in a Multilayered Coating System for Ceramic Matrix Composite Substrates. Advances in Ceramic Coatings and Ceramic-Metal Systems: A Collection of Papers Presented at the 29th International Conference on Advanced Ceramics and Composites (NASA/TM—2005-213835), vol. 322, Cocoa Beach, FL, p. 159. http://ntrs.nasa.gov

Gobron, Stephane; and Chiba, Norishige (1999): 3D Surface Cellular Automata and Their Applications. JVCA, vol. 10, no. 3, pp. 143–158.

Gobron, Stephane; and Chiba, Norishige (2001): Crack Pattern Simulation Based on 3D Surface Cellular Automata. Visual Comput., vol. 17, pp. 287–309.

Groisman, A.; and Kaplan, E. (1994): An Experimental Study of Cracking Induced by Desiccation. Europhys. Lett., vol. 25, no. 6, pp. 415–420.

Hirota, Koichi; Tanoue, Yasuyuki; and Kaneko, Toyohisa (1998): Generation of Crack Patterns With a Physical Model. Visual Comput., vol. 14, no. 3, pp. 126–137.

Horgan, G.W.; and Young, I.M. (2000): An Empirical Stochastic Model for the Geometry of Two-Dimensional Crack Growth in Soil (With Discussion). Geoderma, vol. 96, no. 4, 2000, pp. 263–276.

Huang, R.; Sukumar, N.; and Prévost, J.-H. (2003): Modeling Quasi-Static Crack Growth With the Extended Finite Element Method. Part II: Numerical Applications. Int. J. Solids Struct., vol. 40, no. 26, pp. 7539–7552.

Hsueh, C.H.; and Wereszczak, A.A. (2004): Multiple Cracking of Brittle Coatings on Strained Substrates. J. Appl. Phys., vol. 96, no. 6, pp. 3501–3506.

Hsueh, C.H.; and Yanaka, M. (2003): Multiple Film Cracking in Film/Substrate Systems With Residual Stresses and Unidirectional Loading. J. Mater. Sci., vol. 38, pp. 1809–1817.

Hutchinson, J.W.; and Evans, A.G. (2002): On the Delamination of Thermal Barrier Coatings in a Thermal Gradient. Surf. Coat. Technol., vol. 149, pp. 179–184.

Hutchinson, J.W.; and Suo, Z. (1991): Mixed Mode Cracking in Layered Materials. Adv. Appl. Mech., vol. 29, 1991, pp. 63–191.

Hutchinson, John, W. (1996): Stresses and Failure Modes in Thin Films and Multilayers. Technical University of Denmark, Notes for a DCAMM Course.

Iben, Hayley, N.; and O'Brien, James F. (2009): Generating Surface Crack Patterns. Graph. Models, vol. 71, pp. 198–208.

Jabakhanji, R.; and Mohtar, R.H. (2012): A Non-Local Model for Transient Moisture Flow in Unsaturated Soils Based on the Peridynamic Theory. American Geophysical Union Fall Meeting, Abstract H43D–1387.

Jabakhanji, Rami (2013): Peridynamic Modeling of Coupled Mechanical Deformations and Transient Flow in Unsaturated Soils. Ph.D. Dissertation, Purdue University.

Khatun, Tajkera; Dutta, Tapati; and Tarafdar, Sujata (2015): Topology of Desiccation Crack Patterns in Clay and Invariance of Crack Interface Area With Thickness. Eur. Phys. J. E, vol. 38, p. 83.

Kindle, E.M. (1917): Some Factors Affecting the Development of Mud-Cracks. J. Geol., vol. 25, no. 2, pp. 135–144.

Krämer, S., et al. (2008): Mechanisms of Cracking and Delamination Within Thick Thermal Barrier Systems in Aero-Engines Subject to Calcium-Magnesium-Alumino-Silicate (CMAS) Penetration. Mater. Sci. Eng. A, vol. 490, pp. 26–35.

Lee, K.N. (2000a): Current Status of Environmental Barrier Coatings for Si-Based Ceramics. Surf. Coat. Technol., vols. 133–134, pp. 1–7.

Lee, K.N. (2018): $Yb_2Si_2O_7$ Environmental Barrier Coatings With Reduced Bond Coat Oxidation Rates via Chemical Modifications for Long Life. J. Am. Ceram. Soc., vol. 102, no. 3, pp. 1507–1521.

Lee, Kang N. (2000b): Key Durability Issues With Mullite-Based Environmental Barrier Coatings for Si-Based Ceramics. J. Eng. Gas Turbines Power (ASME 99–GT–443), vol. 122, no. 4, pp. 632–636.

Lee, Kang N. (2015): Environmental Barrier Coatings for SiC_f/SiC. Ceramic Matrix Composites: Materials, Modeling and Technology, Narottam P. Bansal and Jacques Lamon, eds., John Wiley & Sons, Hoboken, NJ.

Lee, Kang, N.; and Miller, Robert, A. (1996): Development and Environmental Durability of Mullite and Mullite/YSZ Dual Layer Coatings for SiC and Si_3N_4 Ceramics. Surf. Coat. Technol., vol. 86–87, pp. 142–148.

Leguillon, D., et al. (2014): Cracks Pattern Formation and Spalling in Functionalized Thin Films. Procedia Materials Science, vol. 3, pp. 104–109.

Leguillon, D., et al. (2016): Prediction of the Surface Cracking Pattern of an Oxidized Polymer Induced By Residual and Bending Stresses. Int. J. Solids Struct., vol. 91, pp. 89–101.

Leguillon, Dominique; Li, Jia; and Martin, Eric (2017): Multi-Cracking in Brittle Thin Layers and Coatings Using a FFM Model. Eur. J. Mech. A-Solid., vol. 63, pp. 14–21.

Leigh, Sang-Ha; Lin, Chung-Kwei; and Berndt, Christopher C. (1997): Elastic Response of Thermal Spray Deposits Under Indentation Tests. J. Am. Ceram. Soc., vol. 80, no. 8, pp. 2093–2099.

Levi, Carlos G., et al. (2012): Environmental Degradation of Thermal-Barrier Coatings by Molten Deposits. MRS Bull., vol. 37, pp. 932 and 941.

Li, C.-J.; and Ohmori, A. (2002): Relationships Between the Microstructure and Properties of Thermally Sprayed Deposits. J. Therm. Spray Techn., vol. 11, no. 3, pp. 365–374.

Liang, J., et al. (2003): Evolving Crack Patterns in Thin Films With the Extended Finite Element Method. Int. J. Solids Struct., vol. 40, no. 10, pp. 2343–2354.

Mal, Dibyendu, et al. (2006): Formation of Crack Patterns in Clay Films: Desiccation and Relaxation. J. Phys. Soc. Jpn., vol. 76, no. 1.

Matsubara, Hitoshi, et al. (2015): Numerical Modelling of Mudcrack Growth. Japanese Geotechnical Society Special Publication, vol. 2, no. 31, pp. 1143–1147.

Meier, Susan Manning; Nissley, David M.; and Sheffler, Keith D. (1991): Thermal Barrier Coating Life Prediction Model Development. J. Eng. Gas Turbines Power (ASME 91–GT–40), vol. 114, no. 2, pp. 258–263.

Mercer, C., et al. (2005): A Delamination Mechanism for Thermal Barrier Coatings Subject to Calcium–Magnesium–Alumino-Silicate (CMAS) Infiltration. Acta Mater., vol. 53, pp. 1029–1039.

Morris, Peter H.; Graham, J.; and Williams, David J. (1992): Cracking in Drying Soils. Can. Geotech. J., vol. 29, no. 2, pp. 263–277.

Mumm, D.R.; and Evans, A.G. (2001): Mechanisms Controlling the Performance and Durability of Thermal Barrier Coatings. Key Eng. Mater., vol. 197, pp. 199–230.

Nahlawi, H.; and Kodikara, J.K. (2006): Laboratory Experiments on Desiccation Cracking of Thin Soil Layers. Geotech. Geol. Eng., vol. 24, no. 6, pp. 1641–1664.

Nemeth, Noel N., et al. (2003): CARES/LIFE Ceramics Analysis and Reliability Evaluation of Structures Life Prediction Program. NASA/TM—2003-106316, 2003. http://ntrs.nasa.gov

Nemeth, Noel, N. (2013a): Unit-Sphere Multiaxial Stochastic-Strength Model Applied to Anisotropic and Composite Materials. NASA/TP—2013-217749. http://ntrs.nasa.gov/

Nemeth, Noel, N. (2013b): Unit-Sphere Anisotropic Multiaxial Stochastic-Strength Model Probability Density Distribution for the Orientation of Critical Flaws. NASA/TM—2013-217810. http://ntrs.nasa.gov/

Nemeth, Noel, N. (2014a): Probability Density Distribution of the Orientation of Strength-Controlling Flaws From Multiaxial Loading Using the Unit-Sphere Stochastic Strength Model for Anisotropy. Int. J. Fract., vol. 185, nos. 1–2, pp. 97–114.

Nemeth, Noel N. (2014b): Unit-Sphere Multiaxial Stochastic-Strength Model Applied to a Composite Material. J. Compos. Mater., vol. 48, no. 27, pp. 3395–3424.

Nemeth, Noel N., et al. (2016a): Stochastic-Strength-Based Damage Simulation Tool for Ceramic Matrix and Polymer Matrix Composite Structures. NASA/TM—2016-219113. http://ntrs.nasa.gov/

Nemeth, Noel N., et al. (2016b): Stochastic-Strength-Based Damage Simulation of Ceramic Matrix Composite Laminates. NASA/TM—2016-219115. http://ntrs.nasa.gov/

Nemeth, Noel, et al. (2017): Stochastic-Strength-Based Damage Simulation of Environmental Barrier Coating Micro/Meso Cross-Section From Thermal Cool Down. Presented at the United States Advanced Ceramics Association (USACA) 41st Annual Conference on Composites, Materials, and Structures, Cocoa Beach, FL.

Nemeth, Noel, et al. (2018): Simulation of Stochastic Mud-Crack Damage Formation in an Environmental Barrier Coating. Presented at the United States Advanced Ceramics Association (USACA) 42nd Annual Conference on Composites, Materials, and Structures, Cocoa Beach, FL.

Nemeth, Noel N.; Jadaan, Osama M.; and Gyekenyesi, John P. (2005): Lifetime Reliability Prediction of Ceramic Structures Under Transient Thermomechanical Loads. NASA/TP—2005-212505. http://ntrs.nasa.gov/

O'Brien, James, F. (2000): Graphical Modeling and Animation of Fracture. Ph.D. Thesis, Georgia Institute of Technology.

O'Brien, James F. (2017): University of California at Berkley, private communication.

O'Brien, James F.; and Hodgins, Jessica K. (1999): Graphical Modeling and Animation of Brittle Fracture. Computer Graphics Proceedings, Annual Conference Series.

Opila, Elizabeth J. (1999): Variation of the Oxidation Rate of Silicon Carbide With Water-Vapor Pressure. J. Am. Ceram. Soc., vol. 82, no. 3, pp. 625–636.

Opila, Elizabeth J. (2003): Oxidation and Volatilization of Silica Formers in Water Vapor. J. Am. Ceram. Soc., vol. 86, no. 8, pp. 1238–1248.

Opila, Elizabeth J., et al. (1999): SiC Recession Caused by SiO_2 Scale Volatility Under Combustion Conditions: II, Thermodynamics and Gaseous-Diffusion Model. J. Am. Ceram. Soc., vol. 82, no. 7, pp. 1826–1834.

Opila, Elizabeth J.; Fox, Dennis S.; and Jacobson Nathan S. (1997): Mass Spectrometric Identification of Si-O-H(g) Species From the Reaction of Silica With Water Vapor at Atmospheric Pressure. J. Am. Ceram. Soc., vol. 80, no. 4, pp. 1009–1012.

Opila, Elizabeth J.; and Hann, Raiford E., Jr. (1997): Paralinear Oxidation of CVD SiC in Water Vapor. J. Am. Ceram. Soc., vol. 80, no. 1, pp. 197–205.

Paluszny, Adriana; and Matthäi, Stephan K. (2009): Numerical Modeling of Discrete Multi-Crack Growth Applied to Pattern Formation in Geological Brittle Media. Int. J. Solids Struct., vol. 46, nos. 18–19, pp. 3383–3397.

Pfaff, Tobias, et al. (2014): Adaptive Tearing and Cracking of Thin Sheets. ACM Trans. Graph., vol. 33, no. 4, article no. 110.

Richards, B.T., et al. (2015): Mechanical Properties of Air Plasma Sprayed Environmental Barrier Coating (EBC) Systems: Preliminary Assessments. Developments in Strategic Ceramic Materials: A Collection of Papers Presented at the 39th International Conference on Advanced Ceramics and Composites, Daytona Beach, FL.

Richards, Bradley, T. (2015): Ytterbium Silicate Environmental Barrier Coatings. Ph.D. Dissertation, University of Virginia School of Engineering and Applied Science.

Richards, Bradley T.; Begley, Matthew R.; and Wadley, Haydn N.G. (2015): Mechanisms of Ytterbium Monosilicate/Mullite/Silicon Coating Failure During Thermal Cycling in Water Vapor. J. Am. Ceram. Soc., vol. 98, no. 12, pp. 4066–4075.

Richards, Bradley T., et al. (2016): Fracture Mechanisms of Ytterbium Monosilicate Environmental Barrier Coatings During Cyclic Thermal Exposure. Acta Mater., vol. 103, pp. 448–460.

Ricks, Trenton; Arnold, Steven; and Harder, Bryan (2018): Coupled Thermo-Mechanical Micromechanics Modeling of the Influence of Thermally Grown Oxide Layer in an Environmental Barrier Coating System. Proceedings of the American Society for Composites 33rd Technical Conference. Seattle, WA, pp. 1528–1541.

Roth, Kurt; Boike, Julia; and Vogel, Hans-Jorg (2005): Quantifying Permafrost Patterns Using Minkowski Densities. Permafrost Periglac., vol. 16, pp. 277–290.

Sadhukhan, Supti, et al. (2007): Desiccation Cracks on Different Substrates: Simulation by a Spring Network Model. J. Phys.: Condens. Matter, vol. 19, no. 356206.

Sadhukhan, Supti, et al. (2008): Desiccation of a Clay Film: Cracking Versus Peeling. Eur. Phys. J. E Soft Matter, vol. 27, no. 4, pp. 391–395.

Sanchez, Marcelo; Manzoli, Osvaldo, L.; and Guimaraes, Leonardo, J.N. (2014): Modeling 3–D Desiccation Soil Crack Networks Using a Mesh Fragmentation Technique. Comput. Geotech., vol. 62, pp. 27–39.

Seghir, R.; and Arscott, S. (2015): Controlled Mud-Crack Patterning and Self-Organized Cracking of Polydimethylsiloxane Elastomer Surfaces. Sci. Rep., vol. 5, no. 14787.

Shenoy, V.B.; Schwartzman, A.F.; and Freund, L.B. (2001): Crack Patterns in Brittle Thin Films. Int. J. Fract., vol. 109, no. 1, pp. 29–45.

Shetty, D.K. (1987): Mixed-Mode Fracture Criteria for Reliability-Analysis and Design With Structural Ceramics. J. Eng. Gas Turbines Power, vol. 109, no. 3, pp. 282−289.

Silling, S.A. (2000): Reformulation of Elasticity Theory for Discontinuities and Long-Range Forces. J. Mech. Phys. Solids, vol. 48, pp. 175–209.

Skjeltorp, A.T.; and Meakin, Paul (1988): Fracture in Microsphere Monolayers Studied by Experiment and Computer Simulation. Nature, vol. 335, pp. 424–426.

Strangman, Tom, et al. (2007): Damage Mechanisms, Life Prediction, and Development of EB–PVD Thermal Barrier Coatings for Turbine Airfoils. Surf. Coat. Technol., vol. 202, nos. 4–7, pp. 658–664.

Sukumar, N.; and Prévost, J-H. (2003): Modeling Quasi-Static Crack Growth With the Extended Finite Element Method: Part I: Computer Implementation. Int. J. Solids Struct., vol. 40, pp. 7513–7537.

Timm, D.H.; Guzina, B.B.; and Voller, V.R. (2003): Prediction of Thermal Crack Spacing. Int. J. Solids Struct., vol. 40, pp. 125–142.

Thouless, M.D. (1990): Crack Spacing in Brittle Films on Elastic Substrates. J. Am. Ceram. Soc., vol. 73, no. 7, pp. 2144–2146.

Valette, Gilles, et al. (2008): A Dynamic Model of Cracks Development Based in a 3D Discrete Shrinkage Volume Propagation. Comput. Graphics Forum, vol. 27, no. 1, pp. 47–62.

Vogel, H.-J., et al. (2005a): Studies of Crack Dynamics in Clay Soil: II. A Physically Based Model for Crack Formation. Geoderma, vol. 125, nos. 3–4, pp. 213–223.

Vogel, H.-J.; Hoffmann, H.; and Roth, K. (2005b): Studies of Crack Dynamics in Clay Soil: I. Experimental Methods, Results, and Morphological Quantification. Geoderma, vol. 125, nos. 3–4, pp. 203–211.

Wadley, H.N.G. (2017): University of Virginia, personal communication.

Weibull W. (1939): A Statistical Theory of the Strength of Materials. Ingeniorsvetenskapsakadamiens Handlinger, no. 151.

Wikipedia contributors: Mudcracks. Wikipedia, The Free Encyclopedia, 2019. https://en.wikipedia.org/wiki/Mudcrack

Xia, Z. Cedric; and Hutchinson, John W. (2000): Crack Patterns in Thin Films. J. Mech. Phys. Solids, vol. 48, pp. 1107–1131.

Yanaka, M., et al. (2001): Statistical Analysis of Multiple Cracking Phenomenon of a SiO_x Thin Film on a Polymer Substrate. J. Appl. Phys., vol. 90, no. 2, pp. 713–719.

Zhang, X.C., et al. (2008a): Analysis on Multiple Cracking in Film/Substrate Systems With Residual Stresses. J. Appl. Phys., vol. 103, p. 023519.

Zhang, X.C., et al. (2008b): Multiple Film Cracking in Film/Substrate Systems With Mismatch Strain and Applied Strain. J. Appl. Phys., vol. 104, no. 6, p. 063520.